UNIVERSITY OF SOUTHAMPTON

FACULTY OF ENGINEERING, SCIENCE & MATHEMATICS

Optoelectronics Research Centre

Trapped-modes, Slow Light and Collective Resonances in Metamaterials

by

Nikitas Papasimakis

Thesis for the degree of Doctor of Philosophy

July 2009

UNIVERSITY OF SOUTHAMPTON

ABSTRACT

FACULTY OF ENGINEERING, SCIENCE & MATHEMATICS
OPTOELECTRONICS RESEARCH CENTRE

Doctor of Philosophy

Trapped-modes, Slow Light and Collective Resonances in Metamaterials

by Nikitas Papasimakis

A new class of metamaterials exhibiting coherent, collective response has been introduced. It is shown that the sharp resonant behaviour of coherent metamaterials can only be observed in arrays of metamaterial elements and is absent from the respose of a single isolated unit cell. As a result, such arrays are extremely sensitive to positional disorder and resonances degrage rapidly with increasing randomization. These obsered strong inter-element interactions render coherent etamaterials ideal candidates for gain-assisted functionalities as deonstrated by the suggestion and numerical study of a novel amplifying/lasing device, termed tha lasing spaser. An antipode class of incoherent metamaterials is also presented, where the resonant respose of a single unit and of an infinite array are very similar resulting in weak dependnce on disorder.

The first metamaterial analogue of electromagnetically induced transparency is demonstrated experimentally and theoretically in essentially planar structures. The phenomenon arises from destructive interference of fields radiated by strongly coupled metamaterial elements that support anti-symmetric weakly-radiating current configurations, termed trapped-modes. This behaviour is accompanied by sharp resonances and steep normal dispersion which leads to long pulse delays, It is shown that cascading of metamaterial slabs increases the bandwidth of the pulse delay effect, while extension to all-angles and all-polarizations is demonstrated by appealing to incoherent metamaterials.

The first experimental study of metamaterials with toroidal symmetry is reported. Resonant circular dichroism is observed in a a metamaterial consisting of toroidal wire windings. Further numerical investigation attributes the gyrotropic behaviour to current standing waves correspoding to the eigenmodes of the unit cell winding. Multipole expansion of the resonant current configurations indicates a dominant electric dipole-magnetic dipole contribution to gyrotropy followed by electric dipole-electric quadrupole order effects, while a non-negligible toroidal response comparable to electric quadrupole in scattering efficiency also emerges.

Finally, collective effects are studied in quasicrystal hole arrays and it is demonstrated that non-resonant scatterers can lead to strong lattice resonances and extraordinary trasmission even in the case of quasi-periodicity. Microwave and optical quasicrystal patterns exhibit similar response exceeding predictions based on absence of inter-element interactions and even reaching a nearly invisible state in the microwave part of the spectrum.

CONTENTS

LIST OF FIGURES

Declaration of Authorship

I, Nikitas Papasimakis, declare that the thesis entitled *Trapped-modes, Slow Light and Collective Resonances in Metamaterials* and the work presented in the thesis are both my own, and have been generated by me as the result of my own original research. I confirm that:

- this work was done wholly or mainly while in candidature for a research degree at this University;
- where any part of this thesis has previously been submitted for a degree or any other qualification at this University or any other institution, this has been clearly stated;
- where I have consulted the published work of others, this is always clearly attributed;
- where I have quoted from the work of others, the source is always given. With the exception of such quotations, this thesis is entirely my own work;
- I have acknowledged all main sources of help;
- where the thesis is based on work done by myself jointly with others, I have made clear exactly what was done by others and what I have contributed myself;
- parts of this work have been published (see the list of publications in Appendix)

Signed: .....

Date: .....

ACKNOWLEDGEMENTS

I am grateful to Prof. N. I. Zheludev for inspiration and supervision, and to Dr. V. A. Fedotov for guidance and assistance throughout the course of my research studies. I would like to thank Prof. J. Garcia de Abajo, Prof. S. L. Prosvirnin, Prof. D. P. Tsai, and Dr. Y. Chen for their collaboration and input, Dr. A. V. Krasavin and A. S. Schwanecke for providing support in early numerical and experimental efforts, respectively, as well as Dr. A. Denisyuk, Dr. Y. Fu, and Mr. X. Xiang for their help in experimental work. Finally, I am indebted to my family for their continuing support.

1. INTRODUCTION

1.1 Motivation

Electromagnetic phenomena underpin the majority of contemporary technologies, ranging from telecommunications to data processing. These technologies depend heavily on and are fuelled by advances in electromagnetics. Mobile phone antennas, fiber networks, phased antenna arrays, radomes, sensors are all mainly based on structured electromagnetic materials. Metamaterials are a special class of artificial electromagnetic structures aiming to control wave propagation. Their unusual and useful functionalities originate from structuring on a sub-wavelength scale and are not attainable by materials available in nature. They hold promise of exotic applications, such as invisibility cloaks, perfect lenses, novel light emitting devices and ultra thin delay lines, and are expected to play a key role in the next photonic revolution leading to ground breaking new science and applications on a global scale.

1.2 Structured Electromagnetic Materials

Controlling optical properties by structuring is common practise in nature as demonstrated by an ever-growing body of evidence [1]. One of the most notable examples is the anti-reflective properties of the micro-structure in the eye of certain insects resulting in enhanced sensitivity [2]. Intriguing cases also include the iridescence exhibited by the spine of the sea mouse resulting from hexagonal crystal-like structuring [3] and the color-selective reflection and transmission of butterfly wing owing to its multi-layer nature [4] to name just a few (see Fig 1.1).

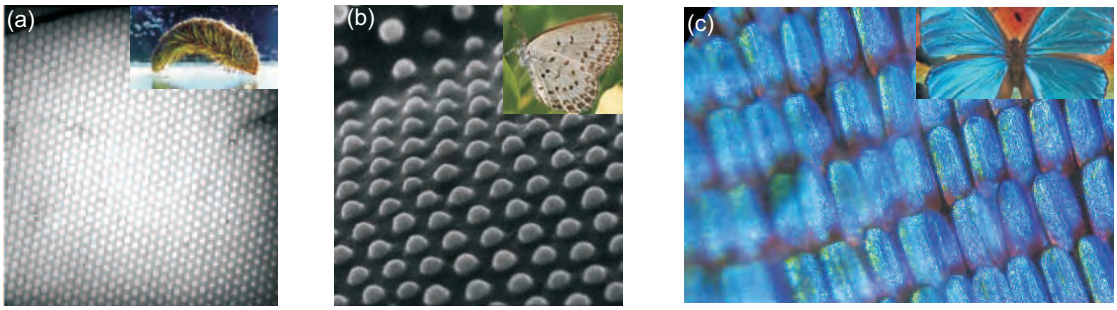

Fig. 1.1: (a) Hexagonal structure of the sea mouse spine, responsible for the observed iridescence [3]. (b) Microscopic protrusions on the butterfly eye function exhibit broad-band anti-reflection properties [2]. (c) Butterfly wings present selective reflection both in terms of angle and color as a result of micro-structuring [4] (photos from [5]).

Unaware of nature's intricate strategies, early civilizations demonstrated substantial interest in controlling light propagation by natural and artificial structures. Magnifying lenses have been used since ancient times in ancient Assyria [6] and Egypt [7] presumably to facilitate the carving

and reading of engravings, while Roman craftsmen doped glass with gold droplets resulting in a dichroic material seen with different colors in transmission and reflection [8] (see Fig 1.2).

Fig. 1.2: The Nimrud lens (1000 BC) (a) and the Lycurgus cup (4^{th} century AD) as seen in reflected (b) and transmitted (c) light [13].

However, the first systematic studies of artificially structured electromagnetic materials had to wait until the development of spectroscopy and the unification of electromagnetic phenomena in the 19^{th} century [9]. Fraunhofer presented the first gratings for spectroscopic measurements and described theoretically their dispersive behaviour [10]. Soon after Lord Rayleigh predicted the presence of a band gap for 1D periodically stacked structures with alternating layers [11]. At the same time, J. C. Bose performed in India a series of still not-widely known experiments on electromagnetic composite media including stacks of metal plates and twisted jute ensembles, demonstrating polarization rotation and other electromagnetic phenomena [12].

Fig. 1.3: (A stack of aluminium plates placed between the pages of a railway catalog (a) and a twisted jute ensemble (b)-(c) employed by J. C. Bose in polarization experiments with mm-wave radiation [12].

Further significant advancements were triggered by the development of wireless communications and radar systems especially during and after World War II, where devices such as antenna radomes, filters, transmitters and receivers were of crucial importance. It was not long until it was realized that arrays comprised of subwavelength electromagnetic resonators can dramatically reduce the scattering cross-section of antennas at most frequencies, thus leading to the concept of frequency selective surfaces (FSS) [14]. In particular, FSS are usually double periodic resonator arrays that exhibit filter behaviour, rejecting or transmitting the incident radiation within a narrow frequency band, while appearing transparent or opaque, respectively, outside this band.

Although, they were initially invented in order to reduce the radar cross-section of mobile antenna systems [15], they have found wide applications enabling and enhancing the performance of important devices, such as reflector arrays [16] and high impedance surfaces [17].

In parallel, inspired by the world-changing applications of semiconductor electronics, E. Yablonovith and S. John proposed that photons in dielectric periodic stuctures can behave analogously to electrons in semiconductors and suggested the use of such photonic crystal in order to inhibit spontaneous emission [18] and localize photons [19], respectively. Although initial investigations were restricted to the microwave domain by fabrication limitations [20], borrowing manufacturing techniques from the semiconductor industry soon lead to photonic crystals operating in optical wavelengths [21]. Photonic crystals hold promise of important applications including optical buffers [22] and light-emitting devices [23], while their ability to control light confinement has already lead to commercial uses in optical fibers [24].

Fig. 1.4: (a) Mid-infrared multi-band FSS [25]. (b) Three-dimensional photonic crystal [26]. (c) Photonic crystal waveguide that exhibits slow light behaviour [27].

Today, interest in artificial structures has been renewed largely due to two reasons: first the rapid advances in fabrication techniques which allow structuring of electromagnetic materials at the nano-scale, and secondly due to the birth of metamaterials, a new research field in the borders between optics and electrical engineering.

1.3 Metamaterials

Metamaterials comprise a rapidly advancing research field, with new directions constantly emerging. As a result, it is not an easy task to coin a universally accepted definition without risking to exclude important areas of research [28]. Therefore, here we adopt the rather loose definition of [29], according to which metamaterials are artificial media consisting of electromagnetic resonators in crystal-like arrangements with a pitch smaller than the wavelength of excitation. Owing to their sub-wavelength structuring, metamaterials appear as effective media to an incident wave with constitutive parameters defined to a large extent by their geometry. Hence, by appropriate patterning, the constitutive parameters of metamaterials can be tailored across a wide range surpassing the properties of naturally available materials.

Probably the first metamaterial is the jute composite used by Bose in his polarization rotation experiments [12]. Almost fifty years after Bose, it was suggested that a lens consisting of stacked metallic plates acts as an artificial dielectric with refractive index less than one, while soon after it was realized that metallic and dielectric rod can simulate plasma behaviour at microwave frequencies [31, 32] (see Fig. 1.5). Almost another forty years had to pass before the next step in metamaterials research, when Sir John Pendry suggested that an ensembe of split-ring resonators

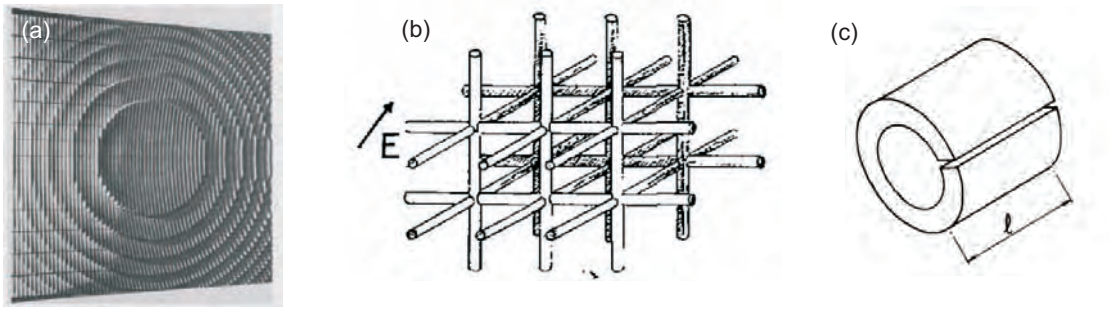

Fig. 1.5: (a) Lens comprised by metallic plates resulting in refractive index less than unity [30]. (b) Array of dielectric rods exhibiting plasma behaviour [32]. (c) Primitive form of the split-ring resonator [33].

(SRRs) -introduced earlier to create a magnetic resonance at GHz frequencies [33], can constitute an effective magnetic medium described by a macroscopic permeability [34]. Armed by artificial media with controllable electric and magnetic response, structures that present simultaneously negative electric permittivity and magnetic permeability were realized [35] (see Fig. 1.6a), a concept considered earlier but remained a theoretical peculiarity due to lack of appropriate materials [36, 37, 38, 39]. The potential of such media was realized by Pendry who suggested that they can be used to build a perfect lens, i.e. a lens that harvests both propagating and evanescent fields and hence is not limited by the wavelength of light [40]. Pendry's theoretical predictions were soon followed by an experimental demonstration of the concept at microwave frequencies [41].

Microwave metamaterials were successfully scaled down to operate at mid- and near-infrared wavelengths with moderate efforts and no significant change in their electromagnetic properties [42, 43]. However, transferring the metamaterial concept in the optics domain was hindered by unforeseen obstacles. On one hand the technical difficulties of structuring materials at the nanoscale restrict visible metamaterials in thin layers, in contrast to their three-dimensional infrared and microwave counterparts. On the other hand, the high losses associated with metals at optical frequencies and the saturation of the magnetic response of SRRs degrade significantly metamaterial performance [44]. The solution was given by a radical change in the geometry of metamaterial resonators, replacing SRRs with metallic elements of appropriate shape. Following this approach optical negative refractive index metamaterials were demonstrated based on pairs of metallic rods [45] and on its complimentary structure, namely pairs of voids on metal films [46], as well as on variations of the latter [47] including the so-called fishnet structure [48].

Although the main body of metamaterial research has focused so far in achieving a negative refractive index, a number of different directions have emerged. Most notably, metamaterials have enabled experimental investigations of the newly founded field of transformation optics [49, 50], where electromagnetic waves are guided and redirected at will, promising applications as exotic as invisibility cloaks. Such effects are made possible by carefully tailoring the permittivity and permeability of the medium surrounding the object to be cloaked, in order to guide incident radiation around the latter rendering it virtually invisible. Experimental demonstrations of cloaking by metamaterial devices have been performed successfully so far in microwave by metal-dielectric metamaterial composites [51] as well as in the visible part of the spectrum by all-

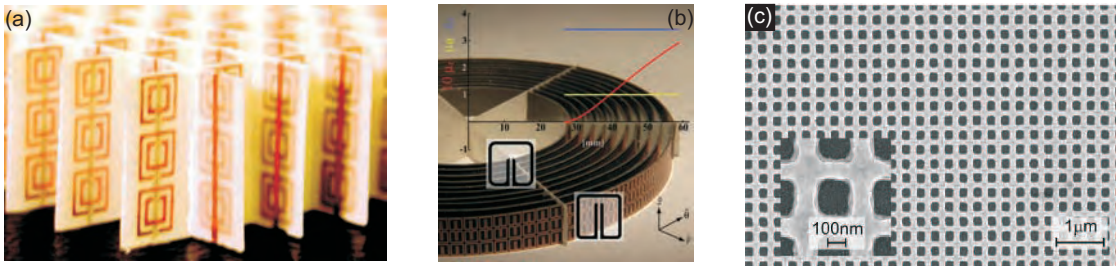

Fig. 1.6: (a) First realization of a negative refractive index medium [35]. (b) Microwave metamaterial with invisibility cloak functionality [51]. (c) An optical negatively refractive metamaterial based on the fish-net structure [48].

dielectric metamaterials [52].

Symmetry considerations have incited investigations of polarization sensitive behaviour of chiral metamaterials, providing an alternative path to negative refraction [53, 54] and leading to the demonstration of intriguing properties, such as giant gyrotropy [55], asymmetric transmission [56] and optical activity without chirality [57]. Further away from the mainstream of metamaterials research, the behavior of metamaterials exhibiting toroidal symmetries has been investigated theoretically and negative refraction along side with other interesting electromagnetic properties was predicted [58].

Recently, it was demonstrated that the metamaterial response can be controlled through symmetry breaking in split-rings (see Fig. 1.7a) by employing coupled resonances, thus introducing the concept of trapped-mode metamaterials, i.e. artificial structures exhibiting narrow-band resonant response resulting from strong interference of its constituents [59]. This lead to a first demonstration of a metamaterial analogue of electromagnetically induced transparency (EIT), where a bi-layered metamaterial was rendered transparent by a resonant anti-phase excitation of the two layers [60] (see Fig. 1.7b). Similar behavior was soon observed for plasmonic metamaterials [61] and experimentally demonstrated in the optical [62] based on the coupling of radiative and dark, sub-radiant elements (see Figs. 1.7c & 1.7d). Finally, EIT-like behaviour was also observed in the THz regime [63] on a scaled-down version of the metamaterial employed in [59], while an omni-directional metamaterial analog of EIT was demonstrated in [64].

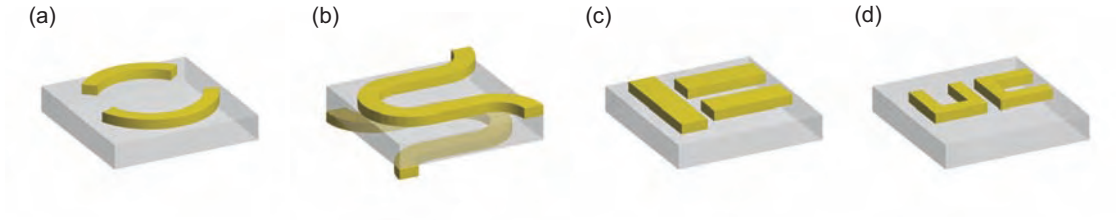

Fig. 1.7: Unit cells of metamaterials exhibiting EIT-like behaviour: (a) asymmetrically split-rings [59], (b) bi-layered fish-scale [59], (c) coupled metallic stripes [61], and (d) coupled split-ring resonators [62].

Metamaterial analogs of EIT are expected to play a key role in future developments in metamaterial research. In a first instance, low-loss metamaterials based on this concept have been predicted [65]. Trapped-mode metamaterials, in particular, can be tailored to exhibit coherent or incoherent behaviour, namely collective or individual response, enabling novel applications and

alleviating fabrication restrictions. Coherent metamaterials are especially important in view of the recent advances in the active metamaterials. Predictions for gain-assisted metamaterials include compensation of metallic losses at visible frequencies leading to loss-less negative refraction [66, 67, 68, 69, 70, 71], amplification and lasing [73, 74]. In the case of coherent metamaterials, low-threshold and truly planar light emitting devices have been suggested and investigated [74, 75], achieving enhanced functionality not accessible by conventional metamaterials. Finally, as demonstrated in this thesis, incoherent trapped-mode metamaterials show very weak dependence on positional disorder, thus allowing for fabrication imperfections and rendering accessible methods, such as self-assembly [76].

1.4 Thesis Overview

This thesis is concerned with the study of coupled resonances, interference effects and collective behaviour in metamaterials.

Chapter 2 provides a brief theoretical background for the undertaken investigations presented in this thesis, while a brief description of the experimental and numerical methods employed can be found in Chapter 3.

A novel type of metamaterial resonances, the so-called "trapped-mode" resonances is studied in chapter 4. The relation between the symmetry of the metamaterial resonators and the electromagnetic response is investigated experimentally and numerically in the microwave domain, and different ways to control and tune the metamaterial response are presented.

Chapter 5 is concerned with the dispersive effects accompanying the trapped-mode resonances. It is shown that such metamaterials constitute a classical analog of the quantum phenomenon of electromagnetically induced transparency. As a result they allow for long pulse delays and ultimately the realization of ultra-compact delay lines.

In chapter 6, the collective and individual behaviour of metamaterials is studied and the concept of coherent and incoherent metamaterials is introduced. In the first case, the resonant response is a collective property that is not found in isolated unit cells. On the contrary, incoherent metamaterials the array response is not significantly different from that of a single resonator. The dependence of the metamaterial resonant response on positional and orientational disorder is studied experimentally and qualitatively interpreted in terms of the unit cell electric and magnetic response. Finally, the behaviour of coherent metamaterials in the presence of gain is investigated and a new light-emitting device, the lasing spaser, is suggested.

In chapter 7, microwave and optical planar metamaterials exhibiting extraordinary transmission are studied. Quasiperiodic lattices of subwavelength apertures that lack individual resonant response in the spectral region of interest, the arrays exhibit collective resonances related to the reciprocal lattice of the pattern.

Chapter 8 presents an investigation of the polarization sensitive response of a new type of metamaterials consisting of wire windings with toroidal symmetry. The origin of the experimentally observed gyrotropy is traced to the current configuration on the wire winding and its multipole representation, obtained through numerical simulations.

Finally, chapter 9 summarises the work presented in this thesis and discusses future directions.

BIBLIOGRAPHY

[1] A. R. Parker and H. E. Townley, Biomimetics of photonic nanostructures. *Nature Nanotechnology* **2**, 347 (2007).

[2] D. G. Stavenga, S. Foletti, G. Palasantzas, and K. Arikawa. Light on the moth-eye corneal nipple array of butterflies, *Proceedings of the Royal Society B* **273**, 661 (2006).

[3] A. R. Parker, R. C. McPhedran, D. R. McKenzie, L. C. Botten, and N. A. Nicorovici, Photonic Engineering: Aphrodite's iridescence. *Nature* **409**, 207 (2001).

[4] P. Vukusic, J. R. Sambles, C. R. Lawrencem and R. J. Wootton, Quantified interference and diffraction in single Morpho butterfly scales. *Proceedings of the Royal Society B* **266**, 1403 (1999).

[5] The Biomimicry Design Portal, *www.asknature.org*.

[6] D. Brewster, On an account of a rock-crystal lens and decomposed glass found in Niniveh. *Die Fortschritte der Physik*, 355 (1852).

[7] T. C. Kriss and V. M. Kriss, History of the operating microscope: From magnifying glass to miconeurosurgery. *Neurosurgery* **42**, 899 (1998).

[8] U. Leonhardt,Invisibility cup. *Nature Photonics* **1**, 207 (2007).

[9] J. C. Maxwell, A Dynamical Theory of the Electromagnetic Field. *Philosophical Transactions of the Royal Society of London* **155**, 459 (1865).

[10] J. Fruanhofer, Kurtzer Bericht von den Resultaten neuerer Versuche ber die Sesetze des lichtes, und die Theorie erselbem. *Annalen Der Physik* **74**, 337 (1823).

[11] J. W. Strutt, On the Maintenance of Vibrations by Forces of Double Frequency, and on the Propagation of Waves Through a Medium Endowed with a Periodic Structure. *Philosophical Magazine* **24**, 145 (1887).

[12] D. T. Emerson, The works of Jagadis Chandra Bose: 100 years of mm-wave research. *IEEE Transactions on Microwave Theory and Techniques*, **45**, 2267 (1997).

[13] The British Museum website, *www.britishmuseum.org*.

[14] B. A. Munk, *Frequency Selective Surfaces* (Wiley, New York, 2000).

[15] E. L. Pelton and B. A. Munk, A streamlined metallic radome. *IEEE Transactions* **AP-22**, 799 (1974).

[16] F. O'Nians and J. Matson, Antenna feed system utilizing polarization independent frequency selective intermediate reflector. U.S. Patent 3-231-892 (1996).

[17] D. Sievenpiper, L. Zhang, R. F. J. Broas, N. G. Alexopolous, and E. Yablonovitch, High impedance electromagnetic surfaces with a forbidden frequency band. *IEEE Transactions on Microwave Theory and Techniques*, **47**, 2059 (1999).

[18] E. Yablonovitch, Inhibited spontaneous emission in solid-state physics and electronics. *Physical Review Letters* **58**, 2059 (1987).

[19] S. John, Strong localization of photoncs in certain disordered dielectric superlattices. *Physical Review Letters* **58**, 2486 (1987).

[20] E. Yablonovitch, T. J. Gmitter, and K. M. Leung, Photonic band structure: the face-centered-cubic case employing nonspherical atoms. *Physical Review Letters* **67**, 2295 (1991).

[21] T. F. Krauss, R. M. DeLaRue, S. Brand, Two-dimensional photonic-bandgap structures operating at near-infrared wavelengths. *Nature* **383**, 699 (1996).

[22] T. Baba. Slow light in photonic crystals. *Nature Photonics* **2**, 465 (2008).

[23] M. Meier, A. Mekis, A. Dodabalapur, A. Timko, and R. E. Slusher, Laser action from two-dimensional distributed feedback in photonic crystals. *Applied Physics Letters* **74**, 7 (1999).

[24] P. S. J. Russel, Photonic crystal fibers. *Science* **299**, 358 (2003).

[25] J. A. Bossard, D. H. Werner, T. S. Mayer, J. A. Smith, Y. U. Tang, R. P. Drupp, and L. Li, The design and fabrication of planar multiband metallodielectric frequency selective surfaces for infrared applications. *IEEE Transactions on Antennas and Propagation* **54**, 1265 (2006).

[26] University of California Los Angeles, Optoelectronics Group Homepage, *http://www.ee.ucla.edu/∼photon/*.

[27] Y. A. Vlasov, M. O'Boyle, H. F. Hamann, and S. J. McNab. Active control of slow light on a chip with photonic crystal waveguides. *Nature* **438**, 65 (2005).

[28] A. Sihvola, Metamaterials in electromagnetics. *Metamaterials* **1**, 2 (2007).

[29] N. I. Zheludev, What diffraction limit? *Nature Materials* **7**, 420 (2008).

[30] W. E. Kock, Metal-lens antennas. *Proceeding of I.R.E. and Waves and Electrons* **34**, 828 (1946).

[31] J. Brown, The design of metallic delay dielectrics. *Proceedings IEE* **97**, 45 (1950).

[32] W. Rotman, Plasma simulation by artificial dielectric and parallel-plate media. *IRE Transactions on Antennas and Propagation* **10**, 82 (1962).

[33] W. V. Hardy and L. A. Whitehead, Split-ring resonator for use in magnetic resonance from 200-2000 MHz. *Review of Scientific Instruments* **52**, 213 (1981).

[34] J. B. Pendry, A. J. Holden, D. J. Robbins, and W. J. Stewart, Magnetism from conductors and enhanced nonlinear phenomena. *IEEE Transactions on Microwave Theory and Techniques* **47**, 2075 (1999).

[35] D. R. Smith, W. J. Padilla, D. C. Vier, S. C. Nemat-Nasser, and S. SChultz. Composite medium with simultaneously negative permeability and permittivity. *Physical Review Letters* **84**, 4184 (2000).

[36] L. I. Mandelshtam, Lectures on some problems of the theory of oscillations, in *Complete Collection of Works* **5** (Academy of Sciences, Moscow, 1944).

[37] D. V. Sivukhin, The energy of electromagnetic waves in dispersive media. *Optika i Spektroskopiya* **3**, 308 (1957).

[38] V. G. Veselago, The electrodynamics of substances with simultaneously negative values of ϵ and μ. *Soviet Physics Uspekhi* **10**, 209 (1968).

[39] S. A. Tretyakov, Research on negative refraction and backward-wave media: A historical perspective. *EPFL Latsis Symposium 2005*, Lausanne 28.2-2.3.2005.

[40] J. B. Pendry, Negative refraction makes a perfect lens. *Physical Review Letters* **85**, 3966 (2000).

[41] A. Grbic and G. V. Eleftheriades, Overcoming the diffraction limit with a planar left-handed transmission-line lens. *Physical Review Letters* **92**, 117403 (2004).

[42] T. J. Yen, W. J. Padilla, N. Fang, D. C. Vier, D. R. Smith, J. B. Pendry, D. N. Basoc, and X. Zhang, Terahertz magnetic response from artificial materials. *Science* **303**, 1494 (2004).

[43] W. J. Padilla, A. J. Taylor, C. Highstrete, M. Lee, and R. D. Averitt, Dynamical electric and magnetic response at terahertz frequencies. *Physical Review Letters* **96**, 107401 (2006).

[44] J. Zhou, Th. Koschny, M. Kafesaki, E. N. Economou, J. B. Pendry, and C. M. Soukoulis, Saturation of the magnetic response of split-ring resonators at optical frequencies. *Physical Review Letters* **95**, 223902 (2005).

[45] V. M. Shalaev, W. Gai, U. K. Chettiar, H. K. Yuan, A. K. Sarychev, V. P. Drachev, and A. V. Kildishev, Negative index of refraction in optical metamaterials, *Optics Letters* **30**, 3356 (2005).

[46] S. Zhang, W. Fan, N. C. Panoiu, K. J. Malloy, R. M. Osgood, and S. R. J. Brueck, Experimental demonstration of near-infrared negative-index metamaterials. *Physical Review Letters* **95**, 137404 (2005).

[47] U. K. Chettiar, A. V. Kildishev, H. K. Yuan, W. Cai, S. Xiao, V. P. Drachev, and V. M. Shalaev, Dual-band negative-index metamaterial: double negative at 813 nm and single negative at 772 nm. *Optics Letters* **32**, 1671 (2007).

[48] G. Dolling, M. Wegener, C. M. Soucoulis, and S. Linden, Negative-index metamaterial at 780 nm wavelength. *Optics Letters* **32**, 53(2007).

[49] J. B. Pendry, D. Schurig, and D. R. Smith, Controlling electromagnetic fields. *Science* **312**, 1780 (2006).

[50] U. Leonhardt, Optical conformal mapping. *Science* **312**, 1777 (2006).

[51] D. Schurig, J. J. Mock, B. J. Justice, S. A. Cummer, J. B. Pendry, A. F. Starr, and D. R. Smith, Metamaterial electromagnetic cloak at microwave frequencies. *Science* **314**, 977 (2006).

[52] J. Valentine, J. Li, T. Zentgraf, G. Bartal, and X. Zhang, An optical cloak made of dielectrics. *Nature Materials* advanced online publication (2009).

[53] J. B. Pendry, A chiral route to negative refraction *Science* **306**, 1353 (2004).

[54] S. Tretyakov, A. Sihvola, and L. Jylha, Backward-wave regime and negative refraction in chiral composites. *Photonics and Nanostructures* **3**, 107 (2005).

[55] A. V. Rogacheva, V. A. Fedotov, A. S. Schwanecke, and N. I. Zheludev, Giant gyrotropy due to electromagnetic-field coupling in a bilayered chiral structure. *Physical Review Letters* **97**, 177401 (2006).

[56] V. A. Fedotov, P. L. Mladyonov, S. L. Prosvirnin, A. V. Rogacheva, Y. Chen, and N. I. Zheludev, Asymmetric propagation of electromagnetic waves through a chiral structure. *Physical Review Letters* **97**, 167401 (2006).

[57] E. Plum, X. X. Liu, V. A. Fedotov, Y. Chen, D. P. Tsai and N. I. Zheludev, Metamaterials: Optical activity without chirality. *Physical Review Letters* **102**, 113902 (2009).

[58] K. Marinov, A. D. Boardman, V. A. Fedotov, and N. I. Zheludev, Toroidal metamaterial *New Journal of Physics* **9**, 324 (2007).

[59] V. A. Fedotov, M. Rose, S. L. Prosvirnin, N. Papasimakis, and N. I. Zheludev. Sharp trapped mode resonances in planar metamaterial with a broken structural symmetry. *Physical Review Letters* **99**, 147401 (2007).

[60] N. Papasimakis, V. A. Fedotov, S. L. Prosvirnin, and N. I. Zheludev, Metamaterial analog of electromagnetically induced transparency. *Physical Review Letters* **101**, 253903 (2008).

[61] S. Zhang, D. A. Genov, Y. Wang, M. Liu, and X. Zhang, Plasmon-induced transparency in metamaterials. *Physical Review Letters* **101**, 047401 (2008).

[62] N. Liu, L. Fu, S. Kaiser, H. Schweizer, and H. Giessen, Plasmonic building block for magnetic molecules in three-dimensional optical metamaterials. *Advanced Materials* **20**, 3859 (2008).

[63] R. Singh, C. Rockstuhl, F. Lederer, and W. Zhang, Coupling betweena dark and a bright eigenmode in a terahertz metamaterial. *Physical Review B* **79**, 085111 (2009).

[64] N. Papasimakis, Y. H. Fu, V. A. Fedotov, S. L. Prosvirnin, D. P. Tsai, and N. I. Zheludev, Metamaterial with polarization and direction insensitive resonant transmission response mimicking electromagnetically induced transparency. *Applied Physics Letters* **94**, 211902 2009).

[65] P. Tassin, L. Zhang, Th. Koschny, E. N. Economou, and C. M. Soukoulis, Low-loss metamaterials based on classical electromagnetically induced transparency. *Physical Review Letters* **102**, 053901 (2009).

[66] A. B. Kozyrev, H. Kim, and D. W. van der Weide,Parametric amplification in left-handed transmission line media,*Applied Physics Letters*, **88**, 264101 (2006).

[67] A. K. Popov, and V. M. Shalaev, Compensating losses in negative-index metamaterials by optical parametric amplification. *Optics Letters* **31**, 2169 (2006).

[68] A. D. Boardman, Y. G. Rapoport, N. King, and V. N. Malnev, Creating stable gain in active metamaterials. *Journal of the Optical Society of America B* **24**, A53 (2007).

[69] A. A. Govyadinov, V. A. Podolskiy, and M. A. Noginov, Active metamaterials: Sign of refractive index and gain-assisted dispersion management. *Applied Physics Letters* **91**, 191103 (2007).

[70] A. Bratkovsky, E. Ponizovskaya, S.-Y. Wang, P. Holmstrom, L. Thylen, Y. Fu, and H. Agren, A metalwire/quantum-dot composite metamaterial with negative ϵ and compensated optical loss. *Applied Physics Letters* **93**, 193106 (2008).

[71] Z.-G. Dong, H. Liu, T. Li, Z.-H. Zhu, S.-M. Wang, J.-X. Cao, S.-N. Zhu, and X. Zhang, Resonance amplification of left-handed transmission at optical frequencies by stimulated emission of radiation in active metamaterials. *Optics Express* **16**, 20974 (2008).

[72] O. Sydoruk, E. Shamonina, and L. Solymar, Parametric amplification in coupled magnetoinductive waveguides. *Journal of Physics D: Applied Physics* **40**, 6879 (2007).

[73] A. K. Sarychev, and G. Tartakovsky, Magnetic plasmonic metamaterials in actively pumped host medium and plasmonic nanolaser. *Physical Review B* **75**, 085436 (2007).

[74] N. I. Zheludev, S. L. Prosvirnin, N. Papasimakis, and V. A. Fedotov, Lasing spaser. *Nature Photonics* **2**, 351 (2008).

[75] 11. M. Wegener, J. L. Garcia-Pomar, C. M. Soukoulis, N. Meinzer, M. Ruther, and S. Linden, Toy model for plasmonic metamaterial resonances coupled to two-level system gain. *Optics Express***16**, 19785 (2008).

[76] D. A. Pawlak, Metamaterials and photonics crystals - potential applications for self-organized eutectic micro- and nanostructures. *Scientia Plena* **4**, 014801 (2008).

2. THEORETICAL BACKGROUND

In this chapter, a brief theoretical background to the reported work is provided. In particular, a first principles derivation of the macroscopic Marwell equations from their microscopic equivalents is presented and constitutive relations for the response fields are introduced. In the case of metamaterials, the contributions to the material parameters from the individual resonators and from their interactions are separated and the conditions for strong collective effects are investigated. Finally, the complete and approximate forms of the multipole expansion for electromagnetic fields radiated by localized sources are discussed.

2.1 Macroscopic and Microscopic Maxwell Equations

Within the framework of classical electrodynamics, the interactions of matter with electromagnetic fields are described by the microscopic Maxwell equations [1]:

$$\vec{\nabla} \cdot \vec{e}(\vec{r},t) = \eta(\vec{r},t)/\epsilon_0 \tag{2.1}$$

$$\vec{\nabla} \cdot \vec{b}(\vec{r},t) = 0 \tag{2.2}$$

$$\vec{\nabla} \times \vec{e}(\vec{r},t) = -\dot{\vec{b}}(\vec{r},t) \tag{2.3}$$

$$\vec{\nabla} \times \vec{b}(\vec{r},t) = \mu_0[\vec{j}(\vec{r},t) + \epsilon_0 \dot{\vec{e}}(\vec{r},t)], \tag{2.4}$$

where $\vec{e}(\vec{r},t)$ and $\vec{b}(\vec{r},t)$ are the microscopic electric and magnetic fields at position $\vec{r}$ and at time t, while $\eta(\vec{r},t)$ and $\vec{j}(\vec{r},t)$ are the microscopic charge and current densities respectively. The macroscopic electric and magnetic fields, $\vec{E}$ and $\vec{B}$, are obtained through averaging the microscopic fields $\vec{e}$ and $\vec{b}$ over a finite, small compared to the wavelength, volume. This is usually achieved by employing an appropriate averaging function, $f(\vec{r})$ which drops smoothly to zero outside the desired averaging volume [2]:

$$\vec{E}(\vec{r},t) = < \vec{e}(\vec{r},t) > = \int f(\vec{r}')\vec{e}(\vec{r}-\vec{r}',t)d^3r' \tag{2.5}$$

$$\vec{B}(\vec{r},t) = < \vec{b}(\vec{r},t) > = \int f(\vec{r}')\vec{b}(\vec{r}-\vec{r}',t)d^3r', \tag{2.6}$$

leading to the macroscopic Maxwell equations:

$$\vec{\nabla} \cdot \vec{E}(\vec{r},t) = < \eta(\vec{r},t) > /\epsilon_0 \tag{2.7}$$

$$\vec{\nabla} \cdot \vec{B}(\vec{r},t) = 0 \tag{2.8}$$

$$\vec{\nabla} \times \vec{E}(\vec{r},t) = -\dot{\vec{B}}(\vec{r},t) \tag{2.9}$$

$$\vec{\nabla} \times \vec{B}(\vec{r},t) = -\mu_0(< \vec{j}(\vec{r},t) > + \epsilon_0 \dot{\vec{E}}(\vec{r},t)) \tag{2.10}$$

The charge and current densities can be decomposed in two components, one including contributions from the charges, $q^{(m)}$, that can move freely (such as the free electron cloud of metals) and one resulting from the bound charge densities, $\tilde{\eta}^{(n)}$ (such as the electrons in the atomic and molecular orbitals):

$$\eta(\vec{r},t) = \sum_m q^{(m)}\delta(\vec{r} - \vec{r}^{(m)}(t)) + \sum_n \tilde{\eta}^{(n)}(\vec{r},t), \tag{2.11}$$

where the index m runs over all free electrons and index n over all atoms and molecules. After a Taylor expansion of $\tilde{\eta}^{(n)}(\vec{r},t)$ around the centre of each distribution, where only the first three terms [1] are retained and a summation over all bound charges, the averaged charge distribution can be written as:

$$< \eta(\vec{r},t) >= \rho(\vec{r},t) - \vec{\nabla}\cdot\vec{P}(\vec{r},t) + \sum_{ij}\partial_{x_i}\partial_{x_j}Q_{ij}(\vec{r},t), \tag{2.12}$$

where:

$$\rho(\vec{r},t) =< \sum_m q^{(m)}\delta(\vec{r} - \vec{r}^{(m)}(t)) + \sum_n q^{(n)}\delta(\vec{r} - \vec{r}^{(n)}(t)) > \tag{2.13}$$

is the macroscopic charge density,

$$\vec{P}(\vec{r},t) =< \sum_n \vec{p}^{(n)}\delta(\vec{r} - \vec{r}^{(n)}(t)) > \tag{2.14}$$

is the macroscopic dipole polarization,

$$\vec{p}_i^{(n)} = \sum_{l(n)} q^{(l)}\vec{r}^{(l)}(t) \tag{2.15}$$

is the electric dipole moment of the n-th bound charge distribution ,

$$\mathbf{Q}_{ij}(\vec{r},t) = \frac{1}{6} < \sum_n Q_{ij}^{(n)}\delta(\vec{r} - \vec{r}^{(n)}(t) > \tag{2.16}$$

is the macroscopic quadrupole density and

$$Q_{ij} = 3\sum_{l(n)} q^{(l)}\vec{r}_i^{(l)}(t)\vec{r}_j^{(l)}(t) \tag{2.17}$$

is the quadrupole moment of the n-th bound charge distribution. In the above relations indices i, j take values x, y, z, while index $l(n)$ runs over all charges of the n-th charge distribution.

Following a similar procedure for the current density, the averaged microscopic charge density can be approximated by:

$$< j_i(\vec{r},t) >= J_i(\vec{r},t) + \partial_t(P_i(\vec{r},t) - \sum_j \partial_{r_j}\mathbf{Q_{ij}}) + \sum_{jk}\epsilon_{ijk}\partial_{r_j}M_k(\vec{r},t), \tag{2.18}$$

where

$$\vec{J}(\vec{r},t) =< \sum_m q^{(m)}\dot{\vec{r}}^{(m)}(t)\delta(\vec{r} - \vec{r}^{(m)}(t)) + \sum_n q^{(n)}\dot{\vec{r}}^{(n)}(t)\delta(\vec{r} - \vec{r}^{(n)}(t)) > \tag{2.19}$$

[1] In accordance with common practice [3], all multipole considerations in this thesis are limited to the electric quadrupole-magnetic dipole order.

is the macroscopic current density,

$$\vec{M}(\vec{r},t) =< \sum_n \vec{m}^{(n)}\delta(\vec{r}-\vec{r}^{(n)}(t)) > \tag{2.20}$$

is the macroscopic magnetization and

$$\vec{m}^{(n)} = \sum_{l(n)} q^{(l)}(\vec{r}\times\dot{\vec{r}}^{(l)}(t)) \tag{2.21}$$

is the microscopic magnetic dipole moment.

Inserting Eqs. (2.12) & (2.18) into Eqs. (2.7) & (2.10):

$$\vec{\nabla}\cdot\vec{D}(\vec{r},t) = \rho(\vec{r},t) \tag{2.22}$$

$$\vec{\nabla}\times\vec{H}(\vec{r},t) = \mu_0(\vec{J}(\vec{r},t) + \epsilon_0\dot{\vec{D}}(\vec{r},t)), \tag{2.23}$$

where $\vec{D}$ and $\vec{H}$ are the response fields defined by the constitutive relations (up to electric quadrupole-magnetic dipole order):

$$\vec{D}(\vec{r},t) = \epsilon_0\vec{E}(\vec{r},t) + \vec{P}(\vec{r},t) - \frac{1}{2}\vec{\nabla}\bar{\mathbf{Q}}(\vec{r},t) \tag{2.24}$$

$$\vec{H}(\vec{r},t) = \frac{1}{\mu_0}\vec{B}(\vec{r},t) - \vec{M}(\vec{r},t) \tag{2.25}$$

Equations (2.22) & (2.23) are equivalent to Eqs. (2.7) & (2.10), the difference being that part of the source terms is now included in the response fields which renders the former equations similar to the microscopic equivalent of the latter equations and often proves convenient [1].

2.2 Material Parameters and Constitutive Relations

The electric and magnetic multipole moments depend on both the electric and magnetic fields as well as their derivatives through complex polarizability tensors [3]. For the needs of this work, we can restrict the following discussion to linear, homogeneous, anisotropic, non-magnetic media [4]:

$$p_i = \alpha_{ij}E_j + \frac{1}{2}a_{ijk}\nabla_k E_j + \frac{1}{\omega}g_{ij}\dot{B}_j \tag{2.26}$$

$$Q_{ij} = a_{kij}E_k \tag{2.27}$$

$$m_i = -\frac{1}{\omega}g_{ji}\dot{E}_j + \chi_{ij}B_j \tag{2.28}$$

Assuming monochromatic excitation of a periodic bulk medium with electric and magnetic fields given by $\vec{E_0}e^{(i\vec{k}\vec{r}-i\omega t)}$ & $\vec{B_0}e^{(i\vec{k}\vec{r}-i\omega t)}$, respectively, and taking into account that the macroscopic polarization and magnetization are obtained by averaging the microscopic multipole mo-

ments, the response fields can be written in Einstein notation as [5]:

$$D_i = \epsilon_0 E_i + \alpha_{ij} E_j - i(g_{ij} - \frac{1}{2}\omega\tilde{\epsilon}_{jkl} a_{kli}) B_j \tag{2.29}$$

$$H_i = -i(g_{ji} - \frac{1}{2}\omega\tilde{\epsilon}_{ikl} a_{klj}) E_j + (\frac{1}{\mu_0} - \chi_{ij}) B_i \tag{2.30}$$

The electromagnetic fields in these relations contain contributions both from the incident wave and from the medium its self. When the latter terms are ignored, then the constitutive relations become:

$$\vec{D} = \bar{\epsilon}\vec{E}_0 - i\bar{\xi}\vec{B}_0 \tag{2.31}$$

$$\vec{H} = -i\bar{\xi}^T\vec{E}_0 + \bar{u}\vec{B}_0, \tag{2.32}$$

where the constitutive tensors are given by:

$$\epsilon_{ij} = \epsilon_0\delta_{ij} + a_{ij} \tag{2.33}$$

$$\xi_{ij} = g_{ij} - \frac{1}{2}\omega\tilde{\epsilon}_{jkl} a_{kli} \tag{2.34}$$

$$u_{ij} = \frac{1}{\mu_0}\delta_{ij} - \chi_{ij} \tag{2.35}$$

Hence the electromagnetic response of any medium is completely defined by its constitutive tensors, which reflect the structure of the medium on a microscopic level. In particular, the permittivity $\bar{\epsilon}$, describes the electric polarizability of the medium, while its magnetic polarizability is usually quantified through the permeability tensor $\bar{\mu} = (\bar{u})^{-1}$. The tensor $\bar{\xi}$ expresses the excitation of electric (magnetic) response due to excitation with magnetic (electric) fields and is responsible for effects related to chirality, such as circular dichroism and optical activity [3].

Before the advent of metamaterials, the accessible values of these constitutive parameters were limited to the ones that were available in nature. Metamaterials aim to expand this domain and to achieve materials with parameters not available in nature by structuring artificial materials at a subwavelength scale. This is performed usually by assembling electromagnetic resonators in regular arrangements. At the resonant frequency, the electric and/or magnetic response of the resonators contributes significantly to the macroscopic polarization and magnetization and, consequently, to the constitutive tensors.

One of the most charasteristic examples is the engineering of strong magnetic response at high frequencies. To this end magnetic resonators, such as split-rings are employed. Close to the resonance the microscopic magnetic response, and consequently the macroscopic magnetization, varies rapidly and takes large positive and negative values. Importantly, if a similar approach is followed for the dielectric permittivity, one can obtain a medium with simultaneous negative permeability and permittivity leading to intriguing phenomena, such as negative refraction, super-resolution and backward waves [6]. However, although research efforts have focused in achieving a negative refractive index in the optical part of the spectrum, metamaterials offer the possibility to engineer a large part of different constitutive tensor components, thus achieving additional enhanced and novel functionalities.

2.3 Collective effects in metamaterials

So far, in this theoretical discussion, interactions between the constituents of metamaterials (meta-molecules) have been neglected. In this section, their role in the metamaterial response is discussed.

When considering inter-element interactions, Eq. 2.31 takes the form:

$$\vec{D}(\vec{r}) = \bar{\epsilon}\vec{E}(\vec{r}) - i\bar{\xi}\vec{B}(\vec{r}) \tag{2.36}$$

$$\vec{H}(\vec{r}) = -i\bar{\xi}^T\vec{B}(\vec{r}) + \bar{u}\vec{B}(\vec{r}), \tag{2.37}$$

where the macroscopic fields at position $\vec{x}$ now depend both on the incident field and the field at different positions. Considering that the medium is composed from discrete resonators centered at positions $\vec{x}_m$ indexed by m, we can replace to a first approximation the resonators with electric, p_m and magnetic, m_m, dipoles indexed by m and placed at positions $\vec{r}_m$. The fields $\vec{E}(\vec{r}_m)$ and $\vec{B}(\vec{r}_m)$ will include contributions, $\vec{E}_0(\vec{r}_m)$ and $\vec{B}_0(\vec{r}_m)$, from the incident field as well as contributions, $\vec{E}^{(n)}(\vec{r}_m)$ and $\vec{B}^{(n)}(\vec{r}_m)$ from every other dipole in the array, indexed by $n \neq m$:

$$\vec{E}(\vec{r}_m) = \vec{E}_0(\vec{r}_m) + \sum_{n\neq m} \vec{E}^{(n)}(\vec{r}_m) \tag{2.38}$$

$$\vec{B}(\vec{r}_m) = \vec{B}_0(\vec{r}_m) + \sum_{n\neq m} \vec{B}^{(n)}(\vec{r}_m) \tag{2.39}$$

To simplify further the discussion we will consider the special case of an isotropic non-chiral medium with no magnetic response under illumination with a plane wave with wave fields $\vec{E}_0 = (E_0, 0, 0)$ and $\vec{B}_0 = (0, B_0, 0)$. In this case, Eqs. (2.36) & (2.37) take the form:

$$\vec{D} = \epsilon\vec{E} \tag{2.40}$$

$$\vec{H} = \frac{1}{\mu_0}\vec{B}, \tag{2.41}$$

Within the dipole approximation, the electric field at site $\vec{r}_m$ due to the elements at sites $\vec{r}_n$ is given by [7]:

$$\vec{E}^{(n)}(\vec{r}_m) = \frac{e^{ik|\vec{r}_{mn}|}}{|\vec{r}_{mn}|^3}[(k^2|\vec{r}_{mn}|^2 + ik|\vec{r}_{mn}| - 1)\vec{p}_n - \\ - \frac{k^2|\vec{r}_{mn}|^2 + 3ik|\vec{r}_{mn}| - 3}{|\vec{r}_{mn}|^2}(\vec{r}_{mn}\cdot\vec{p}_n)\vec{r}_{mn}], \tag{2.42}$$

where $\vec{r}_{mn} = \vec{r}_m - \vec{r}_n$ The latter equation can be simplified considerably if we consider a single layer under normal incidence. Since the medium is periodic then the electric dipole moments will be parallel to the incident electric field and will interact with re-radiated dipole fields along the same direction:

$$E(\vec{r}_m)^{(n)} = \Lambda_{mn}p_n \tag{2.43}$$

with

$$\Lambda_{mn} = \frac{e^{ik|\vec{r}_{mn}|}}{|\vec{r}_{mn}|^3}[k^2|\vec{r}_{mn}|^2 + ik|\vec{r}_{mn}| - 1 - \\ - \frac{k^2|\vec{r}_{mn}|^2 + 3ik|\vec{r}_{mn}| - 3}{|\vec{r}_{mn}|^2}|x_m - x_n|^2] \tag{2.44}$$

If α is the electric dipole polarizability, then we can write for the dipole moments :

$$p_m = \alpha(1 + \sum_{m \neq n} \Lambda_{mn} p_n) E_0 \tag{2.45}$$

and considering that all electric moments are equivalent for a periodic planar array under normal incidence:

$$p = \frac{1}{\frac{1}{\alpha} - \sum_{m \neq n} \Lambda_{mn}} E_0 \tag{2.46}$$

Taking into account that the macroscopic polarization and magnetization are derived from averaging the electric and dipole magnetic moments respectively, then the permittivity and permeability of the medium can be written as:

$$\epsilon = \epsilon_0 + f \frac{1}{\frac{1}{\alpha} - \sum_{m \neq n} \Lambda_{mn}} \tag{2.47}$$

where f is a constant emerging during the averaging procedure of the microscopic moments in order to obtain the macroscopic polarization and in the most simple case is related to the density of the resonators. As expected, the macroscopic parameter includes contributions both from the individual constituents and from interactions between them. These contributions can be easily separated. In the case of permittivity, the single dipole, ϵ_s, and lattice, ϵ_l, contributions are given by:

$$\epsilon_s = f\alpha \tag{2.48}$$

$$\epsilon_l = f\alpha^2 \frac{\sum_{m \neq n} \Lambda_{mn}}{1 - \alpha \sum_{m \neq n} \Lambda_{mn}} \tag{2.49}$$

and the total permittivity can be written as:

$$\epsilon = \epsilon_0 + \epsilon_s + \epsilon_l \tag{2.50}$$

The contribution of the lattice effects to the response of the medium can be quantified through the dimensionless ratio w:

$$w = \frac{\epsilon_L}{\epsilon_S} = (\frac{1}{\alpha \sum_{m \neq n} \Lambda_{mn}} - 1)^{-1} \tag{2.51}$$

Hence, the lattice contribution becomes particularly strong whenever the product $\alpha \sum_{m \neq n} \Lambda_{mn}$ approaches unity. This condition can be fulfilled in a resonant fashion, whenever either the polarizability α or the lattice sum $\sum_{m \neq n} \Lambda_{mn}$ vary rapidly with frequency leading to two different regimes where strong collective effects can be observed, one related to the individual element

resonances (resonances of a) and the other to the lattice resonances (resonances of $\sum_{m\neq n}\Lambda_{mn}$).

2.4 Multipole Expansion of Electromagnetic Fields

In addition to the parametrization of the microscopic electromagnetic fields of section (2.1), multipole expansions also facilitate the parametrization of the fields scattered by localized sources. In particular, if monochromatic time dependence $\sim e^{-i\omega t}$ is assumed, Maxwell equations read:

$$\vec{\nabla}\cdot\vec{E}(\vec{r}) = \eta(\vec{r})/\epsilon_0 \tag{2.52}$$
$$\vec{\nabla}\cdot\vec{B}(\vec{r}) = 0 \tag{2.53}$$
$$\vec{\nabla}\times\vec{E}(\vec{r}) = ik\vec{B}(\vec{r}) \tag{2.54}$$
$$\vec{\nabla}\times\vec{B}(\vec{r}) = \mu_0(\vec{J}(\vec{r}) + \epsilon_0 ik\vec{E}(\vec{r})), \tag{2.55}$$

where $k = \omega/c$ and the inhomogeneous wave equations can be derived:

$$(\nabla^2 + k^2)\vec{B}(\vec{r}) = -\mu_0\vec{\nabla}\times\vec{J}(\vec{r}) \tag{2.56}$$
$$(\nabla^2 + k^2)\vec{E}(\vec{r}) = -\mu_0 ik\vec{J}(\vec{r}) + \vec{\nabla}\eta(\vec{r})/\epsilon_0 \tag{2.57}$$

The solutions to these inhomogeneous equations can be found with the help of the Green function of the wave equation:

$$G(\vec{r},\vec{r'}) = \frac{e^{ik|\vec{r}-\vec{r'}|}}{|\vec{r}-\vec{r'}|} \tag{2.58}$$

and by integrating over the sources of the relations (2.56-2.57):

$$\vec{B}(\vec{r}) = \int \vec{\nabla}\times\vec{J}(\vec{r'})G(\vec{r},\vec{r'})dr'^3 \tag{2.59}$$
$$\vec{E}(\vec{r}) = -\frac{1}{\epsilon_0}\int \vec{\nabla}\eta(\vec{r'})G(\vec{r},\vec{r'})dr'^3 + ik\int \mu_0\vec{J}(\vec{r'})G(\vec{r},\vec{r'})dr'^3 \tag{2.60}$$

Now the Green function $G(\vec{r},\vec{r'})$ can be expanded in a spherical harmonics basis Y_{lm} [1]:

$$G(\vec{r},\vec{r'}) = ik\sum_{lm} G(\vec{r},\vec{r})' j_l(kr')h_l(kr)Y_{lm}Y^*_{lm}, \tag{2.61}$$

where

$$Y_{lm}(\theta,\phi) = \sqrt{\frac{(2l+1)(l-m)!}{4\pi(l+m)!}}P_l^m(cos\theta)e^{im\phi} \tag{2.62}$$

are the spherical harmonics and

$$P_l^m(x) = \frac{(-1)^m}{2^l l!}(1-x^2)^{m/2}\frac{d^{l+m}}{dx^{l+m}}(x^2-1)^l \tag{2.63}$$

are the associated Legendre functions, while $j_l(kr)$ and $h_l(kr)$ are the spherical Bessel and Hankel functions, respectively [1]. Substituting the expanded Green function from Eq. (2.61)

into Eqs. (2.59) & (2.60) gives [8]:

$$\vec{B}(\vec{r}) = \sum_{lm}[\psi^E_{lm}\vec{l}h_l(kr)Y_{lm}(\theta,\phi) - \psi^M_{lm}\frac{i}{k}\vec{\nabla}\times\vec{l}h_l(kr)Y_{lm}(\theta,\phi)] \tag{2.64}$$

$$\vec{E}(\vec{r}) = \sum_{lm}[\psi^E_{lm}\frac{i}{k}\vec{\nabla}\times\vec{l}h_l(kr)Y_{lm}(\theta,\phi) + \psi^M_{lm}\vec{l}h_l(kr)Y_{lm}(\theta,\phi)] \tag{2.65}$$

where $\vec{l} = -i\vec{r}\times\vec{\nabla}$ is the angular momentum operator and:

$$\psi^M_{lm} = \frac{ik^2\mu_0}{l(l+1)}\int j_l(kr')Y^*_{lm}(\theta',\phi')\vec{r}'\cdot\vec{\nabla}\times\vec{J}(\vec{r}')dr^{3\prime} \tag{2.66}$$

$$\psi^E_{lm} = \frac{-ik^2}{l(l+1)}\int j_l(kr')Y^*_{lm}(\theta',\phi')[ik\mu_0\vec{r}'\cdot\vec{J}(\vec{r}')- \\ -\frac{c}{\epsilon_0}(2+\vec{r}'\cdot\vec{\nabla})\eta(\vec{r}')] \tag{2.67}$$

Equations (2.66) & (2.67) define the magnetic and electric multipole moments, respectively and are exact for arbitrary dimensions of the source [8]. In the long wavelength limit, the multipole moments can be approximated by [9]:

$$\psi^M_{lm} = \frac{ik^{l+2}}{l(l+1)(2l+1)!!}\int r'^l Y^*_{lm}(\theta',\phi')\vec{r}'\cdot\vec{\nabla}\times\vec{J}(\vec{r}')dr'^3 \tag{2.68}$$

$$\psi^E_{lm} = \frac{ik^{l+2}}{l(l+1)(2l+1)!!}\int r'^l Y^*_{lm}(\theta',\phi')[ik\mu_0\vec{r}'\cdot\vec{J}(\vec{r}')- \\ -\frac{c}{\epsilon_0}(2+\vec{r}'\cdot\vec{\nabla})\eta(\vec{r}')]dr'^3 \tag{2.69}$$

Now, the integral in Eq. (2.68) identifies with the static magnetic multipole moments, while in Eq. (2.69), if the first term in the parenthesis is neglected due to an extra order of k-dependence, the remaining terms identify with the static electric multipole moments [8]. Indeed, with some algebraic effort the first static multipole moments can be written in cartesian coordinates as [3, 8]:

$$\textit{electric dipole}: \qquad p_i = \frac{1}{i\omega}\int J_i dV \tag{2.70}$$

$$\textit{electric quadrupole}: \qquad Q_{ij} = \frac{1}{i\omega}\int (r_i J_j + J_i r_j)dV \tag{2.71}$$

$$\textit{magnetic dipole}: \qquad m_i = \frac{1}{2}\int (\vec{r}\times\vec{J})_i dV \tag{2.72}$$

$$\textit{magnetic quadrupole}: \qquad \mathbf{m}_{ij} = \frac{2}{3}\int (\vec{r}\times\vec{J})_i r_j dV \tag{2.73}$$

The omission of the term $\int r'^l Y^*_{lm}(\theta',\phi')ik\mu_0\vec{r}'\cdot\vec{J}(\vec{r}')dr'^3$ has generated a lot of controversy, since it is only valid in the long wavelength limit and only when the electric multipole moments provide the dominant contributions to electric multipole radiation [10]. Indeed, for quasi-static current configurations on toroidal solenoids it has been shown that this approximation is invalid and leads to the loss of a family of multipole moments which has been termed toroidal [10]. The

first terms of the toroidal family are [11]:

$$\textit{toroidal dipole}: \qquad \vec{\tau} = \frac{1}{10}\int [(\vec{r}\cdot\vec{j})\vec{r} - \vec{r}^2\vec{j}]d^3r \tag{2.74}$$

$$\textit{toroidal quadrupole}: \qquad T_{ik} = \frac{1}{28}[4r_i r_k(\vec{r}\cdot\vec{j}) \tag{2.75}$$

$$-5r^2(r_i J_k + r_k J_i) + 2r^2(\vec{r}\cdot\vec{j})\delta_{ik}]dV$$

The respective radiating efficiency of the first multipole moments is given by [11]:

$$\textit{electric dipole}: \qquad P_p = \frac{\omega^4\mu_0}{12\pi c}|\vec{p}|^2 \tag{2.76}$$

$$\textit{magnetic dipole}: \qquad P_m = \frac{\omega^4\mu_0}{12\pi c^3}|\vec{m}|^2 \tag{2.77}$$

$$\textit{electric quadrupole}: \qquad P_Q = \frac{\omega^6\mu_0}{160\pi c^3}\sum|Q_{ij}|^2, \tag{2.78}$$

$$\textit{toroidal dipole}: \qquad P_T = \frac{\omega^6\mu_0}{12\pi c^5}|\vec{T}|^2 \tag{2.79}$$

BIBLIOGRAPHY

[1] J. D. Jackson, *Classical Electrodynamics* (John Wiley, New York, 1975).

[2] G. Russakoff, A derivation of the macroscopic Maxwell Equations. *American Journal of Physics* **38**, 1188 (1970).

[3] R. E. Raab and O. L. De Lange, *Multipole Theory in Electromagnetism* (Clarendon Press, Oxford, 2005).

[4] E. B. Graham and R. E. Raab, Light propagation in cubic and other anisotropic crystals. *Proceedings of the Royal Society* **430**, 593 (1990).

[5] O. L. de Lange and R. E. Raab, Surprises in the multipole description of macroscopic electrodynamics. *American Journal of Physics* **74**, 301 (2006).

[6] S. A. Ramakrishna, Physics of negative refractive index materials. *Reports on Progress in Physics* **68**, 449 (2005).

[7] F. J. Garcia de Abajo, Colloquium: Light scattering by particle and hole arrays. *Reviews of Modern Physics* **79**, 1267 (2007).

[8] C. G. Gray, Multipole expansions of electromagnetic fields using Debye potentials. *American Journal of Physics* **46**, 169 (1978).

[9] A. T. Gongora and E. L. Koo, Complete multipole expansion including toroidal moments. *Revista Mexicana de Fisica E* **52**, 188 (2006).

[10] G. N. Afanasiev and V. M. Dubovik, Electromagnetic properties of a toroidal solenoid. *Journal of Physics A: Mathematical and General* **25**, 4869 (1992).

[11] C. Vrejoiu, Electromagnetic multipoles in Cartesian coordinates. *Journal of Physics A: Mathematical and General* **35**, 9911 (2002).

3. METHODS

3.1 Microwave spectroscopy

3.1.1 Microwave Networks

Microwave spectroscopy is completely analogous to optical spectroscopy the main difference being in the frequencies involved and in the measurement systems. At microwave frequencies, measurements are usually performed with vector network analyzers (VNA) that are capable of simultaneously providing both amplitude and phase information by measuring voltage at its ports. In particular, a VNA constitutes a, usually two-port, microwave network and as such it can be characterized by reflection and transmission coefficients associated with its port. More precisely, the voltage, $b1$ and $b2$, on each one of the VNA's ports can be related to the incident voltage, a_1 and a_2, on both ports by the so-called S-matrix [1]:

$$\begin{pmatrix} b_1 \\ b2 \end{pmatrix} = \begin{pmatrix} S_{11} & S_{12} \\ S_{21} & S_{22} \end{pmatrix} \cdot \begin{pmatrix} a_1 \\ a2 \end{pmatrix} \tag{3.1}$$

The physical meaning of the S-matrix components can be directly derived from Eq. 3.1. For example when the voltage in port 2 is zero ($a_2 = 0$) $S_{11} = \frac{b_1}{a_1}$, i.e. S_{11} is the reflection coefficient associated with port 1. Similarly S_{22} is the reflection coefficient at port 2, while S_{21} and S_{12} are transmission coefficients from port 1 to port 2 and from port 2 to port 1, respectively.

An alternative description of a two port network is in terms of the transmission (ABCD) matrix, which relates voltages and currents in the network's ports, in contrast to the S-matrix that involves only voltages. The components of the transmission matrix are defined as [1, 2]:

$$A = \frac{V_2}{V_1} \quad (I_1 = 0) \tag{3.2}$$

$$B = \frac{V_2}{I_1} \quad (V_1 = 0) \tag{3.3}$$

$$C = -\frac{I_2}{V_1} \quad (I_1 = 0) \tag{3.4}$$

$$D = -\frac{I_2}{I_1} \quad (V_1 = 0), \tag{3.5}$$

leading to the following relation:

$$\begin{pmatrix} V_2 \\ I_2 \end{pmatrix} = \begin{pmatrix} A & B \\ C & D \end{pmatrix} \cdot \begin{pmatrix} V_1 \\ I_1 \end{pmatrix}. \tag{3.6}$$

Although the S-parameters provide an intuitive description of the network, the importance of the ABCD matrix lies in the fact that cascaded networks can be described simply by the product

of the ABCD matrices of its components [1]. In this thesis, the S-matrix is primarily used for the characterization of the metamaterial samples, while the transmission matrix is employed during calibration calculations.

3.1.2 Experimental Setup

Microwave metamaterials were characterized in an anechoic chamber with the help of two broadband horn antennas (Schwarzbeck M. E. BBHA 9120D) (see Fig. 3.1a). Transmission and reflection measurements in the range of 2 to 18 GHz were performed by placing the samples between the two antennas and the corresponding S-parameters where recorded with a vector network analyzer (Agilent E8364B). Due to the finite size of the metamaterial samples, cross-talk between the two antennas and scattering at the edges of the samples interfere with the transmitted and reflected signals. On a first stage, this was remedied by constructing a reflecting and absorbing screen with a circular aperture where the metamaterial samples are placed. In particular, the screen consisted of a wooden panel covered on one side with a thin aluminium sheet and on both sides with thick microwave absorber. As a result, waves not directly incident on the exposed metamaterial area are absorbed by the microwave absorber, then reflected by the aluminium sheet and absorbed a second time, thus minimizing their effect on the measurements. In addition to that, the screen blocks a large part of the waves that would propagate around the metamaterial sample and would otherwise result in antenna cross-talk.

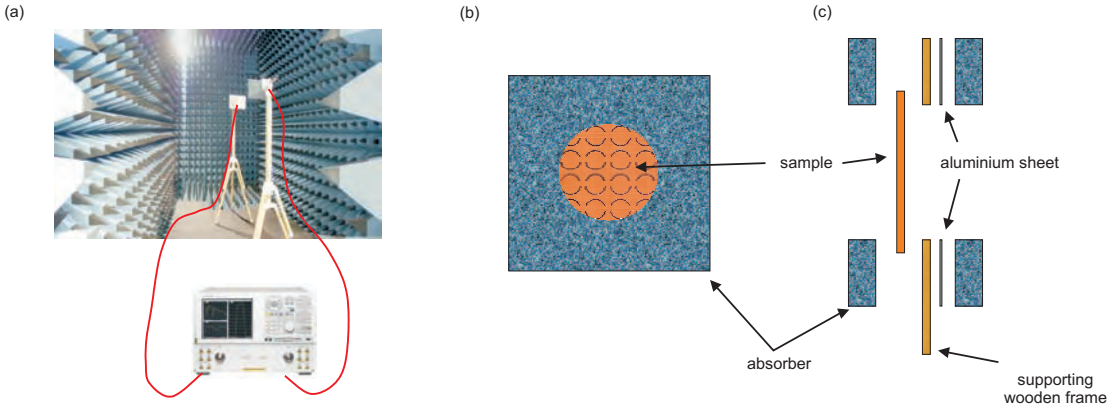

Fig. 3.1: (a) Experimental setup for the characterization of microwave metamaterials. Front (b) and side (c) view of the screen employed to minimize scattering and antenna cross-talk.

Transmission angle resolved transmission measurements, were performed in a modified microwave setup based on the same principles. The sample was placed on a rotating frame resting on a wooden table (see Fig. 3.2). On one of the table's faces a fixed absorbing screen with a circular aperture was mounted facing one of the antennas. A second, smaller, rotating, absorbing screen with a rectangular aperture was placed on the other side of the sample. The role of the first screen was to minimize antenna cross-talk and therefore a larger cross-section was needed. The smaller screen was used to minimize diffraction from the edges of the sample and a rectangular aperture was prefered in order to ensure that a sufficiently large area of the sample was illuminated. The maximum angle of incidence was limited by the sample size, as for angles of incidence near 90^0 the sample cross-section becomes increasingly small. The combination of the

fixed and rotating absorbing allowed measurements up to 75^0.

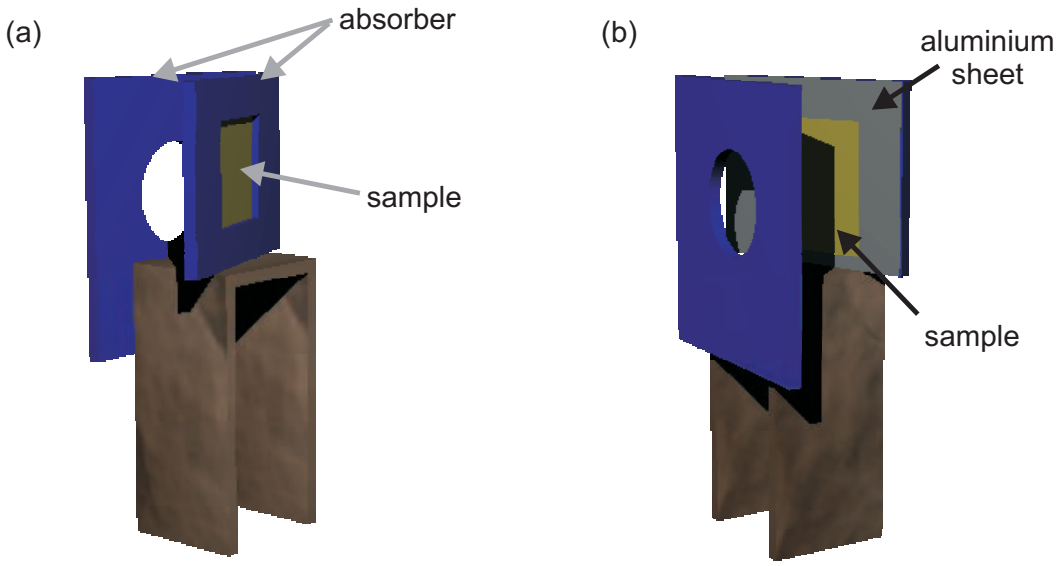

Fig. 3.2: Side views of the experimental setup used for microwave angle-resolved measurements.

3.1.3 Calibration

In general, vector network analyzer (VNA) measurements of a certain device under test (DUT) response suffer from six types of systematic errors related to: (i) directivity, (ii) crosstalk, (iii) source impedance mismatch, (iv) load impedance mismatch, (v) reflection tracking, and (vi) transmission tracking. All of these errors can be minimized by applying a two-port error correction [3]. In particular, one can think of a network analyzer as an ideal error-free network analyzer with two error boxes connected between its ports and any DUT (see Fig. 3.3). If the scattering matrices of the error boxes are given by:

$$E_A = \begin{pmatrix} a_{00} & a_{01} \\ a_{10} & a_{11} \end{pmatrix} \tag{3.7}$$

$$E_B = \begin{pmatrix} b_{00} & b_{01} \\ b_{10} & b_{11} \end{pmatrix} \tag{3.8}$$

then the transmission matrix, T_{DUT} of the device under test can be related to the measured transmission matrix, T_m, by [4, 5]:

$$T_{DUT} = \frac{b_{01}}{a_{01}} A^{-1} T_m B, \tag{3.9}$$

where the matrices are given by:

$$A = \frac{1}{a_{01}a_{10}} \begin{pmatrix} -|E_A| & a_{00} \\ -a_{11} & 1 \end{pmatrix} \tag{3.10}$$

$$B = \frac{1}{b_{01}b_{10}} \begin{pmatrix} 1 & -b_{11} \\ b_{00} & -|E_B| \end{pmatrix} \tag{3.11}$$

Connecting three known standards to port A and port B of the VNA, the components of matrices A and B can be estimated, respectively, while an extra measurement of a known standard involving both ports is required to estimate the term $\frac{b_{01}}{a_{01}}$. Although, usually mechanical standards are employed for such a calibration, here an electronic calibration kit was used, where the impedance is switched by PIN-diode or FET switches, ensuring that the calibration standards never wear out [3].

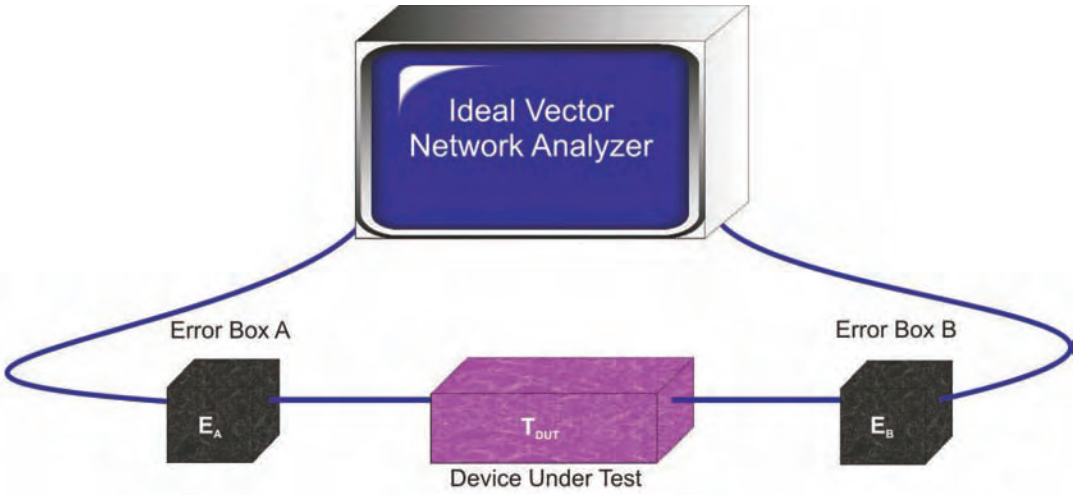

Fig. 3.3: Error adaptor model used in 2-port calibration models of vector network analyzers.

When antenna measurements are performed, then two antennas are connected to the network analyzer's ports and the "device under test" effectively includes the antennas and all components placed between the antennas. Therefore, a two-port calibration can only be performed from the VNA to the edges of the cables connecting the antennas to the VNA, and will only eliminate errors related to this path. In particular, in the case of free-space measurements additional systematic errors occur, which have to be accounted for. These errors include interference of the transmitted and reflected fields with fields scattered at the edges of the samples and at the fixture supporting the sample, multiple reflections between the antennas and between the antennas and the sample, as well as deviations of the incident wavefront from the ideal plane wave form. The most straightforward approach to solve interference errors is to ensure that the sample area is much larger than the cross-section of the incident wave. However such an approach is unrealistic, at least in the microwave regime. A more practical solution is adopted here, namely to employ a large absorbing screen to block radiation not directly incident in the sample and to damp

diffraction from the sample's edges. In addition to that, wave front related errors have been minimized by employing dielectric microwave lenses [1].

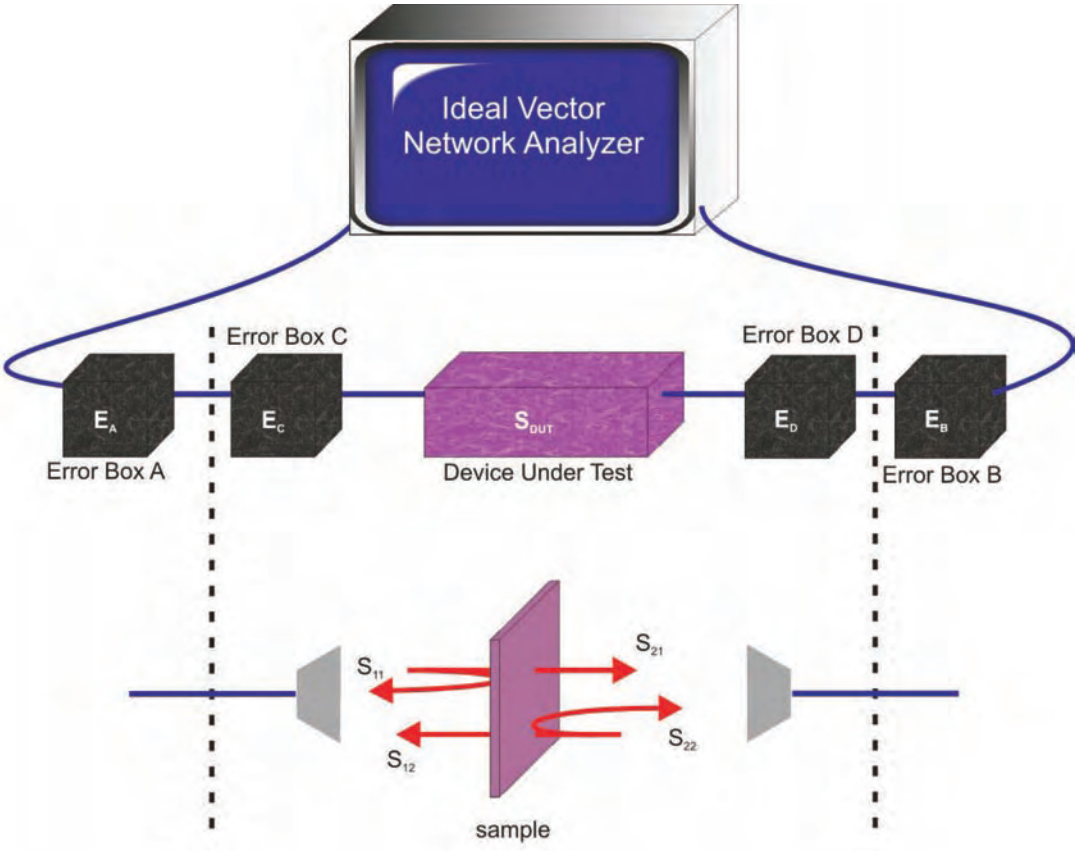

Fig. 3.4: Error adaptor model used in the gated reflect line calibration model of vector network analyzers. The DUT in this case corresponds to the antennas and the sample. The dashed lines mark the reference planes of the two-port calibration.

However, it is not easy to handle the problem of multiple reflections, which virtually renders normal incidence reflection measurements unavailable. To this end the so-called gated reflect line (GRL) calibration was employed, which is known to provide at least one order of magnitude higher accuracy compared to other methods of free-space calibration [6]. The concept behind GRL calibration is similar to the two-port calibration model, by replacing the antennas, the sample and the fixture supporting the sample by two error adaptors and a DUT, corresponding to the sample (see Fig. 3.4) . The error adaptors and the DUT are represented by the corresponding scattering matrices:

$$S_{Ec} = \begin{pmatrix} c_{11} & c_{12} \\ c_{21} & a_{22} \end{pmatrix} \tag{3.12}$$

$$S_{Ed} = \begin{pmatrix} d_{11} & d_{12} \\ d_{21} & d_{22} \end{pmatrix} \tag{3.13}$$

The first step of a GRL calibration is to estimate the values of c_{11} and d_{22} by performing

[1] designed and manufactured by E. Plum

reflection measurements with out a sample. The measurements take place in the time domain and are Fourier transformed in the time domain, where reflections originating from different sources can be distinguished. In particular, as expected the first reflection occurs at the emitting antenna, the second at the receiving antenna, while at a later time multiple reflection take place as well. By applying a gate in the time domain around the reflection response associated with the emitting antenna and repeating the procedure in the reverse direction, the error terms c_{11} and d_{11} can be determined and finally included in the original two-port calibration. By using this new calibration two known standards are measured, namely air with scattering matrix:

$$S_A = \begin{pmatrix} 0 & e^{-i\omega d/c} \\ e^{-i\omega d/c} & 0 \end{pmatrix} \tag{3.14}$$

and a metal plate with scattering matrix:

$$S_M = \begin{pmatrix} -1 & 0 \\ 0 & -1 \end{pmatrix}. \tag{3.15}$$

The measured reflections from the known standards can be related to the scattering matrices S_{Ec},S_{Ed}, S_A and S_M:

$$\Gamma_{air\ 1} = \frac{e^{-2i\omega d/c} c_{21}c_{12}d_{22}}{1 - c_{22}d_{22}} \tag{3.16}$$

$$\Gamma_{air\ 2} = \frac{e^{-2i\omega d/c} d_{21}d_{12}c_{22}}{1 - c_{22}d_{22}} \tag{3.17}$$

$$\Gamma_{metal\ 1} = -\frac{c_{21}c_{12}}{1 + c_{22}} \tag{3.18}$$

$$\Gamma_{metal\ 1} = -\frac{d_{21}d_{12}}{1 + d_{22}} \tag{3.19}$$

From this system of equation, the remaining S-parameters of the error adaptors can be determined and then embedded in the original calibration [6].

The GRL calibration was used in all microwave normal-incidence experiments reported in this thesis. Since at oblique incidence a metal plate can no longer be considered as a standard, it was not possible to apply the GRL at angle-resolved measurements and only a two-port calibration was employed in this case. The GRL calibration was performed automatically as a part of the software package 85071EU-100 provided by Agilent, which offered the opportunity for gated response measurements. During gated response measurements, the measured frequency response is Fourier transformed to the time domain. There, a gate is applied around the response of interest and then the signal is transformed back to the frequency domain. This procedure proves particularly useful for free-space normal incidence measurements, where unwanted multiple reflections provide noise and artifacts in the spectrum. The improvement on the measurements due to the GRL calibration and the gated response measurements is demonstrated in Fig. 3.5 by an example involving transmission from a planar metamaterial.

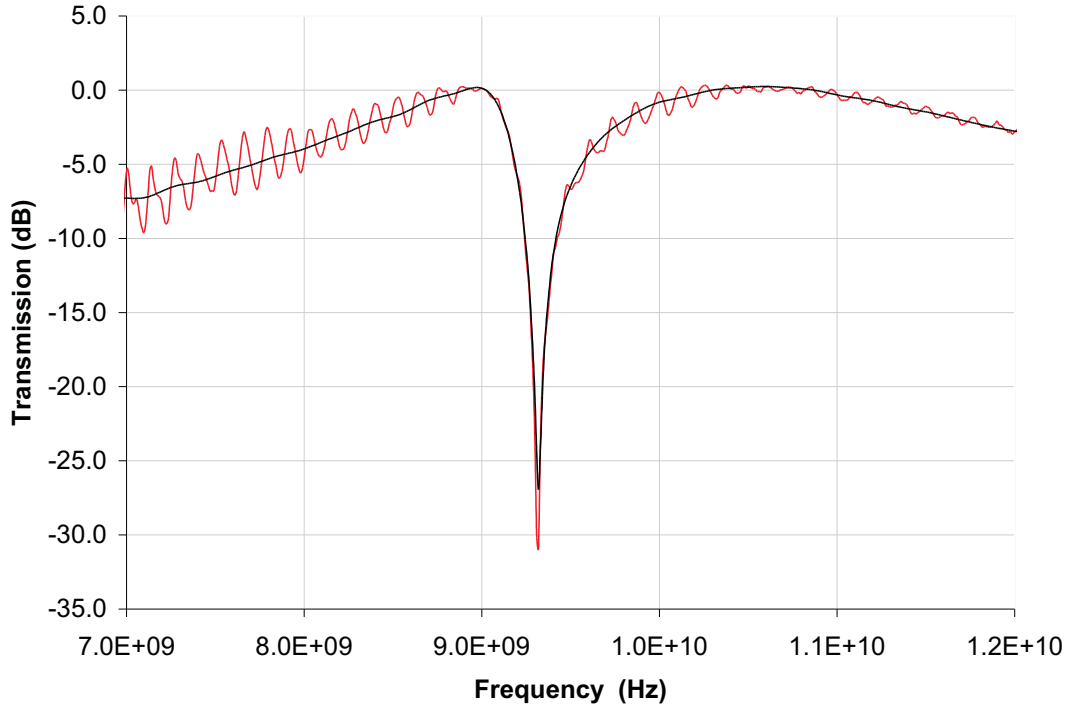

Fig. 3.5: Transmission of a planar metamaterial after a 2-port calibration (red) and a 2-port calibration followed by a GRL calibration (black).

3.1.4 Errors

In all microwave experiments a two-port calibration followed by GRL calibration was applied. Thus, the effect of systematic errors related to the VNA, cables and connectors was minimized. However, systematic errors due to interference of the transmitted and reflected fields with fields scattered at the fixture could not be accounted for entirely by the calibration a lower frequencies. On the other hand, the only alternative would involve larger absorbing screens on both sides of the sample, hence enforcing a low accuracy in the sample positioning. Thus, the measurements range was In fact, this constituted the second main source of uncertainty. In particular, a GRL calibration requires measurement of a metal plate having the same size and placed at the same position as the sample. However, there is a certain uncertainty in the positioning of the metal plate and sample. At the same time, with every change of sample small displacements of the fixture provided extra errors. Positional errors were kept below at all times 5% by measuring a metal plate after the sample measurements and performing a new calibration when the metal plate reflectivity was different from unity by more than 5%. Reducing further the effects of positioning errors would require continuous recalibrations rendering measurement times not practical. Drift errors were also observed particularly in the phase measurements but occurred at long time scales and therefore were negligible compared to the above errors. Although the source of these drift errors was probably related to temperature changes, they did not affect the measurements in significant ways and hence no systematic study was performed to clarify their origin.

3.2 Finite element analysis

Finite element analysis (FEA) is a method of numerical analysis aiming to approximately solve problems that can be formulated in terms of partial differential equations and functional minimization, such as boundary-value problems [7]. It is usually attributed to Courant [8], who applied the FEA to a torsion problem. Since then, FEA has grown in popularity, especially with the solid mechanics community. In addition, during the last decades, the elimination of spurious results together with the wide availability of powerful computers lead to numerous applications in electromagnetics problems. Furthermore, when compared to alternative numerical simulation approaches, such as the finite difference time domain (FDTD) method it presents important advantages. Perhaps the most important in view of the work presented here is the ability to handle efficiently very complex geometries, with a cost however, in computer power requirements.

3.2.1 Description

Finite element analysis is applied to the solutions of partial differential equations within a space Ω, subject to boundary conditions on its boundary $\partial\Omega$:

$$L\phi = f, \tag{3.20}$$

where L is a linear differential operator, f is the excitation and ϕ is unknown. The first step of FEA is an appropriate discretization of domain Ω and an approximation of ϕ based on its values ϕ_i in these discrete locations indexed by i and an interpolation in the whole domain Ω by a basis function N_i:

$$\phi \simeq \sum_i N_i \phi_i \tag{3.21}$$

In the Galerkin formulation, a residual is then defined [10]:

$$R = L\sum_i N_i \phi_i - f, \tag{3.22}$$

which is the difference between the approximate and exact solutions. An efficient method to minimize this residual is to average R over Ω by using appropriate weighting functions $W = \sum_j W_j$, which leads the following linear system of equations:

$$K \cdot \Phi = F, \tag{3.23}$$

where $K_{ij} = \int_\Omega W_i L N_j$, $\Phi_i = \phi_i$ and $F_i = \int_\Omega W_i f$. The system of equations (3.29) can be solved by using well established methods from linear algebra.

In the case of high frequency electromagnetics, FEA is usually applied to the wave equation for the electric (or magnetic field) over a space Ω:

$$\vec{\nabla} \times \frac{1}{\bar{\mu_r}} \vec{\nabla} \times \vec{E} - k_0^2 \bar{\epsilon_r} \vec{E} = -ik_0 Z_0 \vec{J}, \tag{3.24}$$

with boundary conditions of the type $\hat{n} \times \vec{E} = 0$ and $\hat{n} \times \vec{\nabla} \times \vec{E} = \vec{N}$ on the disjoint surface boundaries of Ω, $\partial\Omega_D$ and $\partial\Omega_N$, respectively. In this formulation, a dependence of the type

$\exp^{i\omega t}$ has been assumed, while $k_0 = \omega/c$, $\bar{\epsilon_r}$ and $\bar{\mu_r}$ are relative permittivity and permeability tensors, respectively, and $Z_0 = \sqrt{\mu_0/\epsilon_0}$ is the free-space impedance.

Equation (3.24) has infinite degrees of freedom and therefore a discretization has to take place in order to be able to address the problem numerically. During FEA the discretization is performed by approximating the domain Ω with standard geometrical shapes called elements. In two dimensions the elements of choice are often triangles, while for three dimensional problems tetrahedra are usually preferred, due to their ability to easily cover arbitrarily-shaped domains (see Fig. 3.6). The procedure of discretization (called meshing) includes also a labelling of the elements and their nodes for easy reference.

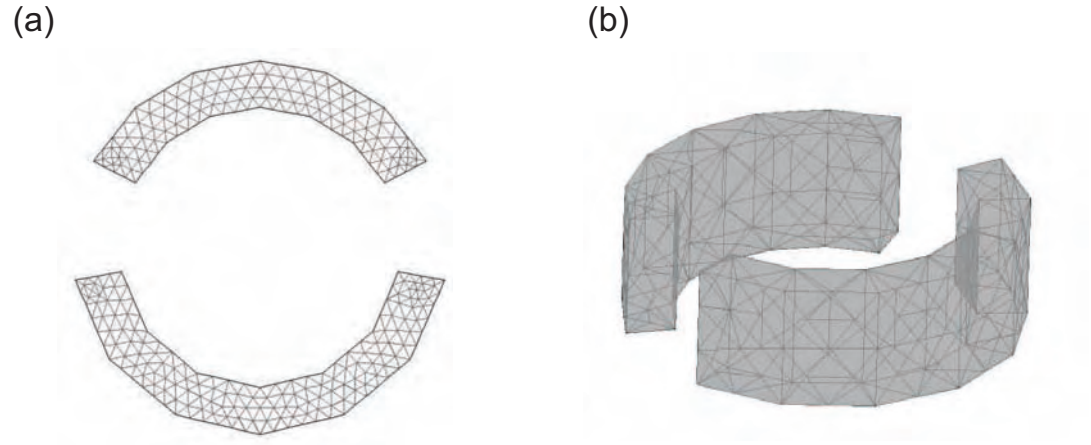

Fig. 3.6: Examples of two-dimensional (a) and three-dimensional (b) meshed employing triangular and tetrahedral mesh elements, respectively.

Once discretization has taken place, the values of $\vec{E}$ can be approximated inside each element by assigning values in certain points of the element and then use a set of interpolating basis functions to obtain a continuous approximation of $\vec{E}$. The electric field is usually assigned values at its (corners) nodes and linear interpolating functions are employed, although higher order polynomials or even vector bases can be used [9]. In particular, bases of the latter type use assigned values of the tangential electric field at the edges of the element instead of electric field values at the nodes and vector interpolating functions instead of polynomials resulting in an appealing approach which is known to minimize spurious errors [10]. Hence, within each element e, $\vec{E}$ can be approximated as [9]:

$$\vec{E}^e(x,y,z) = \sum_{i=1}^{m} \vec{N}_i^e(x,y,z) E_i^e, \tag{3.25}$$

where $\vec{N}_i^e(x,y,z)$ is the vector basis function and E_i^e is the tangential component of the electric field at edge i of element e with m nodes. Hence, summing over all element edges (excluding those at $\partial\Omega_D$ where the tangential component of $\vec{E}$ vanishes) the electric field over the entire domain Ω is obtained:

$$\vec{E} = \sum_{i=1}^{l} \vec{N}_i E_i \tag{3.26}$$

At this point Eq. (3.24) is multiplied by the so-called weighting or testing function W and integrated over the whole domain Ω leading to [9]:

$$\int\int\int_V [(\vec{\nabla}\times\vec{W})\bar{\mu}_r^{-1}(\vec{\nabla}\times\vec{E}) - k_0^2\vec{W}\bar{\epsilon}_r\vec{E}]dV = \tag{3.27}$$

$$= \int\int_{\partial\Omega} \hat{n}\cdot[\vec{W}\times(\bar{\mu}_r^{-1}\vec{\nabla}\times\vec{E})]dS - \int\int\int_V ik_0Z_0\vec{W}\cdot\vec{J}dV \tag{3.28}$$

Now the boundary conditions can be directly introduced by separating the surface integral on domains $\partial\Omega_D$ and $\partial\Omega_N$. Finally, considering that the test function can be expanded similarly to the electric field by $\vec{W} = \sum_{j=1}^{l}\vec{N}_jE_j$ and replacing in Eq. (3.27), the following linear system of equations results [9]:

$$K\cdot E = b, \tag{3.29}$$

where K is the so-called stiffness matrix given by:

$$K_{ij} = \int\int\int_V [(\vec{\nabla}\times\vec{N}_j)\bar{\mu}_r^{-1}(\vec{\nabla}\times\vec{N}_i) - k_0^2\vec{N}_j\bar{\epsilon}_r\vec{N}_i]dV - \tag{3.30}$$

$$- \int\int_{\partial\Omega}\hat{n}\cdot[\vec{N}_j\times(\bar{\mu}_r^{-1}\vec{\nabla}\times\vec{N}_i)]dS \tag{3.31}$$

and

$$b_j = -\int\int\int_V ik_0Z_0\vec{N}_j\cdot\vec{J}dV \tag{3.32}$$

3.2.2 Implementation

For the numerical simulations requirements of the work reported in this thesis a commercial software package was employed, i.e. COMSOL 3.3, which includes a graphical user interface for geometry specification and automated mesh generation and solution. An almost universal, across this dissertation, FEA model for metamaterials is presented in Fig. 3.7. The incident wave is considered to propagate along the negative z-axis, while the metamaterial extends in the xy plane. In order to simulate open space termination, the top and bottom boundaries in the xy plane are set to scattering boundaries, which are transparent to incident plane waves. To truncate the simulation domain and avoid any unwanted reflections from the scattering boundaries, perfectly matched layers (PLM), a type of anisotropic absorbers, are introduced. Such subdomains provide strong absorption with no reflection independently of incidence angle, frequency and polarization [9]. Finally, by employing periodic boundary conditions (PBC) only a single unit cell of the metamaterial structure is required in order to simulate an infinite periodic array.

3.2.3 Errors

During FEA calculations two types of error occur. The first is inherent in the approximation procedure of FEA, since the geometry domain which in general is of arbitrary shape, is approximated by elements of specific shape, while the solution is also approximated within each element by the interpolation function, which might not capture all the details of the field variation. However, both can be reduced by refining the mesh and/or by employing higher order basis functions.

In the simulations reported here, errors were reduced by successively refining the mesh and monitoring the fields at a specific boundary, At each step the new mesh was obtained by splitting

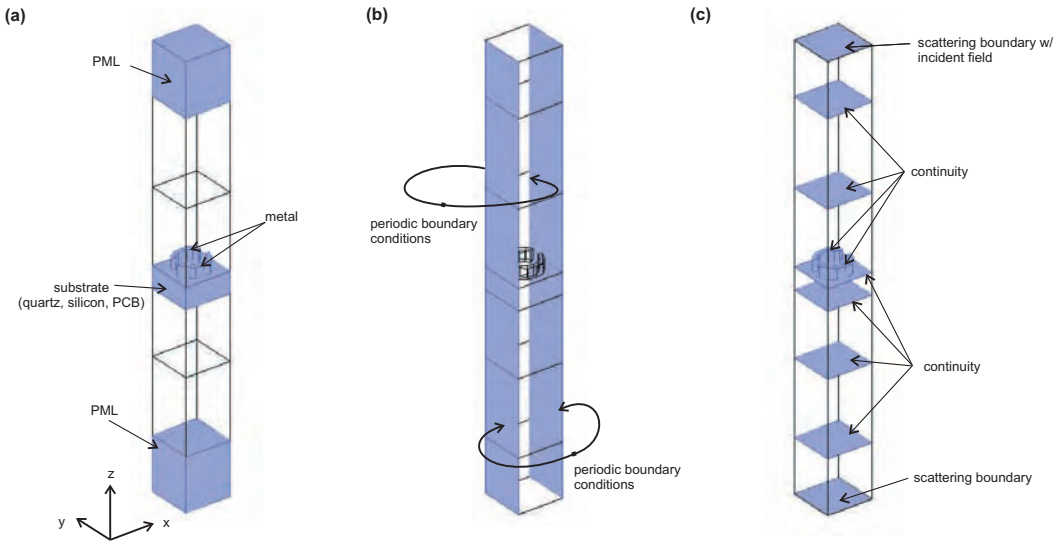

Fig. 3.7: Anatomy a FEA model: subdomain (a) and boundary (b-c) settings.

in two all elements of the mesh of the previous step. This procedure stopped when further mesh refinement returned results not different from the previous step within a 5% or smaller error margin. In most cases, comparison with experiments was possible which increased the confidence in the results.

The second type of errors is due to the finite number of digits used during the calculations. In the cases considered here, such random errors were found to be of the order 10^{-5} or smaller and were not given further consideration.

BIBLIOGRAPHY

[1] D. Pozar. *Microwave Engineering* (John Wiley, New York, 2005).

[2] Agilent AN 1287-1, *Understanding the Fundamental Principles of Vector Network Analysis* (Agilent 2000).

[3] Agilent AN 1287-3, *Applying Error Correction to Network Analyzer Measurements* (Agilent 2002).

[4] H. J. Eul and B. Schiek, A generalized theory and new calibration procedures for network analyzer self-calibration. *IEEE Transactions of Microwave Theory and Techniques* **39**, 724 (1991).

[5] A. Ferrero, Two-port network analyzer calibration using an unknown "thru". *IEEE Microwave and Guided Wave Letters* **2**, 505 (1992).

[6] P. G. Bartley and S. B. Begley, Improved free-space S-parameter calibration. *IMTC 2005 - Instrumentation and Measurement Technology Conferece* (Ottawa, Canada, 17-19 May 2005).

[7] J. Jin, *The Finite Element Method in Electromagnetics* (John Wiley, New York, 2002).

[8] R. L. Courant, Variational methods for the solution of problems of equilibrium and vibration. *Bulletin of the American Mathematical Society* **49**, 123 (1943).

[9] J. Jin and D. J. Riley, *Finite Element Analysis of Antennas and Arrays* (John Wiley, New Jersey, 2009).

[10] D. Davidson, *Computational Electromagnetics for RF and Microwave Engineering* (Cambridge University Press 2005).

4. SHARP RESONANCES IN PLANAR METAMATERIALS

4.1 Introduction

The functionality of most metamaterials (with few exceptions [1, 2]) is based on the resonant interactions of the metamaterial constituents with the incident electromagnetic radiation and the associated dispersive effects [3]. Hence, the ability to control and tune these resonances is crucial in enabling and optimizing future metamaterial devices. Although versatile applications have been demonstrated from the microwave [4, 5, 6] down to the infrared part of the spectrum, providing functional metamaterials into the visible domain remains challenging. Fabrication difficulties aside, the main obstacle appears to be the strong dissipation of metals at optical frequencies [7, 8], which broadens resonances and weakens the dispersive effects. More concisely, the result of dissipation is to decrease the strength of the resonances leading to limited functionality. In particular, losses in such composites have three sources: (i) dissipation in the metal, (ii) dissipation in the dielectric and (iii) radiative losses. In microwave down to mid-IR wavelengths, losses are mainly related to dissipation in the dielectric and scattering into free-space, while metals are still good conductors. At optical frequencies, the losses occur primarily due to the finite conductivity of the metals, as well as due to scattering. Therefore, minimizing scattering losses, e.g. coupling to free-space radiation, is important for metamaterials operating on all parts of the electromagnetic spectrum. On the other hand, metamaterials exhibiting sharp resonances can provide enhanced functionalities, such as ultra-compact slow-light devices, as well as truly-planar amplifying and lasing devices.

In this chapter, three different approaches for achieving sharp resonances are studied. Proof of principle experiments are performed in the microwave domain, while numerical simulations are employed to investigate the origin of the resonances. The optimization of the metamaterial design and the relevant limitations are also discussed.

4.2 Symmetry breaking

The response of metamaterials stems from the excitation of resonant current configurations supported by the metallic unit cell resonator. These current modes are determined by the geometry of the unit cell resonator and, in general, they share the same symmetries with the latter, similarly to the guided modes of a waveguide [9], or the propagating modes of a photonic crystal [10]. In particular, it is expected from fundamental symmetry considerations that the current density $\vec{J}(\vec{r})$ will be an eigenvector of the symmetry operators $\hat{S}$ corresponding to the symmetries of the resonator: $\hat{S}\vec{J}(\vec{r}) = \pm\vec{J}(\vec{r})$. Depending on whether the associated eigenvalue is $+1$ or -1, we can classify the current excitations as symmetric and antisymmetric, respectively. As an example consider a symmetrically split-ring (SSR) which is frequently encountered in

metamaterial research [11]. Such a resonator is invariant under reflection across a horizontal and a vertical plane. Consequently, the supported current modes will have the same symmetries. For example at the frequency of the fundamental mode, where the current forms a standing wave with two nodes at the edges of each arc, the resonator supports symmetric, dipole-like (Fig. 4.1a) and antisymmetric, ring-like (Fig. 4.1b) currents.

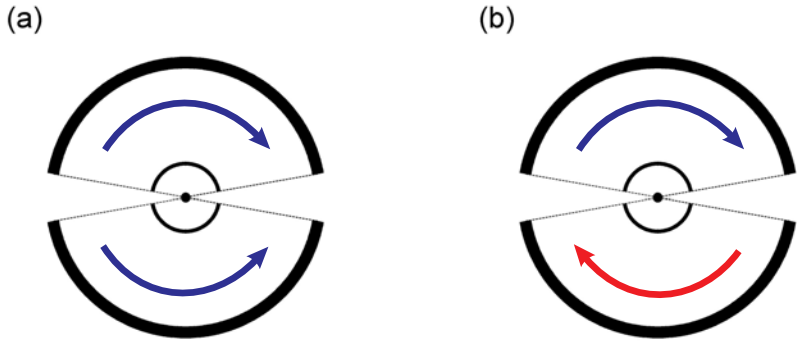

Fig. 4.1: Current modes of a symmetrically-split ring: (a) symmetric, strongly coupled to free space and (b) antisymmetric, inaccessible through free-space at normal incidence.

The symmetric current configuration is strongly coupled to free space radiation due to the strong dipole component which leads to strong scattering and short resonance life times. On the contrary, the dipole moment of the antisymmetric mode vanishes and scattering occurs only at electric-quadrupole/magnetic-dipole order or higher. This significantly enhances the lifetime of the resonance and leads to a much higher quality factor. The virtually zero coupling of this mode to the free-space radiation has led to the characterization "trapped-mode" [12]. This resonance is inaccessible at normal incidence, but it can be excited by weakly breaking the symmetry of the resonator. In particular, the symmetry of a symmetrically-split resonator (SSR) (Fig. 4.2a) can be broken in two ways, i.e. along the horizontal or vertical axis, which results in asymmetrically-split rings with unequal arc lengths (ASR type A) (Fig. 4.2b), or unequal gaps (ASR type B) (Fig. 4.2c), respectively.

The concept of symmetry breaking was studied experimentally by manufacturing two different microwave ASR metamaterials, one with different arc lengths (sample A) and one with different gaps (sample B) (see Fig. 4.3). The arc lengths of sample A corresponded to angles of 140^0 and 160^0, while the gaps of sample B corresponded to 30^0 and 10^0 angles. In both cases, the unit cell size in both cases was $15x15$ mm, while inner and outer ring radii were 5.6 mm and 6.4 mm, respectively. The metamaterial arrays were manufactured by etching a 35 mum-thick copper cladding on a 1.5 mm-thick PCB substrate with relative perimittivity $\epsilon = 4.05 - 0.05i$ [1]. As a reference, a symmetrically-split ring with arc length corresponding to a 160^0 angle was employed and its spectrum was numerically calculated.

The spectral response of type A ASRs is presented in Fig. 4.4 together with the reference

[1] Most results reported in this thesis correspond to microwave samples supported by a standard PCB substrate (FR4) with 1.5 mm thickness and relative permittivity $\epsilon = 4.05 - 0.05i$. When this is not the case, it will be explicitly mentioned.

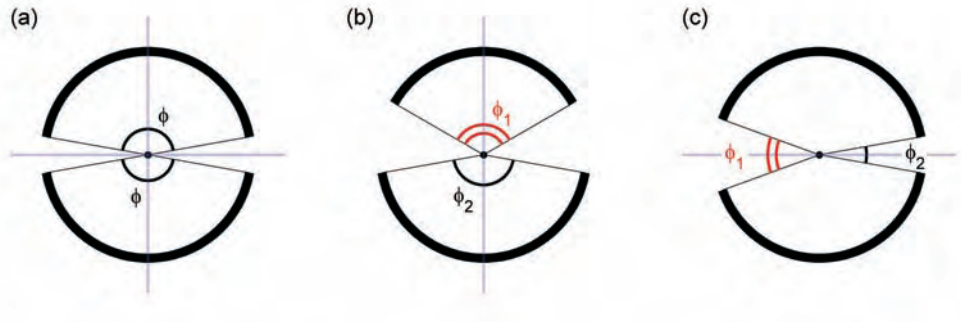

Fig. 4.2: Symmetry breaking in split rings: (a) Symmetrically-split ring (SSR). (b) Asymmetrically-split ring with different arc lengths (ASR type A). (c) Asymmetrically-split ring with different gaps (ASR type B). In each case, the dashed blue lines represent the reflection symmetry planes.

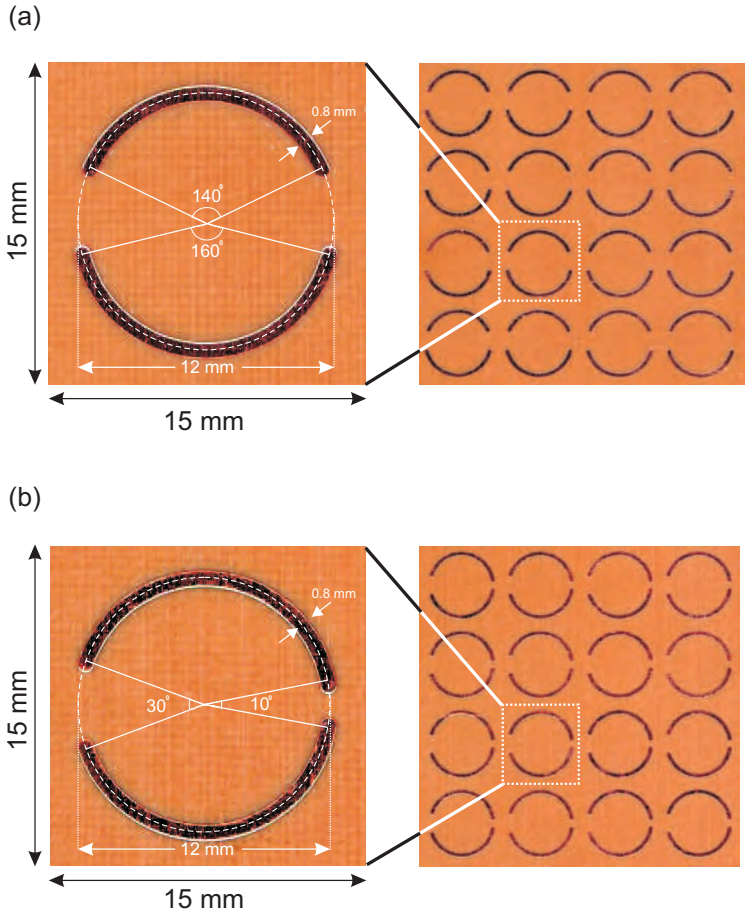

Fig. 4.3: Unit cell and fragment of the asymmetrically-split ring metamaterials: (a) ASR array with different arc lengths, (b) Asymmetrically-split ring sample with different gaps.

curve of a SSR array under illumination with a horizontally polarized wave [2] at normal incidence

[2] For the orthogonal polarization the ASR metamaterial does not exhibit sharp resonances and is almost

(see inset to Fig. 4.4). The SSR metamaterial exhibits a wide transmission stop band centered at 6.3 GHz with full width at half maximum (FWHM) of 4.6 GHz, which corresponds to a reflection peak with a quality factor $Q = 1.4$.

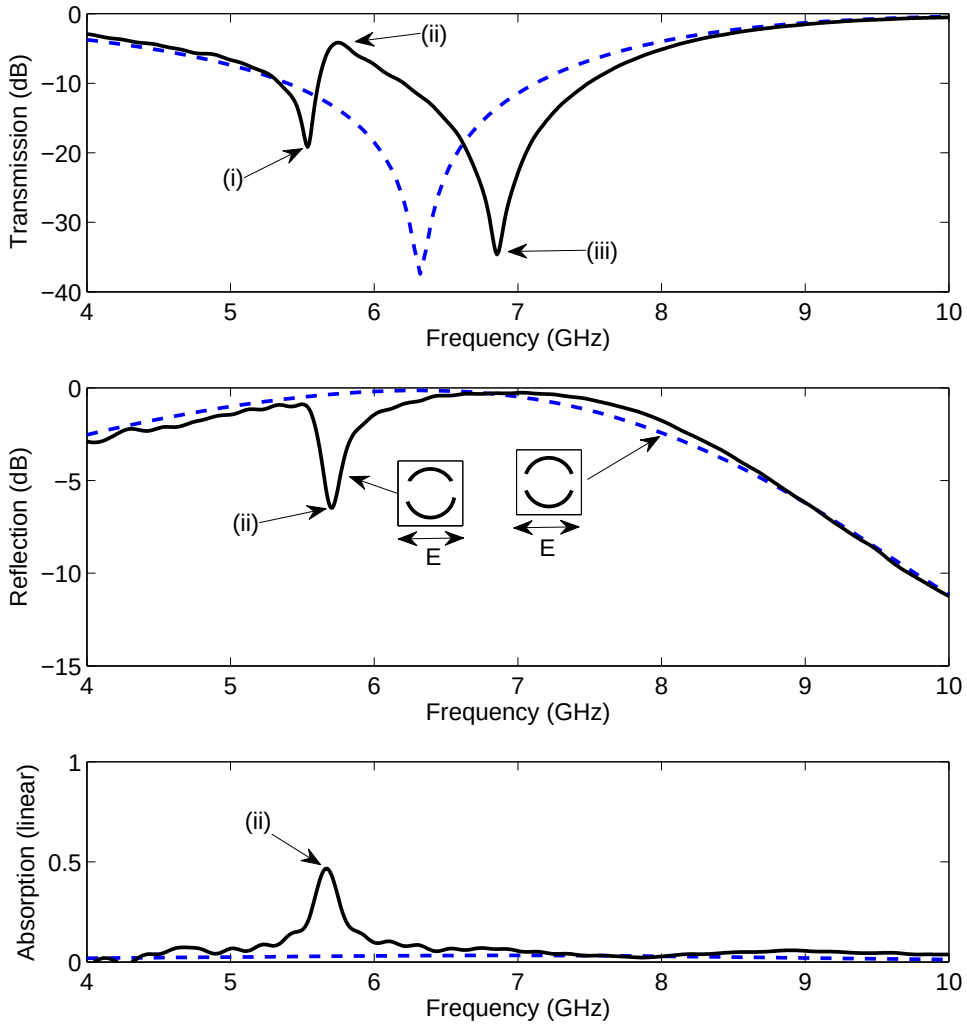

Fig. 4.4: Normal incidence response of asymmetrically-split rings with different arc lengths: (a) transmission, (b) reflection and (c) absorption. For comparison, the response of a symmetrically-split ring array is also presented (dashed blue). The transmission stop bands are marked as (i) and (iii), while the trapped-mode resonance is marked as (ii). The polarization of the incident wave is along the horizontal axis as shown on the shown in the inset to (b).

In the case of the ASR array, the stop band is split in two and three distinct features can be distinguished: (i) a low frequency transmission stop band at 5.55 GHz, (ii) a narrow pass band at 5.75 GHz and (iii) a high frequency stop band at 6.85 GHz. The Q-factor of the stop bands, features (i) and (iii), was calculated as 2.8 and 2.7, respectively. Importantly, the quality factor of the narrow pass band, feature (ii), was estimated as 16.7, almost an order of magnitude higher than those of the stop bands of both the ASR and SSR arrays. This high

indistinguishable from the SSR array.

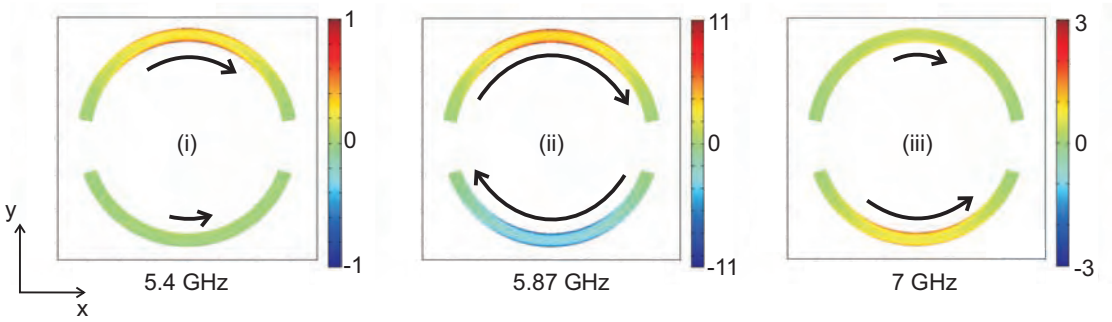

Fig. 4.5: Current modes of asymmetrically-split rings with different arc lengths at (i) the low frequency transmission stop band (5.4 GHz), (ii) the "trapped-mode" resonance (5.87 GHz) and (iii) the high frequency transmission stop band (7 GHz).

quality factor corresponds to a long resonance lifetime justifying the characterization of the resonance as "trapped". Finally, this high Q-mode coincides with a strong absorption peak, indicating that the currents and local fields are significantly enhanced at this frequency and thus more strongly absorbed. As it will be shown at a later section, this also imposes an upper limit on the practically attainable Q factors.

In order to study the origin of the observed resonances, finite element modelling was employed. The structure was modeled as infinitely thin perfectly conducting rings supported by a 1.5 mm thick PCB substrate with permittivity $\epsilon = 4.07 - i0.05$. Periodic boundary conditions were used to simulate an infinite double-periodic array. Figure 4.5 presents the horizontal component (along the x-axis) of the current density on the arcs of unit cell resonator for the case of the high-Q pass band as well as for the two stop bands. In particular, at the low frequency stop band (5.4 GHz)), both arcs are excited in phase with the longer arc dominating the response of the resonator. The situation is reversed at the high frequency stop band (7 GHz), where it is the shorter arc that is more strongly excited, while again both arcs are excited in-phase. On the contrary, at the "trapped-mode" resonance (5.87 GHz) both arcs are excited almost equally but with opposite phases. As a result the fields radiated by this antisymmetric current configuration interfere destructively in the far-field zone, thus dramatically reducing scattering losses. This leads to accumulation of energy on the split-ring in the form of strong current oscillations and enhanced local fields as indicated by Fig. 4.5.

A similar situation occurs in the case of type-B ASR metamaterial, presented in Fig. 4.6, where the normal incidence response of the metamaterial is presented. As a reference we show again the response of the SSR metamaterial. In contrast, to type-A ASRs, in the present case, the polarization of interest is the one with the electric field polarized along the vertical axis (see inset to Fig. 4.6). While the SSR metamaterial shows no sharp resonant spectral features, the ASR array exhibits a narrow reflection peak (see feature (i) in Fig. 4.6a) immediately followed by a broad transmission peak (see feature (ii) in Fig. 4.6). The width of the features is 386 MHz and 4.2 GHz leading to quality factors 13.7 and 1.31, correspondingly.

In the case of ASR with different gaps the origin of the observed resonances can be explained along the same lines as in the case of ASRs type-A. Since the metamaterial is illuminated with vertically-polarized microwaves and only this component is detected, we can restrict our explanation to the vertical component of the current configuration on the ASRs. Figure 4.7a

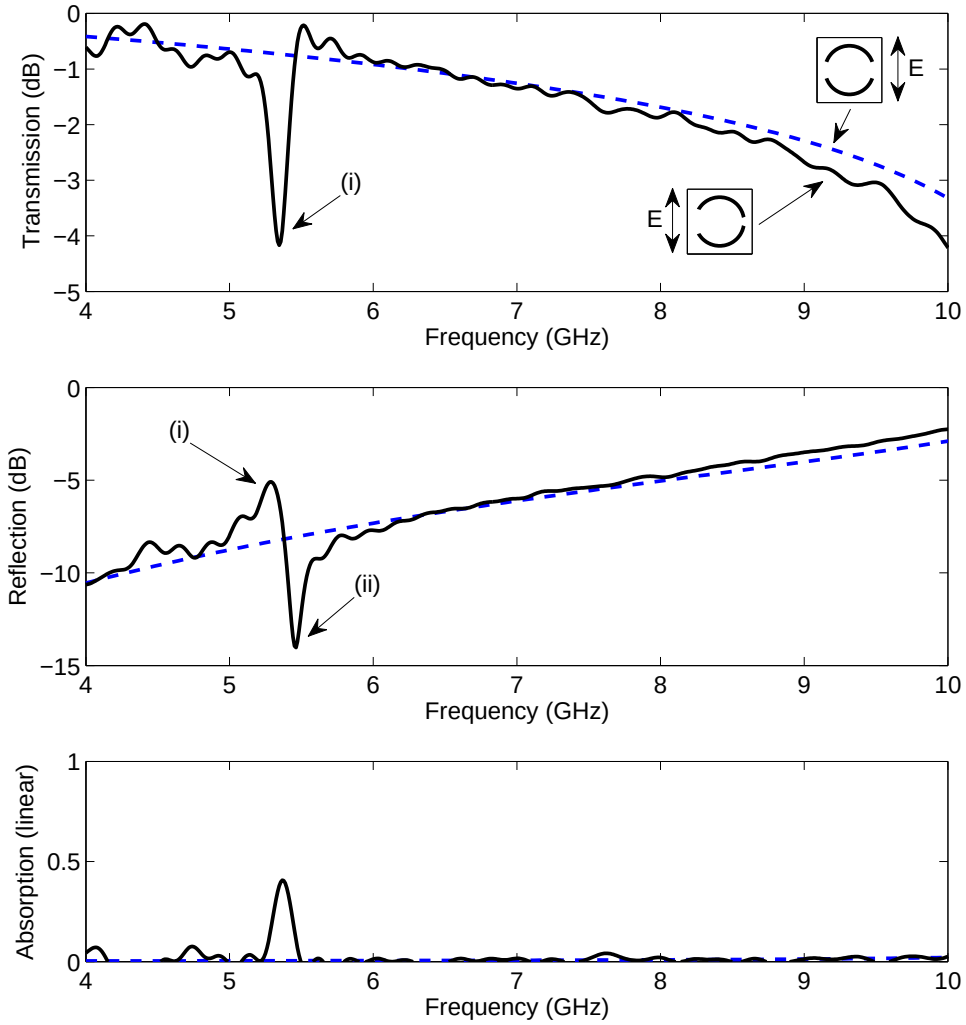

Fig. 4.6: Normal incidence response of asymmetrically-split rings with different gaps: (a) transmission, (b) reflection and (c) absorption. For comparison, the response of a symmetrically-split ring array is also presented (dashed blue). The polarization of the incident wave is along the vertical axis as shown on the shown in the inset to (a).

presents a colormap of the vertical component of the current density along the top arc of the ASR [3] for different frequencies. One can consider that the arcs of the ASR consist of two parts, a short and a long one separated by the vertical plane passing through the centre of the ring. Similarly to ASRs with different arcs, the current in these two parts flows in opposite directions. At low frequencies the longer arc is more strongly excited than the shorter one, while at high frequencies the situation reverses. When the difference in excitation strength of the two parts of the arc is maximum, then one of the arcs will radiate strongly leading to a reflection peak. This situation is illustrated in Fig. 4.7, where the full current configuration is shown. One would expect another reflection maximum occurring at high frequencies, where the shorter part of the

[3] Due to the symmetry of the ASR we can consider only one of the arcs in this discussion.

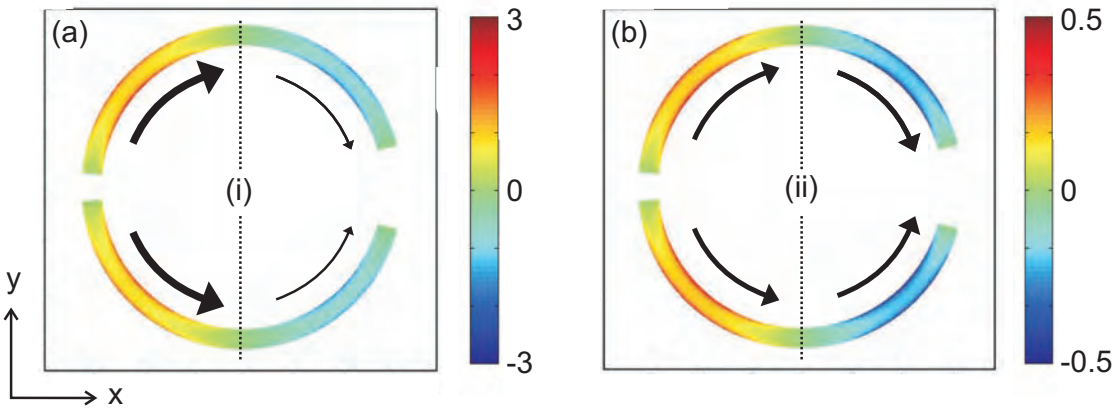

Fig. 4.7: Current modes of asymmetrically-split rings with different gaps at the transmission stop band (5.51 GHz) and pass band (5.59 GHz).

arc is excited more strongly. However, such a resonance is not observed probably due to the fact that the gap in the latter case is much wider and hence associated resonances are considerably weaker than in the former case. On the contrary, at a specific frequency, where the two parts are excited almost equally [4] this antisymmetric current configuration scatters weakly resulting in the observed transmission peak (see Fig. 4.7).

4.3 Coupled elements on the same plane

Another approach in controlling the resonance quality factor in metamaterials involves considering a unit cell consisting of two similar components,with closely spaced resonant frequencies. This is a well known approach in the design of frequency selective surfaces in order to achieve multi-band behavior [13]. A simple example of such a structure is an array consisting of pairs of concentric rings. In fact, nested-ring designs have been employed in various applications, such as filters [14, 15], reflectarray antennas [16] and off-normal incidence diplexers [17] to name a few. However, here we are interested in narrow-band spectral features and their dependence on polarisation and angle of incidence.

We manufactured a 15 mm-pitch metamaterial array of concentric rings with radii 4.5 mm and 5.45 mm, respectively (see Fig. 4.8) supported by PCB sustrate. As a reference we used an array of single rings with a radius of 5.45 mm and the same unit cell size.

In Fig. 4.9 experimentally measured transmission, reflection and absorption spectra are presented for both metamaterials. The single-ring array exhibits a behaviour typical of FSS with a 2.55 GHz-wide stop-band at 6.38 GHz ($Q = 2.5$). On the contrary, the behaviour of the concentric ring metamaterial is very similar to the ASR array type A, with a narrow transmission peak (feature(ii) in Fig 4.9a) appearing at 6.2 GHz with a width of 750 MHz, which corresponds to a Q-factor $Q = 8.3$. This peak lies between a low- and a high-frequency broad transmission stop-bands (see features (i) and (ii) in Fig 4.9a), which are associated with the excitation of the larger and the smaller ring, respectively. As expected, the pass-band corresponds to a narrow re-

[4] The short part will need to be excited slightly more strongly than the longer, in order to compensate for the difference in length.

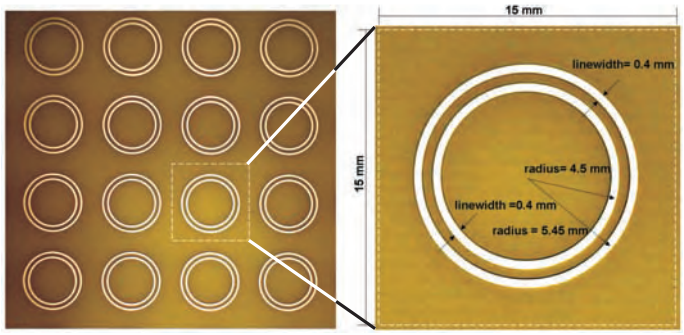

Fig. 4.8: Unit cell and fragment of the concentric ring metamaterial.

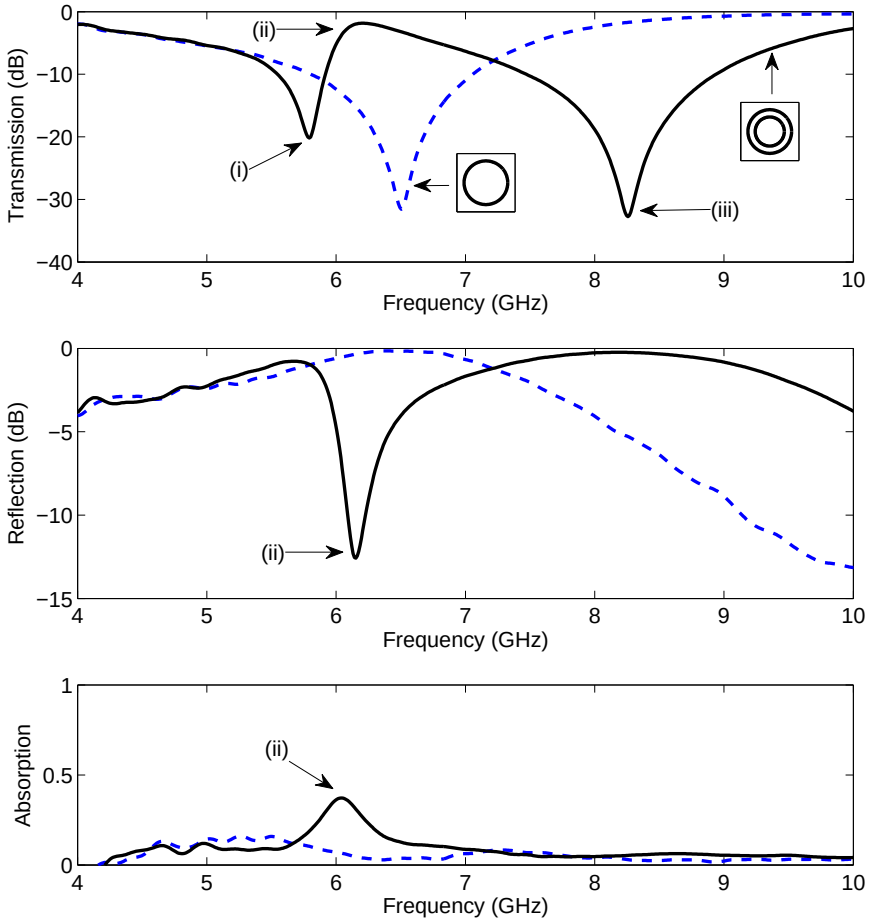

Fig. 4.9: Normal incidence response of concentric rings: (a) transmission, (b) reflection and (c) absorption. For comparison, the response of a single ring array is also presented (dashed blue).

flection dip (feature (ii) in Fig 4.9b) with increased absorption (Fig 4.9c), both typical signatures of "trapped-mode" resonances.

The corresponding, numerically simulated, current density maps are presented in Fig 4.10.

At the low frequency stopband (Fig 4.10a) the larger ring is more strongly excited than the smaller one, while the situation is reversed at the high frequency resonance (Fig 4.10c). At the trapped-mode resonance (Fig 4.10b), both rings are equally excited, but with opposite phases. As a result the radiated fields interfere destructively leading to the observed narrow pass-band. In all cases, the excitation of each ring resembles two curved dipoles oscillating in-phase, and when the two rings are equally excited the net magnetic dipole moment of the pair is zero. This is in contrast to the ASR metamaterial, where the induced ring currents lead to a strong magnetic dipole moment normal the plane of the ring. As it will be shown at a later chapter, this can lead to dramatic differences in the metamaterial response.

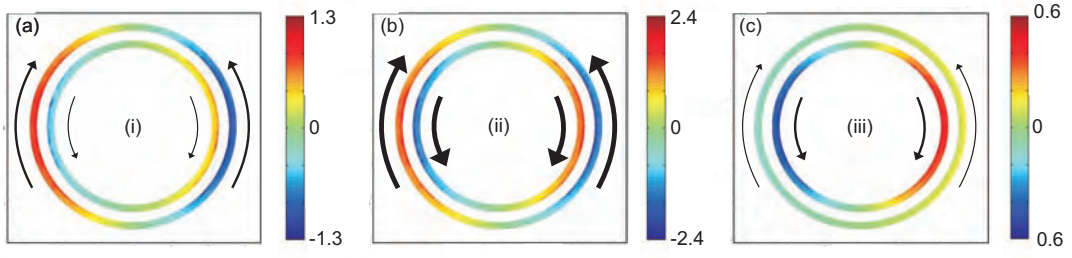

Fig. 4.10: Current modes of concentric rings at (i) the low frequency transmission stop band (5.80 GHz), (ii) the "trapped-mode" resonance (6.20 GHz) and (iii) the high frequency transmission stop band (8.25 GHz).

As a result of the unit cell symmetry this structure is insensitive to the polarisation of the incident wave. In addition to this, the concentric metamaterial is angle insensitive even for very large angles. This is demonstrated in Fig. 4.11, where experimentally measured transmission spectra, taken with a step of 5^0, are presented for transverse electric (TE) and transverse magnetic (TM) polarisation (see insets). The trapped-mode resonance (which corresponds to the red-stripe at about 6 GHz parallel to the horizontal axis) persists even at very large angles of incidence and its frequency remains virtually constant. This is clearly seen in Fig. 4.12a, where the variation in the frequency position of the trapped-mode resonance is shown for both polarisations. Even at 75^0, the position does not vary more than 3% and 1% for TE and TM polarization, respectively.

The only significant change in the spectrum is in the bandwidth of the trapped-mode resonance; Figure Fig. 4.12b presents the variation in the frequency position of the 3 dB level left and right of the transmission peak. This variation is less than 10% for all measured angles of incidence and both polarizations. The performance of the studied metamaterial compares well with other approaches aiming to achieve angle insensitivity behavior in fss [18] and outperforms by far conventional FSS [13]. At the same time, it allows for easily controllable spectral features by changing the difference between the inner and outer ring radii.

The key concept in the present approach is the interaction of two resonators with closely spaced individual frequencies. In between these frequencies, the two resonators are excited with opposite phases and an anti-symmetric current configuration is established. The similar shape of the resonators ensures that scattering from the current on one resonator is almost completely compensated by scattering from the other resonator, which leads to long resonance lifetimes

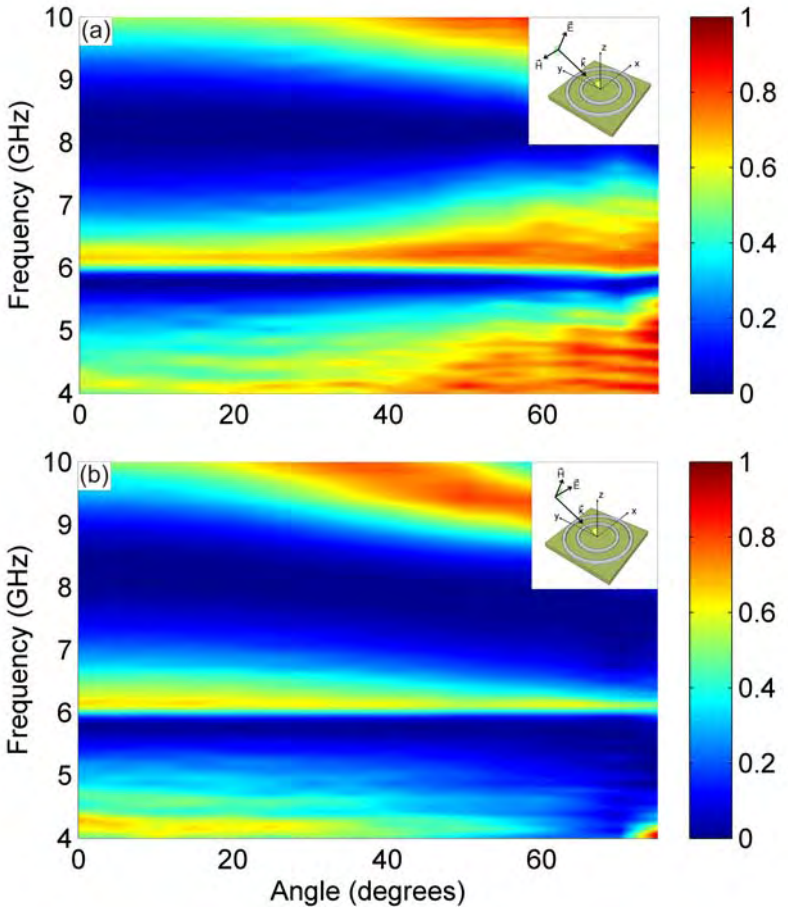

Fig. 4.11: Transmission spectra of a concentric ring array with varying angle of incidence for TE (a) and TM (b) polarization (see insets).

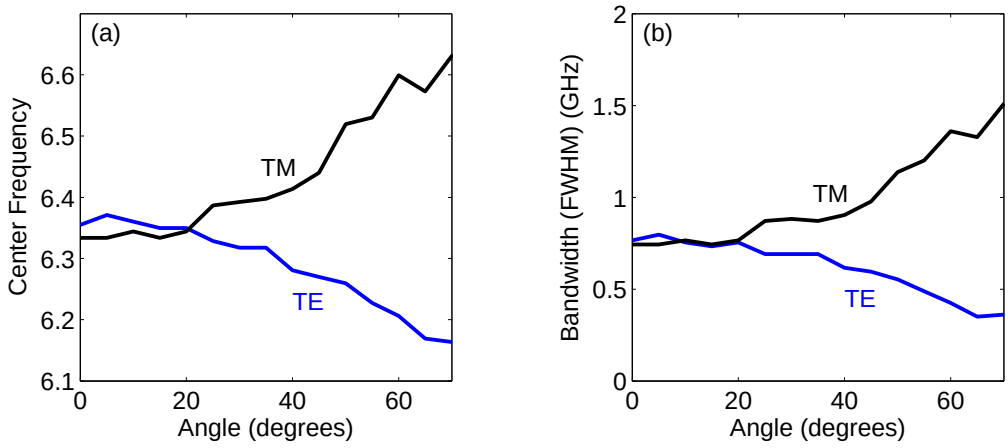

Fig. 4.12: Bandwidth (FWHM) of the concentric ring metamaterial as a function of the angle of incidence for TE (blue) and TM (black) illumination.

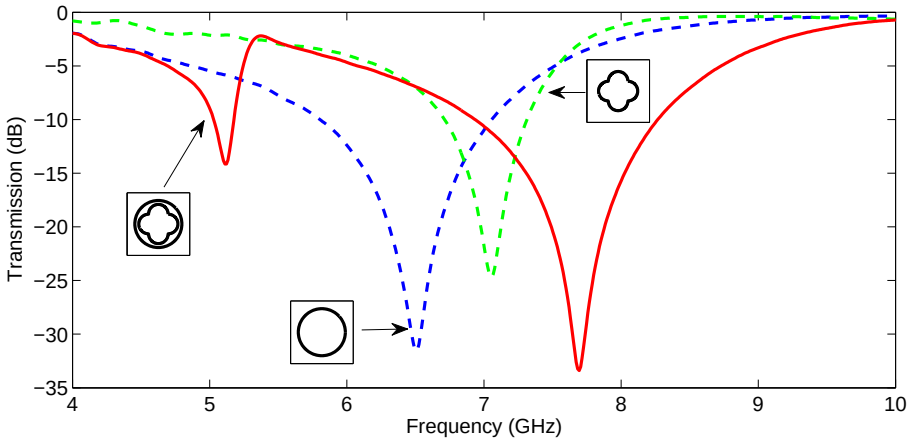

Fig. 4.13: Transmission spectra of a jerusalem cross metamaterial (dashed green), a single ring array (dashed blue), and an array of rings nested within jerusalem crosses (solid red).

and high Q-factors. However, it is not necessary for the two coupled elements to be identical, in order to achieve narrow resonances. This concept is demonstrated in Fig. 4.13, where the transmission spectra are shown for a metamaterial consisting of a jerusalem cross nested within a ring. Both the jerusalem cross and the ring resonator exhibit broad transmission stop bands at closely spaced frequencies (see dashed green and blue curves). In between these two stopbands, lies a transmission peak, typical of the trapped-mode resonance. Nevertheless, in this case the compensation is incomplete, which imposes a limit on the minimum width of the spectral features. Despite this restriction, having resonators with different shape provides yet another degree of freedom in the design of planar metamaterials.

4.4 Coupled elements on different planes

An alternative way to achieve high-Q resonances is by considering coupled elements on different planes. In this case, the interacting resonators should be identical in order to achieve near complete compensation of the respective radiated fields, while a small displacement along the propagation direction ensures that their individual resonances are not degenerate.

As a first example, a metamaterial consisting of two identical double-periodic arrays of single rings with 5.45 mm radius was employed. The two arrays were displaced along the direction of wave propagation by introducing an increasing number of standard A4 paper sheets and the resulting normal incidence reflection was measured. The results are shown in the colormap of Fig. 4.14 as a function of frequency and distance between the two arrays. Two wide reflection peaks can be distinguished: one at around 7.5 GHz that persists for all separation distances and a second one at lower frequencies ranging from 6.5 GHz to 5 GHz. In between these two reflection peaks, a narrow dip is visible (see arrows in Fig. 4.14), where reflection diminishes with increasing separating distance. This dip corresponds to the trapped-mode resonance and is a result of the displacement of the two layers. While at small separating distances this resonance can not be distinguished, it is well developed at larger distances. However, the width of the resonance also increases with increasing separating distance, since the individual resonances of

each layer are further spaced, and thus the respective quality factor drops. This trend is plotted in the inset to Fig. 4.14, where the Q-factor of the trapped mode resonance decreases from 28 at 0.6 mm to almost 5 at 2.7 mm. This provides an easy and controllable way to tune the frequency position and bandwidth of the pass band (although not independently) by simple changing the separating distance of the two layers.

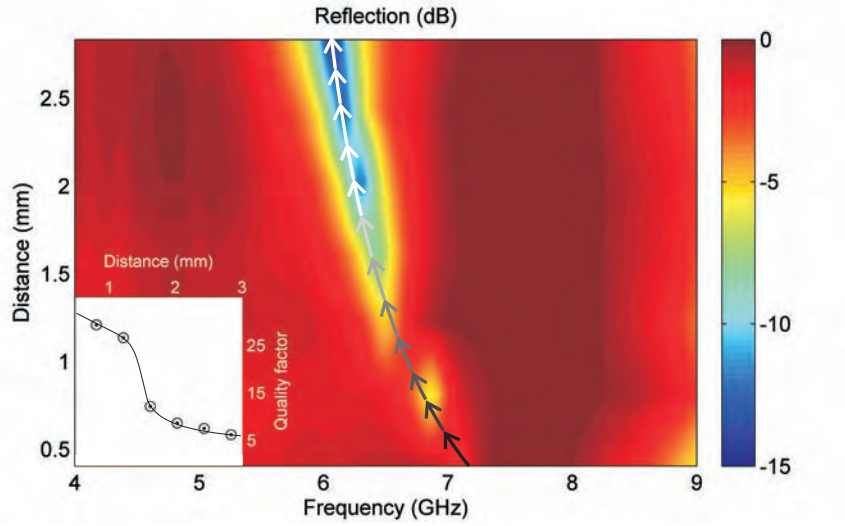

Fig. 4.14: Colormap: Normal incidence reflection of two identical regular metamaterial ring arrays separated along the propagation direction as a function of frequency and separation distance. The arrows follow the evolution of the reflection dip which corresponds to the trapped-mode resonance. Inset: Quality factor of the trapped-mode resonance as function of separating distance.

However, when very thin structures and high-Q factors are both desirable the suggested scheme is insufficient, since the trapped-mode resonance is not well developed for small separating distances. In this case, one can employ slightly different resonators to improve coupling to free-space radiation. This is illustrated by employing arrays of continuous wire patterns, termed fish-scales due to their shape (see Fig. 4.15).

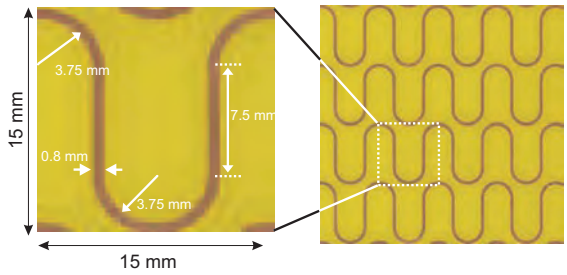

Fig. 4.15: Unit cell and fragment of the fish-scale metamaterial.

A single metamaterial array exhibits a broad reflection band typical of FSS centered at around 6.5 GHz (Fig. 4.16a). When a second identical layer is introduced, a narrow reflection dip can be distinguished (dashed-line) at around 4.5 GHz, corresponding to a weak transmission peak (Fig. 4.16b). This trapped-mode resonance becomes more visible in Fig. 4.16c), where the two

fish-scale arrays have different wire thickness (0.8 mm and 0.4 mm), since this difference further separates the resonant frequencies of the two layers. This is even more apparent in (Fig. 4.16d), where one of the layers is inverted. Here the trapped-mode resonance also moves to a higher frequency, since the inversion changes considerably the coupling of the two metamaterial layers.

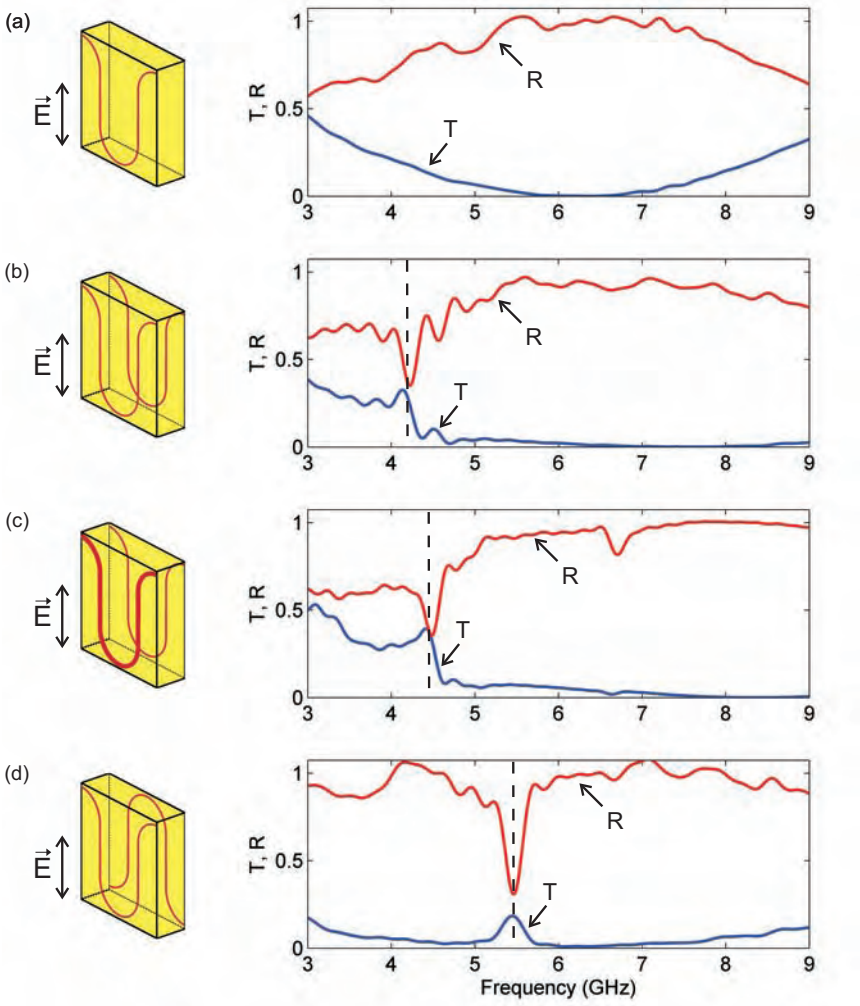

Fig. 4.16: Normal incidence transmission and reflection spectra of single-layer (a) and bi-layered fish-scales (b)-(d), where the two arrays are separated by a 1.5 mm thick dielectric. In (b) the two layers are identical, in (c) there is a small difference in the line thickness of the two arrays, while in (d) one of the layers is inverted. The dashed lines in (b)-(d) mark the position of the trapped-mode resonance.

4.5 Conclusions

In conclusion, three different approaches are discussed that aim in achieving narrow resonances in planar metamaterials based on coupling of metamaterial arrays that lie on the same or different

plane, which leads to the so-called "trapped-mode" resonances. The quality factor of these resonances can be very high at microwave frequencies, where it is only limited by the dissipation in the dielectric. However, it is expected that scaling into the optical domain will result in lower quality factors due to the strong losses associated with the metals at these frequencies.

BIBLIOGRAPHY

[1] F. Magnus, B. Wood, J. Moore, K. Morisson, G. Perkins, J. Fyson, M. C. K. Wiltshire, D. Caplin, L. F. Cohen, and J. B. Pendry. A d.c. magnetic metamaterial. *Nature Materials* **7**, 295 (2008).

[2] J. Yao, Z. Liu, Y. Liu, Y. Wang, C. Sun, G. Bartal, A. M. Stacy, and X. Zhang. Optical negative refraction in bulk metamaterials of nanowires. *Science* **15**, 321 (2008).

[3] M. I. Stockman. Criterion for negative refraction with low optical losses from a fundamental principle of causality. *Physical Review Letters* **98**, 177404 (2007).

[4] R. A. Shelby, D. R. Smith, and S. Shultz. Experimental verification of a negative index of refraction. *Science* **292**, 77 (2001).

[5] D. Schurig, J. J. Mock, B. J. Justice, S. A. Cummer, J. B. Pendry, A. F. Starr, and D. R. Smith. Metamaterial electromagnetic cloak at microwave frequencies. *Science* **314**, 977 (2006).

[6] A. V. Rogacheva, V. A. Fedotov, A. S. Schwanecke, and N. I. Zheludev. Giant gyrotropy due to electromagnetic-field coupling in a bilayered chiral structure. *Physical Review Letters* **97**, 177401 (2006).

[7] C. M. Soukoulis, S. Linden, and M. Wegener. Negative refractive index at optical wavelengths. *Science* **5**, 47 (2007).

[8] V. M. Shalaev. Optical negative-index metamaterials. *Nature Photonics* **1**, 41 (2006).

[9] D. J. Griffiths. *Introduction to electrodynamics* (Prentice Hall, 1981).

[10] J. D. Joannopoulos, S. G. Johndon, J. N. Winn, and R. D. Meade. *Photonic Crystals: Molding the flow of light* (Princeton University Press, 2008).

[11] J. B. Pendry, A. J. Holden, D. J. Robbins, and W. J. Stewart. Magnetism from conductors and enhanced nonlinear phenomena. *IEEE Transactions on Microwave Theory and Techniques* **47**, 2075 (1999).

[12] V. A. Fedotov, M. Rose, S. L. Prosvirnin, N. Papasimakis, and N. I. Zheludev. Sharp trapped mode resonances in planar metamaterial with a broken structural symmetry. *Physical Review Letters* **99**, 147401 (2007).

[13] J. C. Vardaxoglou. *Frequency selective surfaces - analysis and design* (John Wiley, Research Studies Press Ltd, 1997).

[14] E. A. Parker, S. M. A. Hamdy, and R. J. Langley. Arrays of concentric rings as frequency selective surfaces. *Electronics Letters* **17**, 880 (1981).

[15] T. K. Wu and S. W. Lee. Multiband frequency selective surface with multiring patch elements. *IEEE Transactions on Antennas and Propagation* **42**, 1484 (1994).

[16] N. Misran, R. Cahill, and V. F. Fusco. Design optimisation of ring elements for broadband reflectarray antennas. *Microwaves, Antennas and Propagation, IEE Proceedings* **150**, 440 (2003).

[17] R. Cahill, and E. A. Parker. Concentric ring and jerusalem cross arrays as frequency selective surfaces for a 45^0 incidence diplexer. *Electronics Letters* **18**, 313 (1982).

[18] G. I. Kiani, K. P Esselle, K. L. Ford, A. R. Weily, and C. Panagamuwa, *Microwave and optical technology letters* **50**, 2315 (2008).

5. INDUCED TRANSPARENCY AND SLOW LIGHT IN PLANAR METAMATERIALS

5.1 Introduction

Changes in the velocity of light propagating through dispersive media have been the subject of extensive investigations in the past [1]. However, the advances in the fabrication of artificial electromagnetic materials have lead to a renewed interest in this topic. Indeed the ability to delay a pulse by several times its width is expected to play a central role in the development of future optical technologies. One of the most promising applications is the realization of an optical buffer, where information can be stored temporarily, while it is being processed. Such a device can lead to optical routers instead of the existing electronic ones, resulting in significant increase of communication speed. In addition to buffering, slow light can enable time-domain information processing, such as multiplexing and performing convolution integrals [2]. Also, reducing the velocity of light pulses can lead to enhancement of linear and non-linear interactions [3], which in turn can improve the efficiency of a number of devices such as amplifiers, lasers, detectors, to name just a few. Common requirements [4] of slow light devices include long pulse delays (at least a few times the pulse width) over a wide bandwidth (of the order of several Gb/sec) with little distortion of the pulse shape. Furthermore, they have to be (ideally optically) tunable at a fast reconfiguration rate (at the ns scale) with low losses, although high losses can be compensated by introducing gain. Finally, they have to be compatible with existing fabrication technologies and compact for efficient integration into future devices.

Although, the first experimental studies of low group velocities appeared in the late 60's [5, 6], research in slow light exploded after the demonstration from Hau and Harris [7] of a group velocity as low as $17m/s$ in a cold sodium atom vapor by employing the quantum phenomenon of electromagnetically induced transparency (EIT) [8], where interference of a probe and a pump laser beam renders an otherwise opaque medium transparent over a narrow frequency range within an absorption line. Soon similar coherent quantum phenomena were employed to generate slow light in different types of media, such as crystalline solids [9, 10] and quantum wells [11]. However, this approach was restricted to the available material resonances, while most of the proposed techniques, involved special and often cumbersome experimental conditions, such as cryogenic temperatures and the use of high intensity laser sources. This obstacle was surpassed by appealing to classical analogs of EIT. Indeed, it was suggested that classical systems such as plasmas [12, 13, 14], electrical circuits and even mechanical spring-mass oscillators [15] can demonstrate behaviour analogous to EIT. In particular, the implementation of EIT-like effects in optical resonators has proved of high importance in terms of applications, since in this case the operating frequency can be tuned simply by varying the system geometry (scaling), while no pumping or cooling is necessary. It was proposed that classical field interference in coupled

resonators can lead to EIT-like and slow light behaviour [16, 18, 17]. Experimental investigations involved typical arrangements, where a dielectric waveguide is coupled to a dielectric resonator chain, which can extend in a direction parallel [19, 20] or perpendicular to the waveguide [21, 22]. In parallel, slow light was also demonstrated in other classical systems, such as photonic crystals [23] and photonic crystal waveguides [24, 25]. Although these approaches lead to demonstration of considerable delays they suffer from the restraints of a constant delay-bandwidth product, i.e. the price for low group velocities is narrow bandwidth, which is inherent in all resonant phenomena. This obstacle was surpassed by dynamically tuning the system, while light propagates in the structure [26, 27] enabling even storing and retrieving light pulses at will. Very recently, slow light has been also demonstrated in optical fibers, where wide bandwidth tunable delays were observed tuned at a very rate much faster than previous approaches [28, 29]. However, theoretical studies have suggested that the maximum achievable delay is roughly proportional to the refractive index contrast. Therefore, metal-based metamaterials arise as a candidate for the realization of practical devices and in fact it has been predicted that light can be delayed or even stopped in metamaterial waveguides [30], although an experimental verification for the latter is pending. Nevertheless, a fundamental drawback of all approaches to slow light sofar is their dimension along the light propagation direction which hinders on-chip integration for future devices. For example, the length of a typical photonic crystal- or optical fiber-based optical buffer should be several meters long [2, 31], while a typical chip has a footprint of a few μm^2. Therefore, orders of magnitude reduction of size is needed before such applications can be realized.

Here, an alternative approach is presented based on the concept of planar "trapped-mode" metamaterials introduced in chapter 4. It is shown that considerable pulse delays can be achieved in such structures which have vanishing thickness along the propagation direction. Moreover, it is suggested that the electromagnetic behaviour of planar metamaterials may represent a classical analog of EIT. Finally, we demonstrate that significant bandwidth enhancement can be achieved by cascading the suggested metamaterial design, while the resulting structure is still of subwavelength thickness, thus paving the way to the realization of extremely compact optical components with high integration efficiency.

5.2 Slow light propagation

Light pulses propagate through dispersive media with a velocity different than the phase velocity, $v_p(\omega) = c/n(\omega)$, where $n(\omega)$ is the refractive index at frequency ω. This pulse velocity is usually called group velocity [1], v_g and is defined as: index [1]:

$$v_g = \frac{d\omega}{dk},$$

or

$$v_g = \frac{c}{n + \frac{dn}{d\omega}}, \tag{5.1}$$

where k is the complex wavenumber.

In fact, it was predicted [32] and later observed [33, 34] that the group velocity can be much

[1] The group velocity does not always coincides with the information velocity. For example, at an absorption resonance the group velocity can be greater than c, although information can not be transmitted at that speed [1].

smaller or greater than c without strong distortion due to pulse reshaping phenomena. From Eq. 5.1 it follows that in order to achieve slow light propagation, i.e. low group velocities, one has to maximize the refractive index and/or its first derivative with respect to frequency. Usually, one has little control over n, but by operating in frequency regions of strong dispersion, such as a sharp resonance or the band-edge of a crystal, very high values of $\frac{dn}{d\omega}$ and consequently long pulse delays are possible. Indeed, the real, $Re[n]$, and imaginary, $Im[n]$, part of the refractive index, which control the dispersion and the absorption, respectively, that a wave traveling through a medium experiences, are not independent. More concisely, causality requirements lead to the Kramers-Kronig relations:

$$Re[n(\omega)] = 1 + \frac{c}{\pi} P \int_0^\infty \frac{Im[n(\omega')]}{\omega^2 - \omega'^2} d\omega' \tag{5.2}$$

A well known consequence of Eq. 5.2 is the anomalous dispersion observed at absorption resonances, which results in pulse advance [1][2]. Inversely, one would expect that sharp normal dispersion would occur at a narrow minimum of loss or a maximum of gain. This behaviour is illustrated in Fig. 5.1, where two characteristic cases of anomalous and normal dispersion are presented.

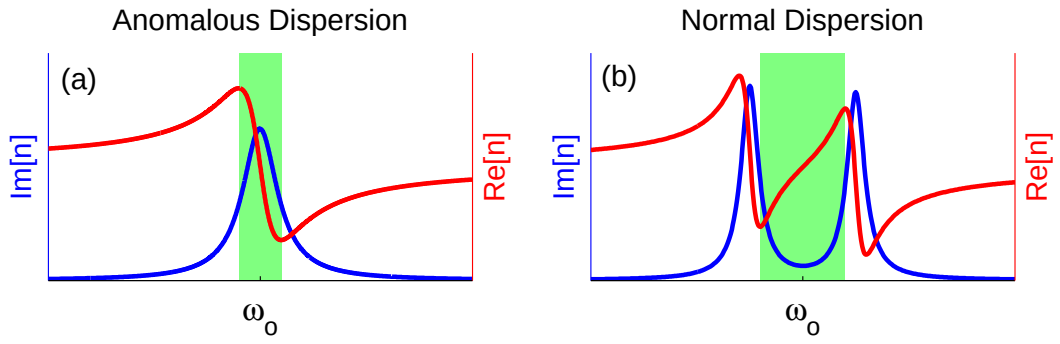

Fig. 5.1: Real (red) and imaginary (blue) part of the refractive index for (a) single Lorentz oscillator and (b) two Lorentz oscillators with slightly different frequencies.

Another consequence of the Kramers-Kronig relations is that one cannot have very sharp dispersion over a wide bandwidth, i.e. very steep dispersion can occur only at the expense of bandwidth. This limitation is quantified by the so-called delay-bandwidth product, which is constant for a given physical process and it constitutes a popular figure of merit for comparing different slow light mechanisms.

As expected, a pulse whose spectrum lies entirely within the frequency region of normal dispersion will be delayed, but retaining its shape. However, if the pulse spectral width extends outside this region, then distortion will take place, since, if we consider the pulse as an ensemble of monochromatic components, then due to the fact that the group velocity will vary with frequency, different pulse components will be delayed by different amounts and the pulse envelope

[2] In this case, the signal does not actually propagate faster than the speed of light (this would violate causality), but rather it is reshaped in such a way that the maximum of the transmitted pulse is shifted *within the envelope of the incident pulse*

will broaden. This broadening is quantified by the group velocity dispersion, GVD, defined as:

$$GVD = \frac{d^2k}{d\omega^2}, \tag{5.3}$$

Similar will be the effects of higher order dispersion terms, while the dispersive nature of the absorption will also contribute to distortion. This will limit the available bandwidth and consequently decrease the delay-bandwidth product. In order to take into account the limitations that arise from distortion, in the following discussion, we will consider as a figure of merit the fractional delay, namely the ratio of pulse delay over the width (full width at half maximum) of the transmitted pulse. The minimum pulse duration (and consequently the bandwidth) will be limited by the requirement that, in order for two pulses to be distinguished, their peaks have to be separated in time by at least one pulse width (FWHM).

5.3 Electromagnetically Induced transparency

Electromagnetically induced transparency (EIT) is a coherent non-linear quantum phenomenon that occurs in atomic media due to quantum interference of two laser beams tuned at different atomic transitions. A detailed analysis of EIT lies beyond the scope of the thesis. Instead, it will suffice to mention the fundamental characteristics of EIT by appealing to a simplified EIT system which will allow us to draw the analogy with metamaterial systems later on. In this brief introduction we will mainly follow the recent review by Fleischhauer et al. [35]. Finally, it will be assumed that the response of the atomic system is parallel to the electric field of the incident waves, so that we can avoid the complications of a vector consideration.

As an example we will consider a so-called Λ atomic system, which consists of three states, i.e. $|1>$ (the ground state), $|2>$ (the excited state) and $|3>$ (a metastable state). The excited state is dipole-coupled to both states $|1>$ | and $|3>$, with corresponding resonant frequencies ω_{21} and ω_{23}, respectively, while transitions from state $|3>$ to state $|1>$ are not allowed. This is illustrated in Fig 5.2a. The atomic system interacts with two laser beams: a weak probe E_p with frequency $\omega_p = \omega_{21} + \delta$, where δ is a small detuning from the $|1> \rightarrow |2>$ transition, and a strong pump beam E_c with frequency $\omega_c = \omega_{23}$ applied the $|2> \rightarrow |3>$ transition. We are interested in the linear response of the atom vapor to the probe field E_p which will be given by the real (χ') and imaginary (χ'') part of its relative susceptibility $\chi(\omega_p)$:

$$P(\omega_p) = \epsilon_0(\chi'(\omega_p) + i\chi''(\omega_p)]E_p, \tag{5.4}$$

where $P(\omega_p)$ is the induced polarization. The latter is related to the off-diagonal elements (coherences), ρ_{21}, ρ_{23} of the system's density matrix by:

$$P(\omega_p) = \frac{N_{atom}}{V}[d_{12}\rho_{21}e^{-i\omega_{21}t} + d_{32}\rho_{23}e^{-i\omega_{23}t} + c.c.], \tag{5.5}$$

where $\frac{N_{atom}}{V}$ is the atomic density, d_{12} and d_{32} are the dipole moments associated to transitions $|1> - |2>$ and $|3> - |2>$, respectively, while *c.c.* stands for complex conjugate. The coherences

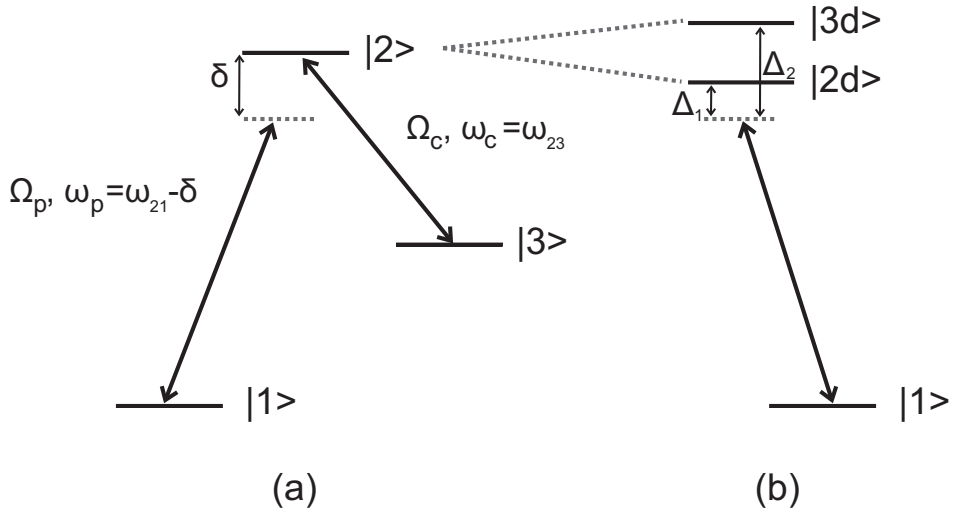

Fig. 5.2: (a) A Λ-system under the bare picture. The excited state $|2>$ is coupled to the ground state $|1>$ by a probe beam of strength Ω_p and frequency ω_p, detuned from the resonant frequency ω_{21} by a small amount δ. A pump beam of strength Ω_c and frequency $\omega_c = \omega_{23}$ resonantly couples the excited state $|2>$ to the metastable state $|3>$. (b) Under the dressed state picture, the effect of the pump beam is considered to induce a splitting of the excite state $|2>$ to the (dressed) states $|2d>$ and $|3d>$. The detuning of the probe beam from the dressed states is denoted by Δ_1 and Δ_2, respectively.

can be found by solving the Liouville equations of motions:

$$\rho_{23} = \frac{i\Omega_c e^{i\delta t}}{\gamma}\rho_{13} \tag{5.6}$$

$$\rho_{13} = \frac{\Omega_c}{2\delta}\rho_{21}^* \tag{5.7}$$

$$\rho_{21} = \frac{i\Omega_p e^{i\delta t}}{\gamma + 2i\delta} + \frac{i\Omega_c}{\gamma + 2i\delta}\rho_{13}^* \tag{5.8}$$

The linear susceptibility can then be estimated by retaining only terms linear in $e^{i\omega_p t}$:

$$\chi \sim d_{12}\rho_{21}e^{-i\omega_{21}t}, \tag{5.9}$$

or

$$\chi' \sim |d_{12}|^2 \frac{4\delta(\Omega_c^2 - 4\delta^2)}{(4\delta^2 - \Omega_c^2)^2 + 4\delta^2\gamma^2} \tag{5.10}$$

and

$$\chi'' \sim |d_{12}|^2 \frac{8\delta^2\gamma}{(4\delta^2 - \Omega_c^2)^2 + 4\delta^2\gamma^2}, \tag{5.11}$$

where γ is the coherence decay rate of state $|2>$, while dephasing of state $|3>$ is considered negligible. The most striking characteristic of Eq. 5.11 is that the imaginary part, χ'' of the susceptibility vanishes for zero detuning of the probe, $\delta = 0$, meaning that no absorption occurs at resonance. Note that this is possible only due to the effect of the pump beam. Indeed, for $\Omega_c = 0$,

Eq. 5.11 reduces to $\chi'' \sim |d_{12}|^2 \frac{2\gamma}{4\delta^2+\gamma^2}$, which is takes its maximum value for $\delta = 0$. This cancellation of absorption can be explained in terms of interference of different excitation pathways. In a semiclassical picture the coherences express the oscillating dipole moments induced by the applied electromagnetic fields. Then, the origin of the interference can be traced on the second term of Eq. 5.8, where the pump beam couples ρ_{21} associated with the $|1> \rightarrow |2>$ transition to ρ_{13} and ρ_{23} through Ω_c. These two terms express the interference between the direct excitation pathway $|1> \rightarrow |2>$ and an indirect via state $|3>$, $|1> \rightarrow |2> \rightarrow |3> \rightarrow |2>$. Although the latter has weak probability of occurring, this is compensated by the large amplitude of the pump field. On the other hand, the strong probability of the former direct excitation is restrained by the low intensity of the probe beam. This interference becomes more evident if we transfer in the dressed state picture. In this framework, the effect of the pump is reduced to a splitting of the resonance at which the probe beam is tuned, which now experiences two new dressed states $|2d>$ and $|3d>$ whose energies have shifted approximately by $\pm\hbar\Omega_c/2$ from the energy of state $|2>$ (see Fig. 5.2b). If we denote the detunings of the probe beam from the dressed states as $\Delta_1 = \omega_{21} + \Omega_c/2 - \omega_p$ and $\Delta_2 = \omega_{21} - \Omega_c/2 - \omega_p$ respectively, then the susceptibility can be readily written as:

$$\chi' \sim |d_{12}|^2 \frac{\Delta_1\Delta_2(\Delta_1+\Delta_2)}{4\Delta_1^2\Delta_2^2 + \gamma^2(\Delta_1+\Delta_2)^2} \tag{5.12}$$

and

$$\chi'' \sim |d_{12}|^2 \frac{\gamma(\Delta_1+\Delta_2)^2}{4\Delta_1^2\Delta_2^2 + \gamma^2(\Delta_1+\Delta_2)^2} \tag{5.13}$$

In this form, the contributions from the two dressed states through the detunings Δ_1 and Δ_2 become obvious, while the appearance of the sum $\Delta_1 + \Delta_2$ in the nominator of the susceptibility directly shows the quantum interference. At zero detuning from the bare excited state, the dressed states contribute with opposite phases in the susceptibility and exactly compensate one another leading to zero absorption. At the same time due to Kramers Kronig restrictions, the real part of the susceptibility exhibits strong dispersion. In fact, for small detunings, the dispersion of the real part of the susceptibility, is inversely proportional to the splitting of the dressed states $d\chi'/d\omega \sim (\Delta_1 - \Delta_2)^{-2}$, meaning that smaller splittings (i.e. weaker pump field) leads to sharper dispersion.

5.4 Pulse Delays in Microwave Trapped Mode Metamaterials

The sharp resonances exhibited by the trapped-mode metamaterials (see chapter 4) provide an ideal opportunity to realize pulse-delaying schemes in very thin media. In contrast to all other approaches, where constraints are introduced in the minimum thickness of the medium, the thickness of planar metamaterials along the propagation direction is many times smaller than the wavelength and is only limited by fabrication requirements. As an we will investigate the dispersion properties of the bi-layered fish-scale metamaterial, where the front and back layers are displaced along the lateral direction by half a unit cell with respect to one another. As it will be shown, this particular design allows for low distortion pulse delays, while it can also be cascaded by successive stacking of metamaterial slabs leading to significant bandwidth increase.

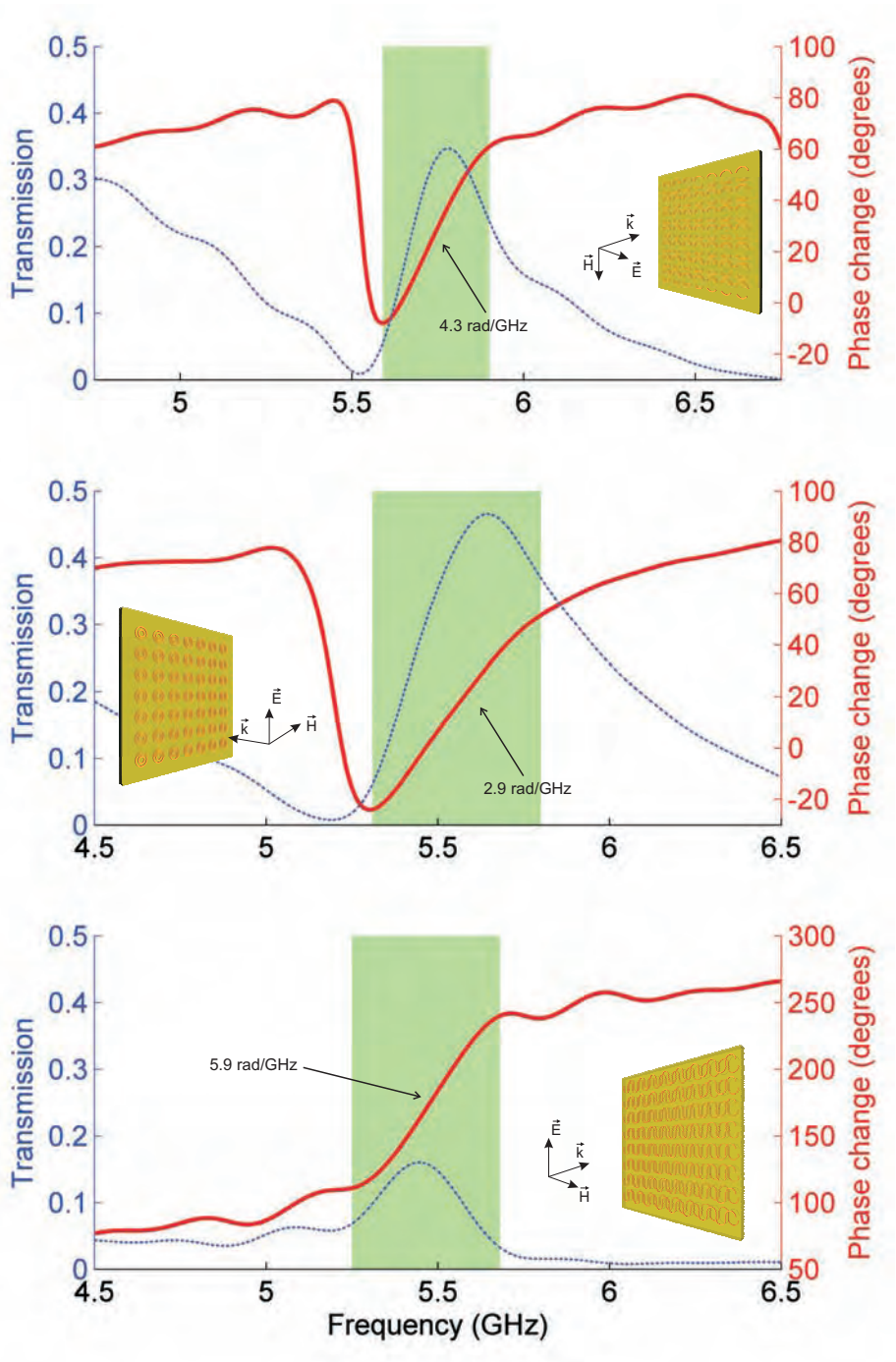

Fig. 5.3: Transmission (blue) and phase change (red) for (a) ASR metamaterial with different arc lengths, (b) concentric ring metamaterial and (c) the bi-layered fish-scale metamaterial with displaced top and bottom layers. The insets in the graphs show the propagation direction and the polarization of the incident wave, while the green panels mark the frequency regions of sharp normal dispersion.

Figure 5.3 presents transmission intensity and phase change for asymmetrically-split ring (ASR), concentric ring (CR) and bi-layered fish-scale arrays. Narrow trasmission resonances can

be observed in all cases, coresponding to the trapped-mode, antisymmetric current excitations. As expected by the Kramers-Kronig relations, these resonances are accompanied by sharp normal phase dispersion, which is approximately linear at the vicinity of the transmission peaks. Importantly, the sharpest phase dispersion is observed for the bi-layered fish-scale metamaterial with a slope of 5.9 rad/GHz as compared to 4.3 rad/GHz and 2.9 rad/GHz for the ASR and CR arrays, respectively. Furthermore, in contrast to the latter metamaterials, the phase change in the case of bi-layered fish-scale metamaterial is a monotonous function of frequency and hence group velocity dispersion is expected to be weaker.

The slow-light behaviour of the bi-layered fish-scale array is further illustrated in Fig. 5.4a, where the group delay is presented as a function of frequency. The group delay peaks at the trapped-mode resonance exceeding 1 ns, which is the maximum achievable delay in the structure regardless of the incident pulse width, while away from resonance, the group delay takes very small values around zero. On the other hand, the group velocity dispersion (see Fig 5.4b) vanishes at the transmission peak, but reaches very high positive and negative values at frequencies slightly above or below the "trapped-mode" resonance. Consequently, as the spectral width of an incident pulse increases the effects of the group velocity dispersion will become important leading to broadening of the pulse. Similar will be the effects of higher dispersion terms and of the dispersive nature of the transmission amplitude.

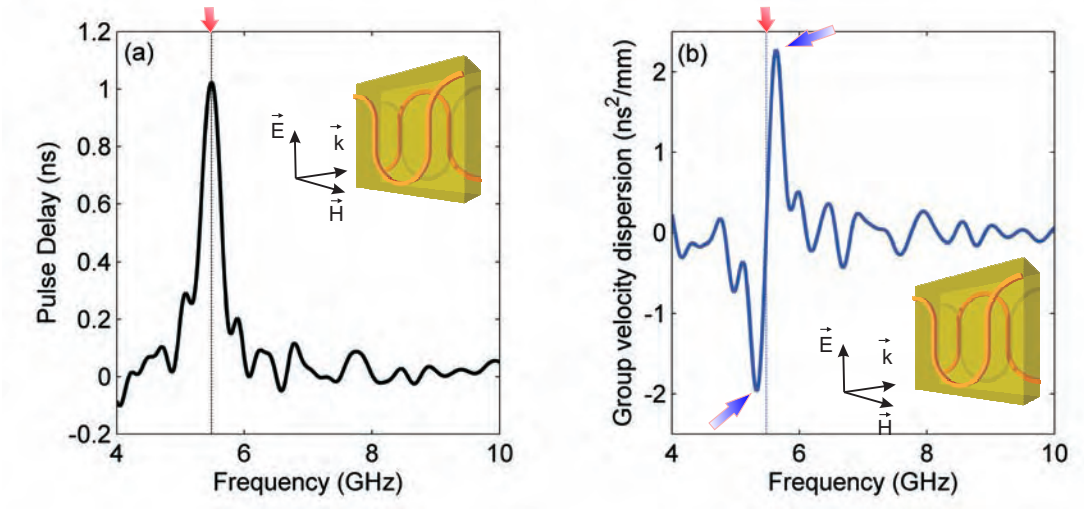

Fig. 5.4: Group delay (a) and group velocity dispersion (b) for the bi-layered fish-scale metamaterial (shown in the insets). The dashed lines and red arrows mark the frequency, where dispersion is at a maximum. The blue arrows in (b) mark maxima of the group velocity dispersion.

However, both the group velocity and the group velocity dispersion vary with frequency and therefore the delay and distortion that a pulse will experience will depend on its spectral width and, consequently, to its duration. This behaviour is illustrated in Fig. 5.5a, where the fractional delay and broadening (both normalized to the transmitted pulse duration) of the transmitted pulse are presented for pulses of different duration. More concisely, the bi-layered fish-scale metamaterial provides the longest fractional pulse delays for short, spectrally broad pulses, while broadening effects are relatively weak (less than 50% of the incident pulse duration). For example a 0.5 ns long pulse will broaden to 0.7 ns and will be delayed by more than 0.35 ns,

which corresponds to a fractional delay of about 50%. This counter-intuitive behaviour can be explained by considering the interplay of three different factors, i.e. (i) how much of the pulse spectral power lies within the area of constant normal dispersion, (ii) broadening due to distortion and (iii) the incident pulse duration. By decreasing the latter, the fractional delays become longer, but at the same time the spectrum of the pulse becomes broader and factors (i) and (ii) tend to decrease the fractional delay. However, outside the trapped-mode resonance the group velocity dispersion has very small values. Therefore, the pulse spectrum can become increasingly wide without leading to very strong distortion effects. As a result, the duration of the pulse will become smaller and the fractional delay will increase. This is not the case for the ASR metamaterial (see Fig. 5.5b), where the largest fractional pulse delay of 20% occurs for an optimum pulse duration of about 2.5 *ns*. In this case the delays are much smaller than in the bi-layered fish-scale, mainly due to the less steep slope of the phase curve at the trapped mode resonance but also due to the strong dispersion of both the group velocity and the transmitted intensity. These factors lead to broadening which limits the available fractional delays.

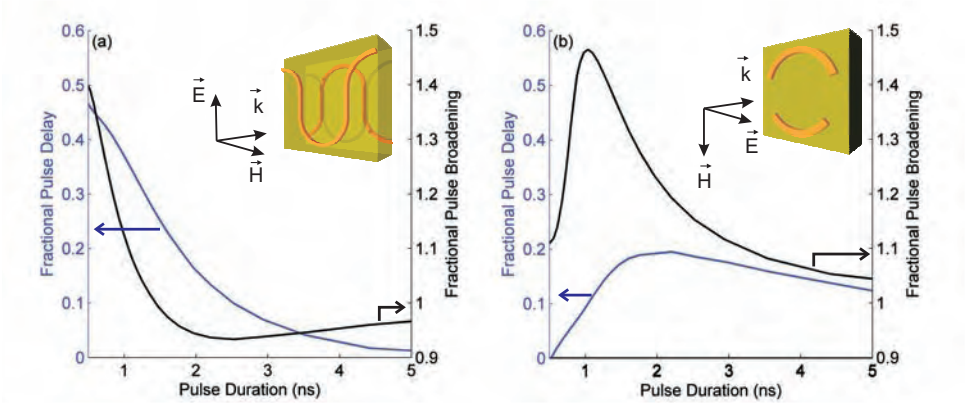

Fig. 5.5: Fractional pulse delay (blue) and fractional broadening (black), defined as the ratio of the delay and the transmitted pulse duration over the duration of the incident pulse, respectively, for the bi-layered fish-scale (a) and the ASR (b) metamaterial shown in the corresponding insets.

5.5 Metamaterial Analog of Electromagnetically Induced Transparency

The observed behaviour of the trapped-mode metamaterials can be considered as a classical analog of electromagnetically induced transparency, as the weak coupling of the counter-propagating currents to free space in the metamaterial is reminiscent of the weak probability for photon absorption in EIT observed in atomic systems. The main difference lies in the fact that, in the metamaterial case, the transparent state is a result of classical field interference, rather than quantum interference of atomic excitation pathways.

To draw the parallel further we will appeal to a circuit representation of the metamaterial [36]. The response of a single layer to an an incident electromagnetic field $\vec{E}_i$ can be described by the induced current $\vec{I}$. To simplify the following discussion, we will approximate the fish-scale metamaterial unit cell by a pair of parallel thin dipoles without a dielectric substrate. The induced current can be expressed in terms of an effective voltage $V = lE_i$, where l is the effective

length of the dipoles [37], by introducing the single layer impedance Z_o:

$$V = Z_o \cdot I,$$

or

$$lE_i = Z_o \cdot I, \tag{5.14}$$

The impedance $Z_o = Z_s + Z_m$ includes both the unit cell element self impedance Z_s and the mutual impedance between different elements on the same layer Z_m. Near the unit cell element resonance ω_o, the term Z_s varies rapidly with frequency and can be approximated by: $Z_o = R_s + jL_s(\omega^2 - \omega_o^2)/\omega \simeq (R_s + Z_m) + 2jL_s(\omega - \omega_o)$, where R_s and L_s can be considered as the resistance and the inductance of the circuit equivalent and are assumed constants defined by the geometry of the structure. Then, the reflectivity R of an array of dipole pairs will be given by [38]:

$$R \sim \frac{Re[Z_o]^2}{|Z_o|^2} \tag{5.15}$$

When a second layer is introduced at a distance d along the propagation direction of the incident wave, then interactions between the two layers have to be taken into account. More concisely, the current I_1 (I_2) on the first (second) layer induces a voltage on the second (first) layer and Eq. 5.14 becomes:

$$lE_i = Z_o \cdot I_1 + Z_c \cdot I_2 \tag{5.16}$$

$$lE_i e^{i\phi} = Z_o \cdot I_2 + Z_c \cdot I_1, \tag{5.17}$$

where $\phi = 2\pi/\lambda$ is the phase difference in the excitation of the two layers due to their physical separation and Z_c is the coupling impedance. The solution of the system of equations Eqs. 5.16 & 5.17 yields:

$$I_1 \sim \frac{Z_o - Z_c e^{i\phi}}{Z_o^2 - Z_c^2} E_i = e^{i\phi} \frac{Z_1}{D} E_i \tag{5.18}$$

$$I_2 \sim \frac{Z_o e^{i\phi} - Z_c}{Z_o^2 - Z_c^2} E_i = \frac{Z_2}{D} E_i, \tag{5.19}$$

where we have introduced for later convenience $Z_1 = Z_o e^{-i\phi} - Z_c$, $Z_2 = Z_o e^{i\phi} - Z_c$ and $D = Z_o^2 - Z_c^2$. Neglecting dissipation effects, the losses in the two-layer dipole array will be given by the reflectivity $|R|$ which will be proportional to:

$$|R| \sim |i_1 + i_2 e^{i\phi}| \sim \left| \frac{Z_1 + Z_2}{Z_1 Z_2 + Z_c(Z_1 + Z_2)} \right| \tag{5.20}$$

In Eq. 5.20 the current from the second layer is multiplied by a phase factor, in order to account for the retardation of the scattered fields due to the physical separation of the two layers.

A similar relation can be obtained for the case of ASRs and DRs, namely for two interlaced arrays on the same layer. In this case, each array is characterized by its impedance, $Z_o^{(1)}$ and $Z_o^{(2)}$ and the corresponding currents are given by:

$$I_1 \sim \frac{Z_o^{(1)} - Z_c}{Z_o^{(1)} Z_o^{(2)} - Z_c^2} E_i = \frac{Z_1}{D} E_i \tag{5.21}$$

$$I_1 \sim \frac{Z_o^{(2)} - Z_c}{Z_o^{(1)} Z_o^{(2)} - Z_c^2} E_i = \frac{Z_2}{D} E_i, \tag{5.22}$$

where $Z_1 = Z_o^{(1)} - Z_c$, $Z_2 = Z_o^{(2)} - Z_c$ and $D = Z_1 = Z_o^{(1)} Z_o^{(2)} - Z_c^2$. The reflectivity will be given again by Eq. 5.20.

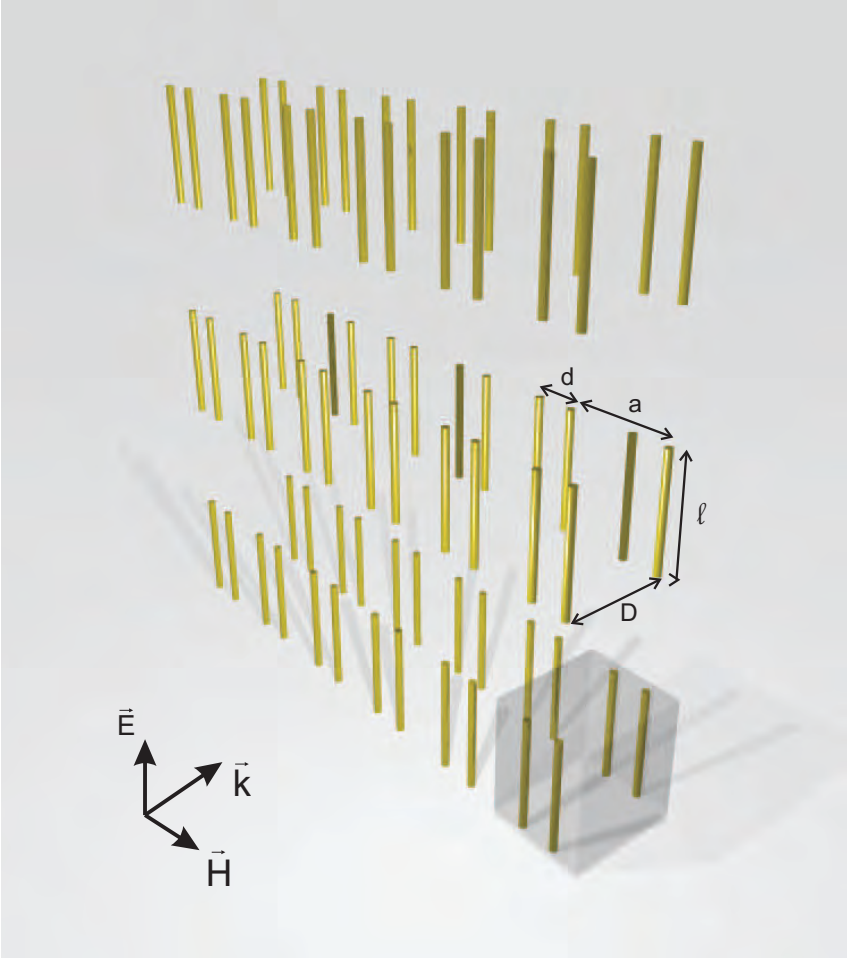

Fig. 5.6: (Approximation of the bilayered fish-scale metamaterial. The fish-scale unit cell is replaced with a pair of parallel half-wavelength dipoles. The polarization of incident wave is considered to be parallel to the dipole axis.

In both bi-layered and interlaced arrays, losses are eliminated when the sum $Z_1 + Z_2$ is at a minimum, which implies that the currents on each array oscillate with opposite phases according to Eqs. 5.21 and 5.22. This is in direct analogy with the detunings from the dressed states in EIT that contribute with opposite phases in the imaginary part of the linear susceptibility (see Eq. 5.13). Indeed, the imaginary part of impedances Z_1 and Z_2 can be understood as detunings from two resonant frequencies. The difference in the latter resonances is analogous to the AC

stark splitting in EIT as a result of the pump beam and is induced either by physical displacement of two identical layers, or simply by making one of the layers slightly different than the other one. On the other hand, reflection maxima will occur when Z_1 or Z_2 is at a minimum, namely when the induced current on one of the layers vanishes leading to strong scattering from the other layer.

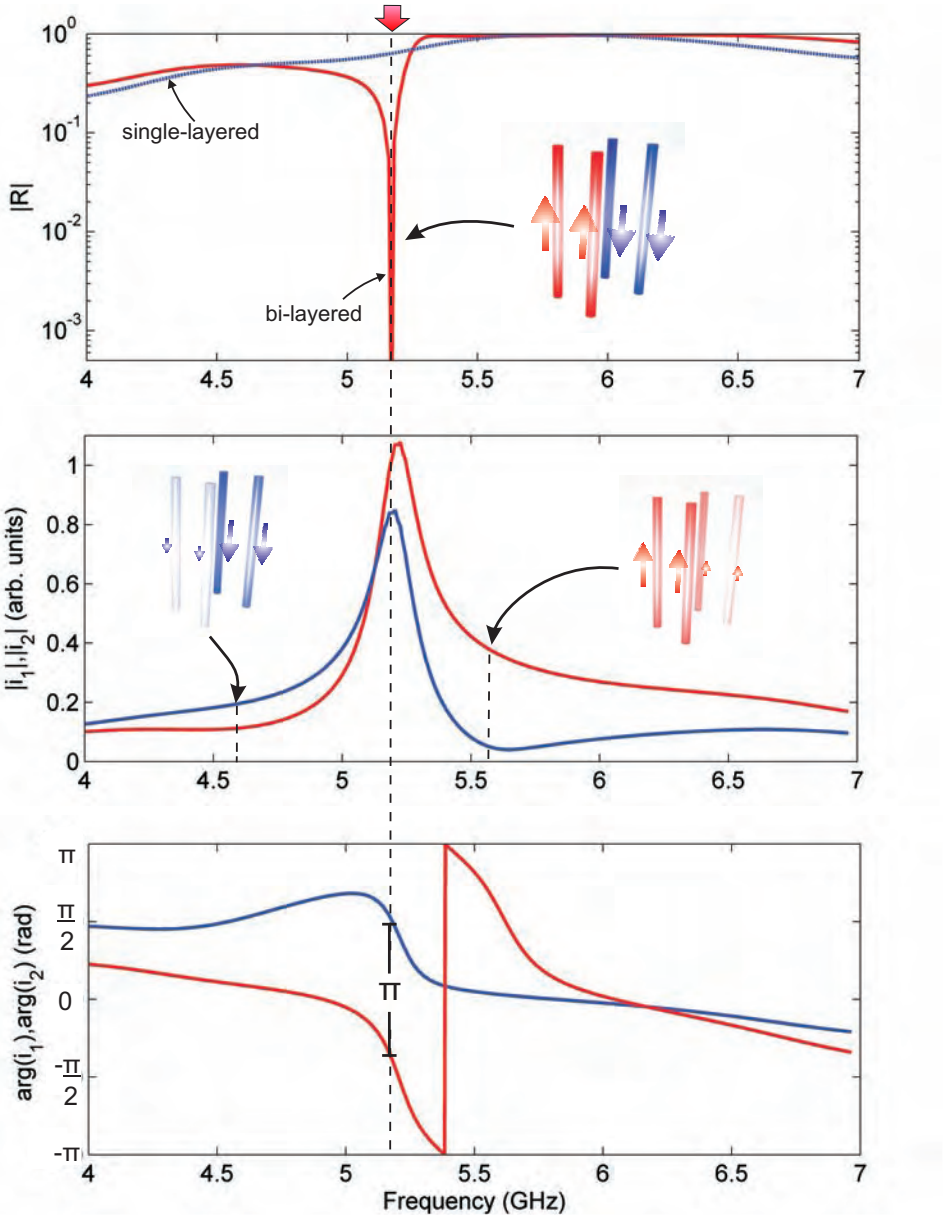

Fig. 5.7: (a) Representative reflectivity spectrum from Eq. 1 for single layer (dotted blue) and two-layer (solid red) structures approximated by $Z_o = 60 + 18 \cdot 10^{-9}(\omega - \omega_o)i$ and $Z_c = 55 - 60i$, where $\omega_o = 36.4 \cdot 10^9\ rad/s$. (b) Current strength on the front (red) and back (blue) layer. Dashed lines mark the positions of the reflection maxima. (c) Phase of the induced currents on the front (red) and back (blue) layer. At the trapped mode resonance an antisymmetric mode is established, with the currents on the two layers having a π phase difference.

This behaviour can be illustrated in the following example, where the bi-layered fish-scale is approximated by two arrays of thin, perfectly conducting, dipole pairs. The unit cell of each

layer had dimensions of $40x40\ mm$ and consisted of two parallel 27.3 mm long dipoles separated by 7.5 mm. The two layers were displaced by 4 mm with respect to each other along the direction of wave propagation. By limiting our analysis in a narrow frequency region around the half-wavelength resonance of the dipoles ($\sim 5.5\ GHz$), we can assume a sinusoidal current on each dipole. Then the impedance Z_o can be calculated [39], which yields approximately: $Z_o = 60 + 18 \cdot 10^{-9}(\omega - \omega_o)i$, where $\omega_o = 36.5 \cdot 10^{-9}\ rad/s$, while only the dispersion of the imaginary part of the single element impedance has been taken into account. In a similar way, the coupling impedance Z_c for a two-layer dipole-pair array can be estimated near the resonant frequency ω_o as $Z_c = 55 - 60i$. The reflection curve for this case is presented in Fig. 5.7a, where the reflectivity of a single layer array is also included for comparison. The most striking characteristic of the reflectivity curve is the EIT signature of a narrow minimum within the broad single-layer reflection peak. The currents on each layer and their relative phase difference is also presented in Figs 5.7b and 5.7c, respectively. In the far-field zone, the waves emitted by these resonant, anti-symmetric currents interfere destructively due to the π phase difference, hence dramatically reducing scattering losses. As a result the currents induced in the metal stripes in each layer become exceptionally high near the trapped mode resonance (see Fig. 5.7b). Although this estimation is prone to significant approximation and becomes increasingly unrealistic away from the half-wavelength dipole resonance, nevertheless it proves that the circuit representation is adequate to reproduce at least qualitatively the similarity of the trapped-mode metamaterials with EIT systems.

5.6 Bandwidth Enhancement In Cascaded Metamaterials

The bandwidth of the normal dispersion region can be significantly increased with a small penalty in the maximum achievable delay and an actual increase in the maximum transmission within this frequency region, by successively stacking fish-scale metamaterial slabs. Indeed, the fish-scale design can be cascaded in such a way, that each slab is inverted with respect to the adjacent ones (see left panels in Fig. 4.8), while the distance between successive fish-scale patterns is defined by the thickness of the dielectric substrates (1.5 mm). The experimental results for three and four fish-scale layers are shown in Figs. 4.8a and 4.8b, respectively.

In both cases, stacking of multiple slabs results in an increase of maximum transmitted intensity and width of the frequency region, where normal dispersion occurs. In particular, with each additional layer, a new transmission peak appears shifted at lower frequencies with respect to the bi-layered fish-scale case. These new peaks can be attributed to the different modes that become accessible with increasing number of layers due to "hyridization" of the modes that each pair of adjacent of fish-scale layers supports [40]. At the same time, the sharp normal phase dispersion extends over a wide frequency band exceeding 1.5 GHz and 2.5 GHz for three and four layers, respectively. However, the steepness of the phase slope weakly varies between resonances, which introduces distortion (broadening) and limits the attainable delays.

5.7 An optical delay line

In order to demonstrate the scalability of the presented approach and its applicability to the actual technological challenges, we simulate a trapped-mode metamaterial operating at telecom-

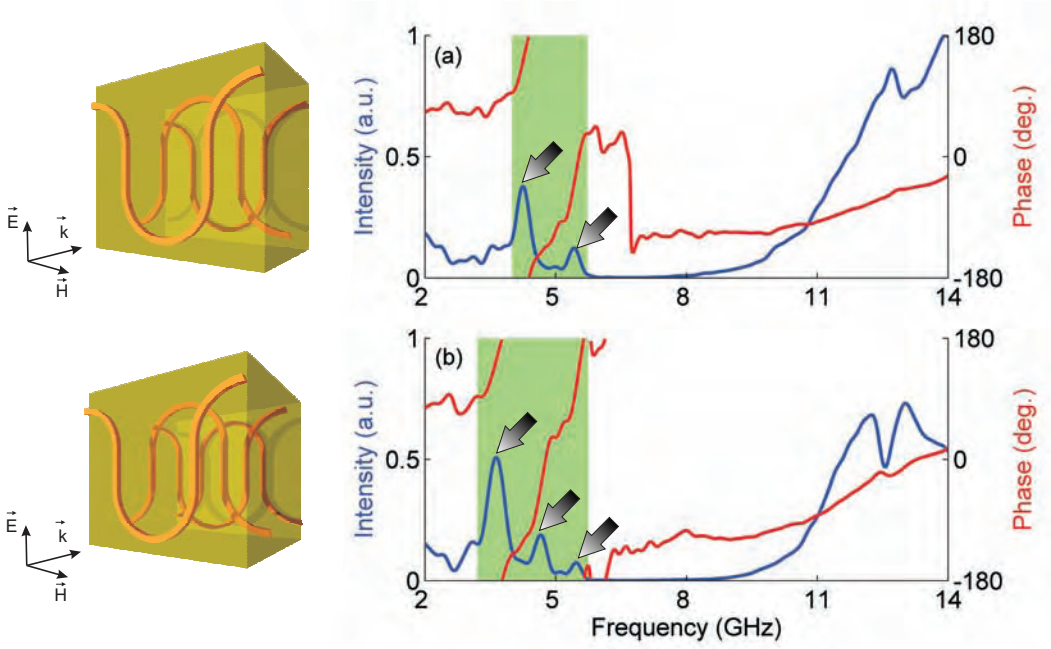

Fig. 5.8: Experimentally measured transmission amplitude (blue) and phase change (red) for three (a) and four (b) fish-scale layers. The arrows mark the positions of individual resonances, while the area of normal dispersion is highlighted (green).

wavelengths, i.e. $\sim 1.5\mu m$. Since bi-layered structures are not easily manufactured at nanoscales, we consider a single-layer metamaterial based on asymmetrically-split rings (ASRs). The modeled structure has a $210x210$ nm unit cell and is supported by a 200 nm thick silicon substrate with permittivity $\epsilon = 12$. The rings are considered to be made of silver, for which the permittivity is given by a Drude model fit to experimental data. Transmission and phase for the optical ASR array is shown in Fig. 4.9a, which shows the characteristic trapped-mode behaviour. Due to the large asymmetry, the transmission window extends over a wide region of about 40 THz, while at the same time sharp normal dispersion occurs. The corresponding fractional delay for different durations of the incident pulse is presented in Fig. 4.9b. The maximum achievable delay occurs for about a 30 fs incident pulse which is delayed for about 20%. This delay is small in view of potential applications, however the bandwidth at which it occurs is quite broad. At the same time the broadening that the pulse experiences is weak, remaining under 30%. The delay-bandwidth product of the structure is about 0.2, which is of the same order of magnitude with that of a typical resonator waveguide. However, it has been suggested that a more appropriate figure of merit should take into account the length of the structure [41]. Therefore, we will consider as a figure of merit the delay-bandwidth product divided by the ratio of the thickness of the structure along the propagation direction over wavelength. For the ASR presented here this FOM is about 1.3, which is at least comparable if not higher than a large number of other approaches [41].

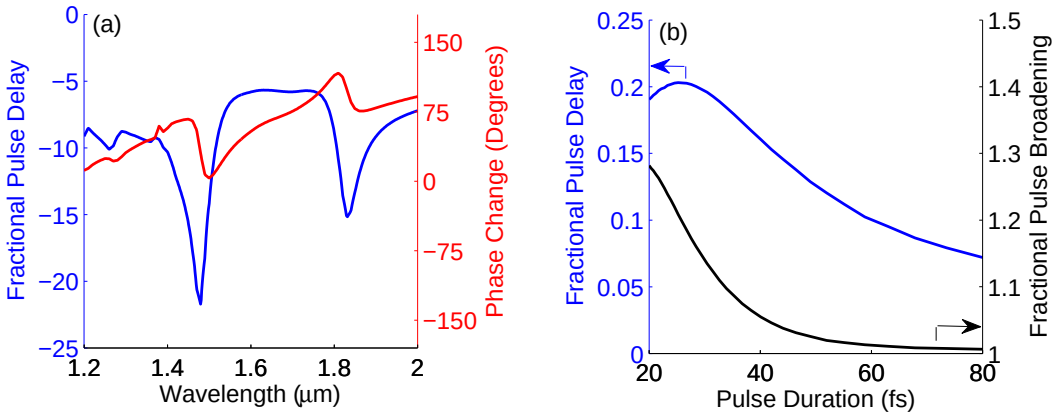

Fig. 5.9: (a) Transmission and phase change spectrum for an infrared ASR array. A steep phase dispersion can be distinguished at the trapped mode resonance, where with losses of about $-6\ dB$. (b) Corresponding fractional pulse delay and broadening.

5.8 Conclusions

In conclusion, a new approach to slow light has been presented, one that, in contrast to previous schemes does not require the medium to extend along the propagation direction. This can lead to an extremely small footprint, and also provides the opportunity to structure already present interfaces. It is also shown that the trapped-mode metatamaterial behaviour constitutes a classical analog of EIT, where quantum probability amplitudes are replaced by fields radiated from resonant current configurations. Open questions that need to be addressed include the possibility for tunability of the pulse delay and the compensation of losses in the optical part of the spectrum

BIBLIOGRAPHY

[1] L. Brillouin, *Wave Propagation and Group Velocity* (Academic Press Inc., New York, 1960).

[2] T. Baba. Slow light in photonic crystals. *Nature Photonics* **2**, 465 (2008).

[3] T. F. Krauss. Slow light in photonic crystal waveguides. *Journal of Physics D: Applied Physics* **40**, 2666 (2007).

[4] R. S. Tucker, P. C. Ku, and C. J. Chang-Hasnain. Slow light optical buffers: Capabilities and fundamental limitations. *Journal of Lightwave Technology* **23**, 4046 (2005).

[5] D. J. Bradley, G. M. Gale, and P. D. Smith. Self-induced transparency and dispersion delays in potassium vapour. *Nature* **225**, 719 (1970).

[6] D. Grischkowsky. Adiabatic following and slow optical pulse propagation in rubidium vapor. *Physical Review A* **7**, 2096 (1973).

[7] L. V. Hau, S. E. Harris, Z. Dutton, and C. H. Behroozi, Nature **397**, 594 (1999).

[8] S. E. Harris, J. E. Field, and A. Imamoglu. Nonlinear optical processes using electromagnetically induced transparency. *Physical Review Letters* **64**, 1107 (1990).

[9] A. V. Turukhin, V. S. Sudarshanam, M. S. Shahriar, J. A. Musser, B. S. Ham, and P. R. Hemmer. Observation of ultraslow and stored pulses in a solid. *Physical Review Letters* **88**, 023602 (2001).

[10] M. S. Bigelow, N. N. Lepeshkin, and R. W. Boyd. Superluminal and slow light propaggation in a room temperature solid. *Science* **301**, 200 (2003).

[11] P. C. Ku, F. Sedgwick, C. J. Chang-Hasnain, P. Palinginis, T. Li, H. Wang, S. W. Chang, and S. L. Chuang. Slow light in semiconductor quantum wells. *Optics Letters* **29**, 2291 (2004).

[12] S. E. Harris. Electromagnetically induced transparency in an ideal plasma. *Physical Review Letters* **77**, 5357 (1996).

[13] D. F. Gordon, W. B. Mori, and C. Joshi. On the possibility of electromagnetically induced transparency in plasma. I. Infinite plasma. *Physics of Plasmas* **7**, 3145 (2000).

[14] D. F. Gordon, W. B. Mori, and C. Joshi. On the possibility of electromagnetically induced transparency in plasma. II. Bounded plasma. *Physics of Plasmas* **7**, 3156 (2000).

[15] C. L. G. Alzar, M. A. G. Martinez, and P. Nussenzveig, Am. J. Phys. **70**, 37 (2002).

[16] L. Maleki, A. B. Matsko, A. A. Savchenkov, and V. S. Ilchencko. Tunable delay line with interacting whispering-gallery-mode resonators. *Optics Letters* **29**, 626 (2004).

[17] A. B. Matsko, A. A. Savchenkov, D. Strekalov, V. S. Ilchenko, and L. Maleki. Interference effects in lossy resonator chains. *Journal of Modern Optics* **10**, 2515 (2004).

[18] D. D. Smith, H. Chang, K. A. Fuller, A. T. Rosenberger, and R. W. Boyd. Coupled-resonator-induced transparency. *Physical Review A* **69**, 063804 (2004).

[19] Q. Xu, S. Sandhu, M. L. Povinelli, J. Shakya, S. Fan, and M. Lipson. Experimental realization of an on-chip all-optical analogue to electromagnetically induced transparency. *Physical Review Letters* **96**, 123901 (2006).

[20] Q. Xu, J. Shakya, and M. Lipson. Direct measurement of tunable optical delays on chip analogue to electromagnetically induced transparency. *Optics Express* **14**, 6463 (2006).

[21] A. Naweed, G. Farca, S. I. Shopova, and A. T. Rosenberger. Induced transparency and absorption in coupled whispering-gallery microresonators. *Physical Review A* **71**, 043804 (2005).

[22] K. Totsuka, N. Kobayashi, and M. Tomita. Slow light in coupled-resonator-induced transparency. *Physical Review Letters* **98**, 213904 (2007).

[23] M. Scalora, R. J. Flynn, S. B. Reinhardt, R. L. Fork, M. J. Bloemer, M. D. Tocci, C. M. Bowden, H. S. Ledbetter, J. M. Bendickson, J. P. Dowling, and R. P. Leavitt. Ultrashort pulse propagation at the photonic band edge: Large tunable group delay with minimal distortion and loss. *Physical Review E* **54**, R1078 (1996).

[24] M. Notomi, K. Yamada, A. Shinya, J. Takahashi, C. Takahashi, and I. Yokohama. Extremely large group-velocity dispersion of line-defect waveguides in photonic crystal slabs. *Physical Review Letters* **87**, 253902 (2001).

[25] Y. A. Vlasov, M. O'Boyle, H. F. Hamann, and S. J. McNab. Active control of slow light on a chip with photonic crystal waveguides. *Nature* **438**, 65 (2005).

[26] M. F. Yanik, W. Suh, Z. Wang, and S. Fan. Stopping light in a waveguide with an all-optial analog of electromagnetically induced transparency. *Phys. Rev. Lett.* **93**, 233903 (2004).

[27] Q. Xu, P. Dong, and M. Lipson. Breaking the delay-bandwidth limit in a photonic structure. *Nature Physics* **3**, 406 (2007).

[28] Y. Okawachi, M. S. Bigelow, J. E. Sharping, Z. M. Zhu, A. Schweinsberg, D. J. Gauthier, R. W. Boyd, and A. L. Gaeta. Tunable all-optical delays via Brillouin slow light in an optical fiber. *Physical Review Letters* **94**, 153902 (2005).

[29] K. Y. Song, M. G. Herrez, and L. Thvenaz. Observation of pulse delaying and advancement in optical fibers using stimulated Brillouin scattering. *Optics Express* **13**, 82 (2005).

[30] K. L. Tsakmakidis, O. Hess, and A. D. Boardman. Trapped rainbow storage of light in metamaterials. *Nature* **450**, 397 (2007).

[31] L. Thevenaz. Slow and fast light in optical fibres. *Nature Photonics* **2**, 474 (2008).

[32] C. G. B. Garrett and D. E. McCumber, Phys. Rev. A **1**, 305 (1970).

[33] L. Casperson and A. Yariv, Phys. Rev. Lett. **26**, 293 (1971).

[34] S. Chu and S. Wong, Phys. Rev. Lett. **48**, 738 (1982).

[35] M. Fleischhauer, A. Imamoglu, and J. P. Marangos. Electromagnetically induced transparency: Optics in coherent media. *Rev. Mod. Phys.* **77**, 633 (2005).

[36] B. A. Munk and R. J. Luebbers, IEEE Trans. Antennas Propag. **AP-22**, 776 (1974).

[37] G. Sinclair. The transmission and reception of elliptically polarized waves. *Prceedings of the I.R.E.* **38**, 148 (1950).

[38] B. Munk, R. Kouyoumjian, and L. Jr. Peters. Reflection properties of periodic surfaces of loaded dipoles. *IEEE Transactions on Antennas and Propagation* **19**, 612 (1971).

[39] C. T. Tai. Coupled antennas. *Proceedings of the I.R.E.* **36**, 487 (1948).

[40] N. Liu, L. Fu, S. Kaiser, H. Schweizer, and H. Giessen, Plasmonic building block for magnetic molecules in three-dimensional optical metamaterials. *Advanced Materials* **20**, 3859 (2008).

[41] J. B. Khurgin, J. Opt. Soc. Am. B **22**, 1062 (2005).

6. COLLECTIVE EFFECTS IN PASSIVE AND ACTIVE METAMATERIALS

6.1 Introduction

The strongly dispersive nature of the metamaterials response stems from the resonances of its individual constituents (meta-molecules). As a result the electromagnetic behaviour of individual meta-molecules and metamaterial arrays are usually very similar and any differences can be attributed to the moderate interactions between adjacent elements [1, 2]. However, it has been shown that inductive coupling between metamaterial resonators can lead to collective behaviour and reveal new effects [3, 4, 5]. In particular, periodic arrangements of split-ring resonators in one, two and three dimensions can support a new kind of waves termed magneto-inductive waves [4, 6]. Such waves arise from the voltage induced in each split-ring due to the time-varying magnetic fields associated with the currents on the other resonators in the array. Magneto-inductive waves present intriguing properties: they exhibit strong dispersion, they can only propagate only within specific pass-bands, they can be forward or backward waves [4, 6, 7, 8, 10]. These properties are desirable in various applications and to this end numerous devices based on magneto-inductive waves have been suggested, including waveguides, junctions, couplers and transducers [4, 9, 10, 11]. In addition, it was suggested that magneto-inductive waves can be employed to launch electromagnetic waves [12], while applications in sub-wavelength imaging [13] and nuclear magnetic resonance imaging [14] were also considered.

Collective effects in metamaterials become especially important, when the effects of disorder on the metamaterial response are considered. Indeed, weakly interacting meta-molecules should not be greatly affected by disorder, while drammatic changes are expected in strongly-interacting systems. Studies of disorder in metamaterials have focused mainly to periodic arrays of resonators whose resonant frequencies follow a random distribution. In particular, it was predicted that in the case of magnetic metamaterials, introducing disorder in the form of weak fluctuations in the parameters of the unit cell resonators or as impurities can lead to significant changes in the effective permeability, which typically takes lower values with increasing fluctuation intensity or impurity concentration [15, 16]. The strong dependence of metamaterial parameters in the microscopic disorder was attributed to the scattering of magnetoinductive waves at the resonators with different parameters and at the impurities, hence introducing an additional loss mechanism [16]. This behaviour was verified experimentally in arrays of microwave split-ring resonators, whose geometric parameters varied according to a uniform distribution [17]. In contrast to the effects of random fluctuations in the resonator geometry, studies of the effects of different disorder types in metamaterials are not well understood. Preliminary theoretical investigations of one-dimensional nanoparticle chains that support guided waves have shown that increase of positional disorder leads to increased damping for such waves [18]. Also, non-systematic studies of magnetic metamaterials consisting of split-rings have shown qualitatively that the response

of split-ring arrays is affected by random displacements of the individual unit cells, as well as by displacements of whole two-dimensional layers [2]; however, in all cases of positional disorder the metamaterial resonant response persisted. Finally, similar effects where observed for the negative refractive index of a microwave metamaterial with a dendritic unit cell [19].

Here, two extreme cases of metamaterials are introduced: coherent metamaterials, where the resonant response is a property of the metamaterial array and is not found in a single meta-molecule, and incoherent metamaterials, where the response of individual arrays and resonator arrays are almost identical. We attribute this behaviour to the presence or absence, respectively, of magnetization which is not coupled to the magnetic field of the incident wave due to its orientation: normal to the array plane and parallel to the incident wave propagation direction. This fundamental difference leads to dramatic behaviour in presence of disorder: coherent metamaterials depend critically in the periodic nature of the array, while the antipode class of incoherent metamaterials appears almost independent of disorder. The collective nature of the coherent metamaterial response allows for a strong feedback mechanism which can be employed in active devices. Such a device, termed the lasing spaser, is suggested here and its potential for amplification and light-emission is demonstrated numerically both in the optical and mid-infrared part of the electromagnetic spectrum.

6.2 Single element and collective resonances in trapped-mode metamaterials

The observed trapped resonances in the asymmetrically-split ring (ASR) and the concentric ring (CR) metamaterials, although both manifest as sharp minima in the reflection spectrum, are of different origin, the former depending essentially on a collective (coherent) effect, while the latter is predominantly a property of a single meta-molecule. To illustrate this fact, finite element numerical simulations were performed on self-standing, infinitely thin, perfectly conducting structures and the scattering properties under plane wave illumination of both an infinite metamaterial array and an isolated single meta-molecule were simulated. In the first case, the reflection spectrum of the infinite periodic array was calculated and was compared to the back scattered electromagnetic field spectrum of a single metamaterial resonator. This comparison is justified by the fact that in both cases the spectrum is estimated following a similar procedure: the electromagnetic fields are estimated on a surface in the presence of the metamaterial structure (be it a single resonator or an array) and are subtracted from the fields estimated in the absence of the resonators.

The results for asymmetrically-split ring resonators are presented in Fig. 6.2. The inner and outer radius of the simulated ASRs was 5.6 mm and 6.4 mm, respectively, while the arcs corresponded to 160^0 and 140^0 angles. In the case of the array, a square unit cell of 1.5 mm side was used. In both cases, the incident plane wave was polarized along the x-axis of Fig. 6.2a. A single ASR presents a rather broad maximum in its scattering spectrum at 9.25 GHz with a width of 228 MHz (Fig. 6.2b), in contrast to the behaviour of the ASR array that exhibits a narrow reflection minimum at 8.85 GHz with a width of roughly 733 MHz (see Fig. 6.2g). The origin of this qualitative difference in scattering properties becomes evident, when one has closer look at the multipole moments corresponding to the current configuration on the split ring arcs. In the case of a single split ring, the induced electric dipole moments on the arcs oscillate in-phase (Fig. 6.2c) leading to a peak in the total electric dipole moment (Fig. 6.2d)

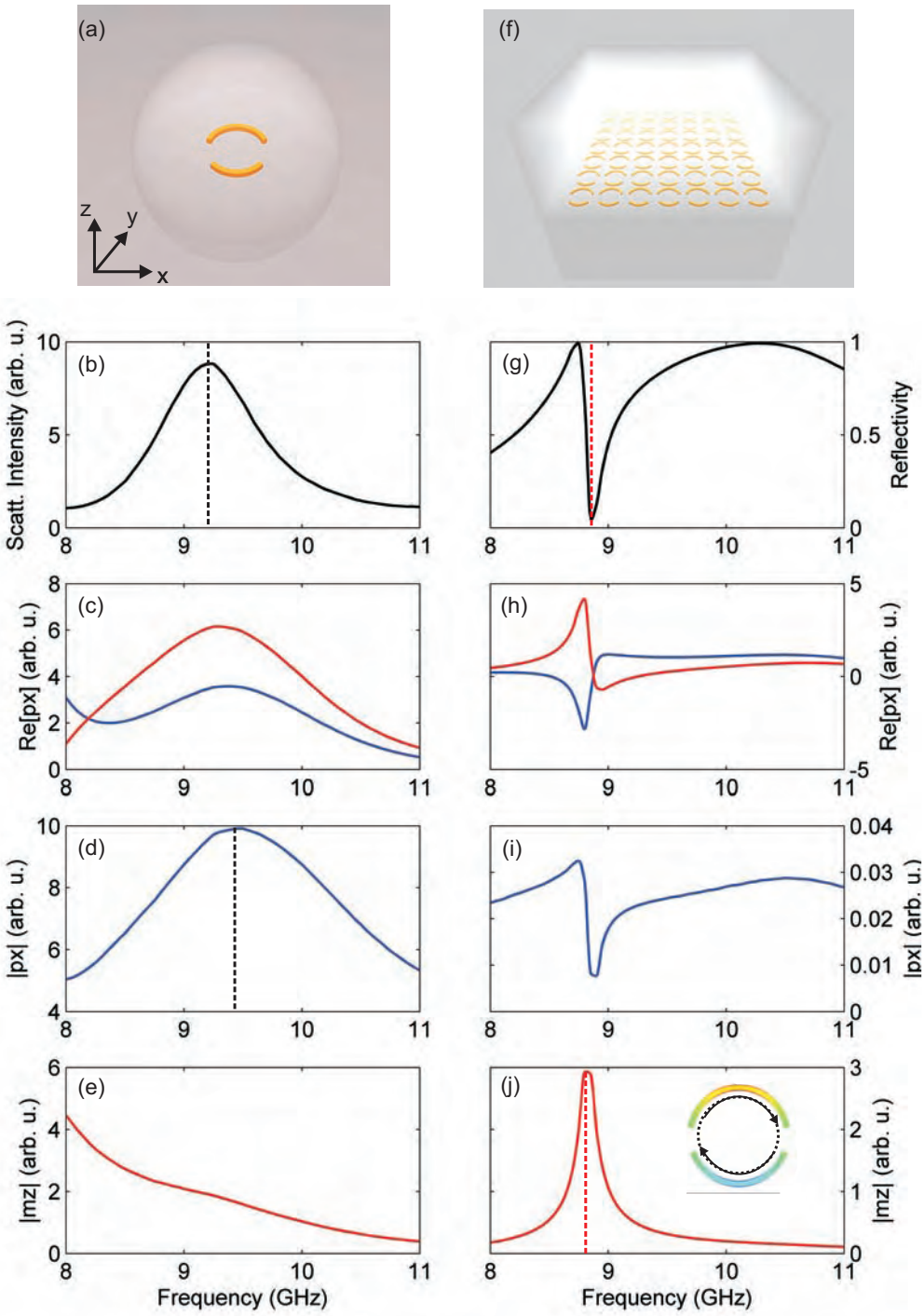

Fig. 6.1: Scattering properties of asymmetrically-split rings. (a-e) isolated split ring: sketch of single split ring (a), scattering spectrum under plane wave illumination (b), x-component of the electric dipole moment for each arc (c) and for both arcs combined (d), and z-componenet of the magnetic dipole moment (e). (f-j) split ring array: sketch of metamaterial array (f), reflection spectrum (g), x-component of the electric dipole moment for each arc (h) and for both arcs combined (i), and z-component of the magnetic dipole moment (j).

which is responsible for the scattering maximum. On the contrary, in the case of the ASR

array, an anti-symmetric current configuration is supported, where the induced electric dipole moments oscillate in anti-phase (Fig. 6.2h) resulting in a minimum of the total electric dipole moment of the unit cell (Fig. 6.2i). This anti-phase oscillation corresponds to a loop current and a resonant peak in the magnetic dipole moment spectrum (Fig. 6.2j). Since no counter propagating currents are supported by the single ASR, there is no resonance in the magnetic dipole moment spectrum. Indeed, while a single magnetic dipole can radiate strongly in a wide range of angles, in an infinite array of magnetic dipoles oriented perpendicular to the plane of the array (z-axis of Fig. 6.2a), radiation is only allowed in the plane of the array and is suppressed in all other angles. Hence, in an ASR array energy is accumulated in the magnetic dipoles that are uncoupled to free-space, while scattering losses occur only due to the weak electric dipole. On the contrary, the magnetic dipole moment of a single ASR scatters strongly leading to high radiation losses and a suppression of the trapped-mode resonance.

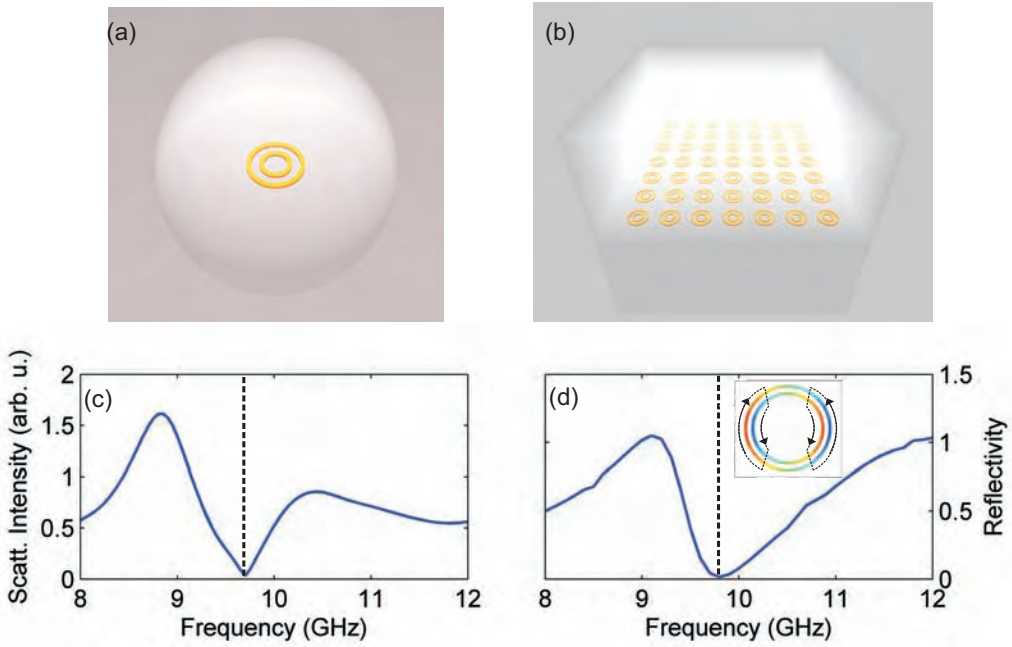

Fig. 6.2: Scattering properties of concentric ring pairs: sketch of isolated meta-molecule (a) and the corresponding scattering spectrum under plane wave illumination (b); sketch of the metamaterial array (c) and the corresponding reflection spectrum (d). The dashed lines mark the position of the scattering/reflection minima associated with the trapped-mode resonance. Inset: Simulated current configuration at the trapped-mode resonance for a CR array.

The situation is dramatically different when the scattering properties of a single CR and a CR array are compared (Fig. 6.2). Indeed, scattering from a single CR resonator (Fig. 6.2b) and reflection from an infinite periodic array of such resonators (Fig. 6.2d) are very similar: the scattering spectrum of a single CR presents at 1.219 GHz wide minimum at 9.7 GHz, while reflection from a CR array exhibits a 1.005 GHz wide dip at 9.8 GHz, both manifestations of the trapped-mode resonance. The reason why concentric rings behave differently from asymmetrically-split rings is the absence of induced magnetic dipole moments. Indeed, from the simulated current configuration (inset to Fig. 6.2d), it is evident that the CR resonator can

be decomposed in two parts that support loop-like currents that flow along opposite directions. Hence the corresponding magnetic dipole moments have opposite phases and the total magnetic dipole reponse vanishes. Since the trapped-mode resonance in the CR case does not require a strong magnetic dipole, then a single CR does not experience the strong magnetic dipole scattering losses and, consequently, can support the anti-symmetric current configuration necessary for the trapped-mode resonance to manifest.

6.3 Effect of positional disorder in trapped-mode metamaterials

The demonstrated collective or individual character of the trapped-mode metamaterials' response leads to distinct behaviour in the presence of the disorder. In a first instance, the behaviour of the trapped-mode resonance upon disordering the regular lattice is investigated.

Positional disorder was introduced in the metamaterial array by randomly displacing each meta-molecule from its original position in the periodic array according to the following procedure: the center of each unit cell is displaced to a randonmly chosen point within a square of side α centered at the original position of the meta-molecule's centre. The degree of disorder is quantified by the dimensionless parameter, D, defined as the ratio of α over the unit cell side. Disordered arrays consisting of ASRs and CRs were manufactured for different degrees of disorder. In particular, for each value of the disorder parameter, D, five different ASR arrays and a single CR array were studied [1]. The geometry of both metamaterial arrays is presented in Fig. 6.3. The inner and outer radius of the ASRs was 2.8 mm and 3.2 mm, respectively, while the ASR arcs corresponded to 160^0 and 140^0 angles. The inner and outer radii of the CRs was 2.15 mm & 2.35 mm for the smaller ring and 2.625 mm & 2.825 mm for the larger ring, respectively. In both cases, the unit cell's dimensions were $7.5x7.5$ mm.

The response of the disordered arrays under plane wave illumination was studied and the corresponding results are shown in Figs. 6.4 & 6.5. In all cases the incident wave was polarized with its electric field parallel to the split ring arcs. Panels (a)-(g) of Fig. 6.4 demonstrate the strong dependence of the ASR metamaterial to positional disorder. Indeed, the trapped-mode resonance degrades considerably even for weak disorder ($0.22 < D < 0.32$) and becomes indiscernible for moderate disorder ($D = 0.55$). On the other hand, in the case of CR metamaterial arrays, the trapped mode persists even for strong disorder (see panels (f)-(j) of Fig. 6.5) and any marked changes in the resonance are observed at high values of D ($D > 0.63$). Strikingly, the reflection dip can still be observed at the the highest value of disorder ($D = 1$).

The dramatic difference in the behaviour of the two metamaterials becomes apparent, when the dependence of their resonance linewidth on the disorder is considered (see Fig. 6.6). The procedure by which the linewidith is estimated is presented in Fig. 6.4a: a line is considered to pass through the reflection maxima located on the left- and right-hand side of the reflection dip; then the depth of the reflection dip is estimated considering as maximum the level of the fitted line and the full width at the level where reflection reduces to 50% of the maximum. Here, the inverse linewidth, τ is employed as a measure of the resonance lifetime, which represents the coupling of the current configuration to free-space radiation and is directly related to the average strength of the anti-symmetric component of the current mode induced in the meta-molecules by

[1] Preliminary experiments indicated very weak dependence of the concentric ring metamaterials to positional disorder, allowing thus to limit the number of needed samples to one per degree of disorder.

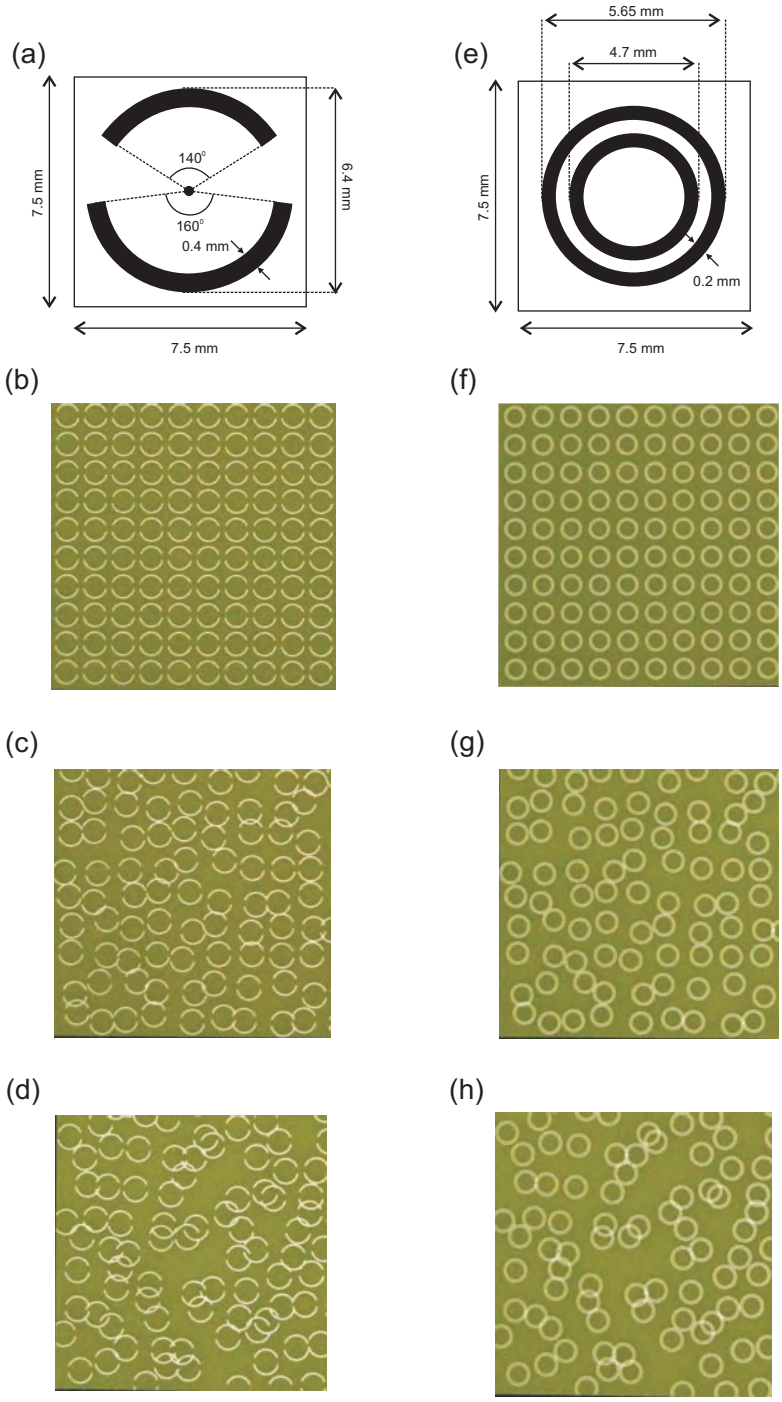

Fig. 6.3: (a) Geometry of the ASR metamaterial unit cell. (b)-(e) Fragments of ASR metamaterial arrays for $D = 0$ (b), $D = 0.5$ (c), and $D = 1$ (d). (e) Geometry of the CR metamaterial unit cell. (f)-(h) Fragments of ASR metamaterial arrays for $D = 0$ (f), $D = 0.5$ (g), and $D = 1$ (h).

the incident electromagnetic wave. The disordered ASR metamaterial arrays exhibit a fast decay of the resonance lifetime with increasing disorder and already for moderate disorder ($D = 0.63$) it becomes impossible to distinguish the resonance in the reflection spectrum. On the contrary, the resonant behaviour of concentric ring arrays appear almost independent of disorder even for

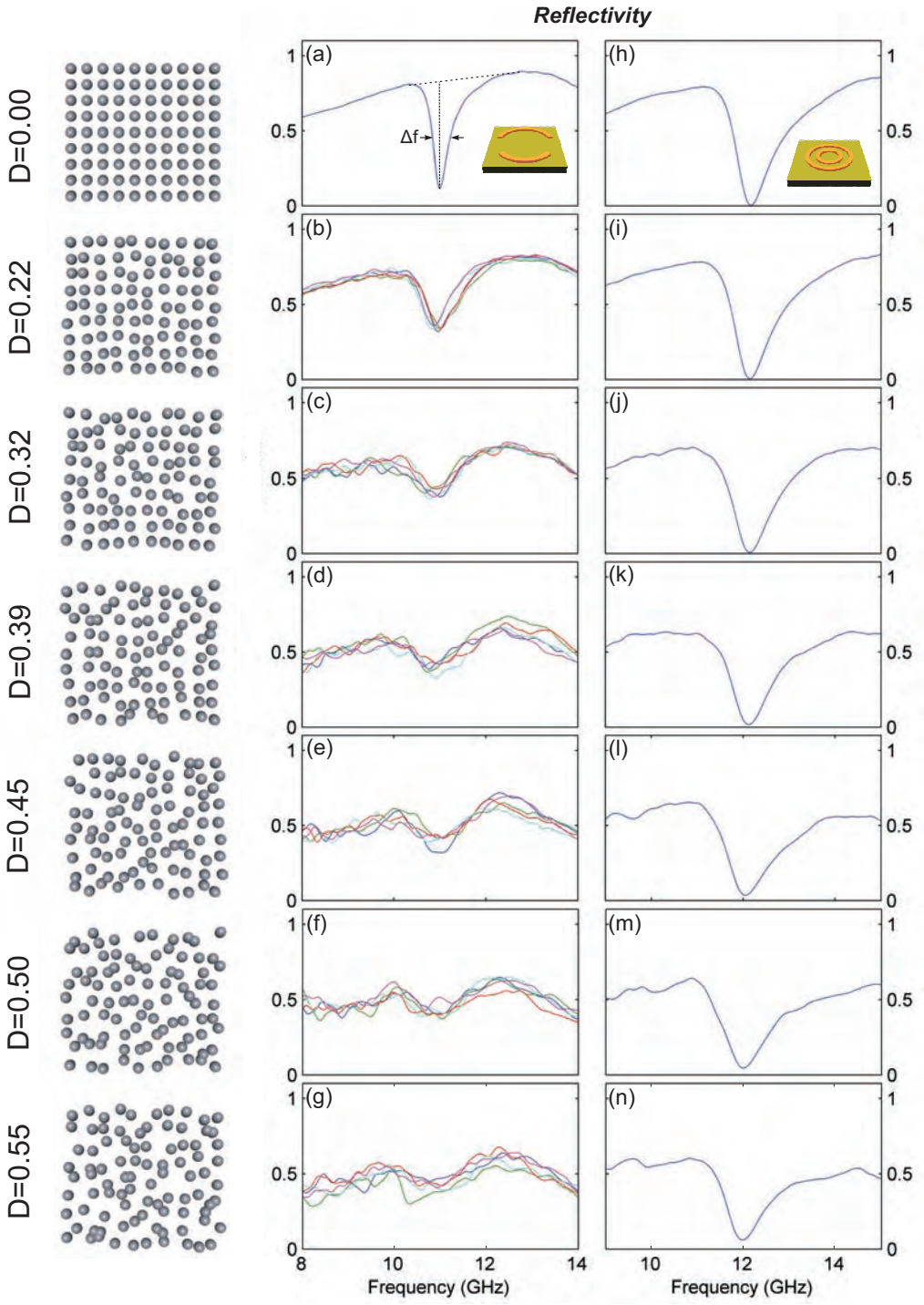

Fig. 6.4: Reflection of disordered asymmetrically-split ring (a-g) and concentric ring (h-n) metamaterial arrays for different values ($0-0.55$) of the disorder parameter, D. In the case of asymmetrically-split rings, five different realizations corresponded to to each value of D. The left column illustrates the degree of disorder for each value of D.

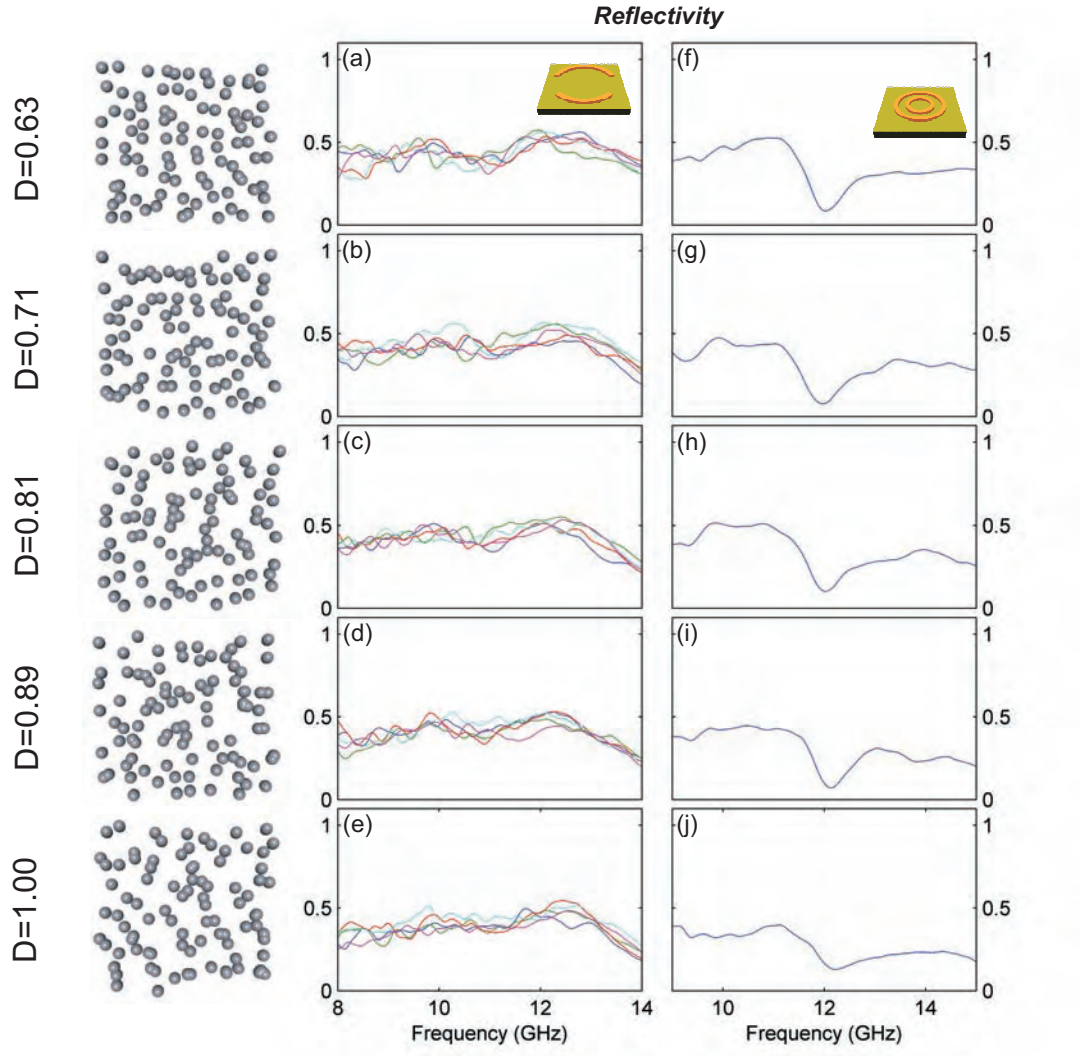

Fig. 6.5: Reflection of disordered asymmetrically-split ring (a-e) and concentric ring (f-j) metamaterial arrays for different values $(0.63-1)$ of the disorder parameter, D. In the case of asymmetrically-split rings, five different realizations corresponded to to each value of D. The left column illustrates the degree of disorder for each value of D.

values of disorder parameter as high as $D = 0.81$.

The dependence or independence of the metamaterials to positional disorder can be attributed to the different origin of the trapped-mode resonance. Indeed, as shown in section 6.2, the main difference between the response of the ASR and the CR metamaterials lies in the presence of a strong induced magnetic dipole moments in the former and the absence thereof in the latter. In particular, at resonance conditions, concentric rings support a weak electric dipole moment (by design), while the magnetic dipole moment vanishes. Hence, any interactions between adjacent elements will be mediated by the weak electric dipole and multipoles of electric quadrupole order or higher resulting in short-range interactions. As a result mutual interactions between the meta-molecules (both of electric or magnetic dipole-type) are very weak, and the collective response of

the arrays does not depend strongly on the positions (or disorder) of the molecules, thus reducing to a direct sum of the individual molecular contributions.

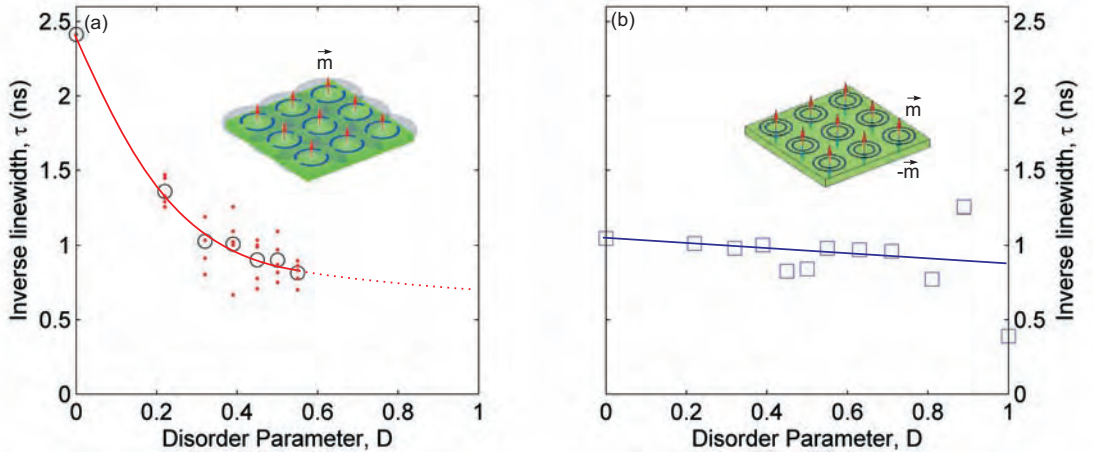

Fig. 6.6: Inverse linewidth, τ, for the asymmetrically-split ring (a) and the concentric ring (b) metamaterial. In (a), red points correspond to the five different realizations at each degree of disorder, while black empty circles correspond to the average inverse linewidth over five measurements. Red (a) and blue (b) solid lines serve as eye-guides. The corresponding insets illustrate the different origin of the trapped-mode resonance in the two cases.

Asymmetrically-split rings, on the other hand, present a more complex behaviour. They support both a weak electric dipole moment (by design) and a strong magnetic dipole moment, which arises directly from the anti-symmetric current configuration that also leads to the trapped-mode resonance. While in an infinite, regular array these magnetic dipoles are not allowed to radiate away from the plane of the array, this is no longer true when disorder is introduced and scattering losses are hence increased. This leads to a decrease of the intensity of the anti-symmetric current configuration and a broadening of the resonance. Furthermore, the ASR resonators can interact with one another through their induced magnetic dipole moments, which can also disturb the anti-symmetric current mode and degrade the quality of the trapped-mode resonance. In fact, one can argue that the decay of the quality of the resonance can be explained on the basis of these two effects, namely increased scattering losses due to magnetic dipole radiation and magnetic dipole-dipole interactions. At weak disorder, radiation losses are low allowing for the existence of strong magnetic dipole moments, and hence inter-element magnetic interactions should be at their strongest. By increasing the degree of disorder, magnetic dipole scattering is expected to become increasingly important, reducing the energy stored in the anti-symmetric current configuration and the magnitude of the induced magnetic dipole moments, thus minimizing the effect of magnetic dipole-dipole interactions.

Extending further this qualitative argument, one can recall that the inverse linewidth, τ, a measure of the resonance lifetime of a damped oscillator, should be roughly proportional to the energy stored in the resonator per cycle. In the case of the ASR metamaterial, energy is stored in the form of oscillating magnetic dipoles. It is argued here that upon disordering the array losses increase due to magnetic dipole scattering predominantly. The radiation losses of disordered magnetic dipole arrays can be easily calculated provided that interaction between the array

elements is limited to interference of the radiated far-fields. The results corresponding to $21x21$ arrays of non-interacting magnetic dipoles oriented perpendicular to the array plane are presented in Fig. 6.7b. For each degree of disorder, D, 10 different disordered arrays are considered and the corresponding scattered far-fields in the plane of the array are calculated [20]. As expected, the main feature of the graph is that the scattering losses (averaged over the 10 different realizations) increase. While in a regular array ($D = 0$) most of the energy is scattered in the plane of the array, when disorder is introduced, energy is radiated away from the array at directions outside the array plane and as a result the energy stored in the magnetic dipole moments of the meta-molecules diminishes. For comparison, the inverse linewidth of the disordered ASR metamaterial resonances and its variance are also presented in Fig. 6.7a. In particular, the inverse linewidth (which is proportional to the energy stored in the array) decreases with D, while the corresponding variance peaks close to $D \simeq 0.4$. Indeed, with increasing disorder the meta-molecules can be found further away from their initial positions, and thus the variance of meta-molecule configurations at each degree of disorder increases with increasing of the latter. On the other hand, strongly disordered array experience very high scattering losses that do not allow engaging the trapped-mode resonance independently of the specific meta-molecule arrangement. The same argument holds for interactions between the induced magnetic dipoles. Hence, the maximum in variance can be explained on the basis of competition between these two factors: increase of disorder leading to increase of the variance of meta-molecule arrangements and disappearance of the resonance at strong disorder.

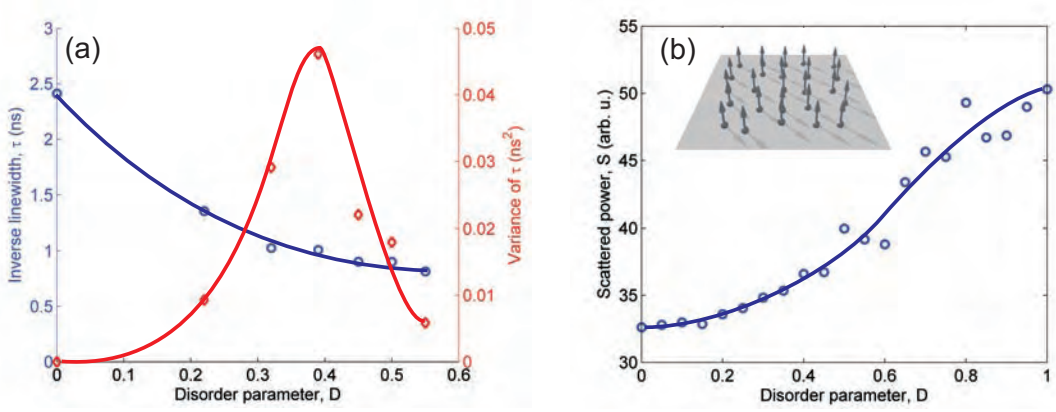

Fig. 6.7: (a) Average values (blue open circles) and variance (red empty rhombes) of the inverse linewidth, τ, as a function of the positional disorder parameter, D, for the case of asymmetrically-split rings. (b) Average values (blue open circles) of the scattering power, §, as a function of the positional disorder parameter, D, for the case of magnetic dipole arrays. Blue and red solid lines serve as eye-guides.

6.4 *Effect of orientational disorder in asymmetrically-split ring metamaterials*

The inherent anisotropy of the ASR resonator allows for a different type of disorder to be studied, i.e. orientational disorder. Introduction of such disorder provides further insights into the behaviour of coherent metamaterials and leads to situations very similar to other physical systems

with strong interactions of magnetic type.

Orientational disorder is introduced in the ASR metamaterial by rotating by 180^0 (flipping) randomly chosen unit cells. The disorder was quantified by the ratio, F, of rotated (flipped) ASRs over the total number of unit cells. For each value of the disorder parameter, F, five different ASR arrays were manufactured [2].

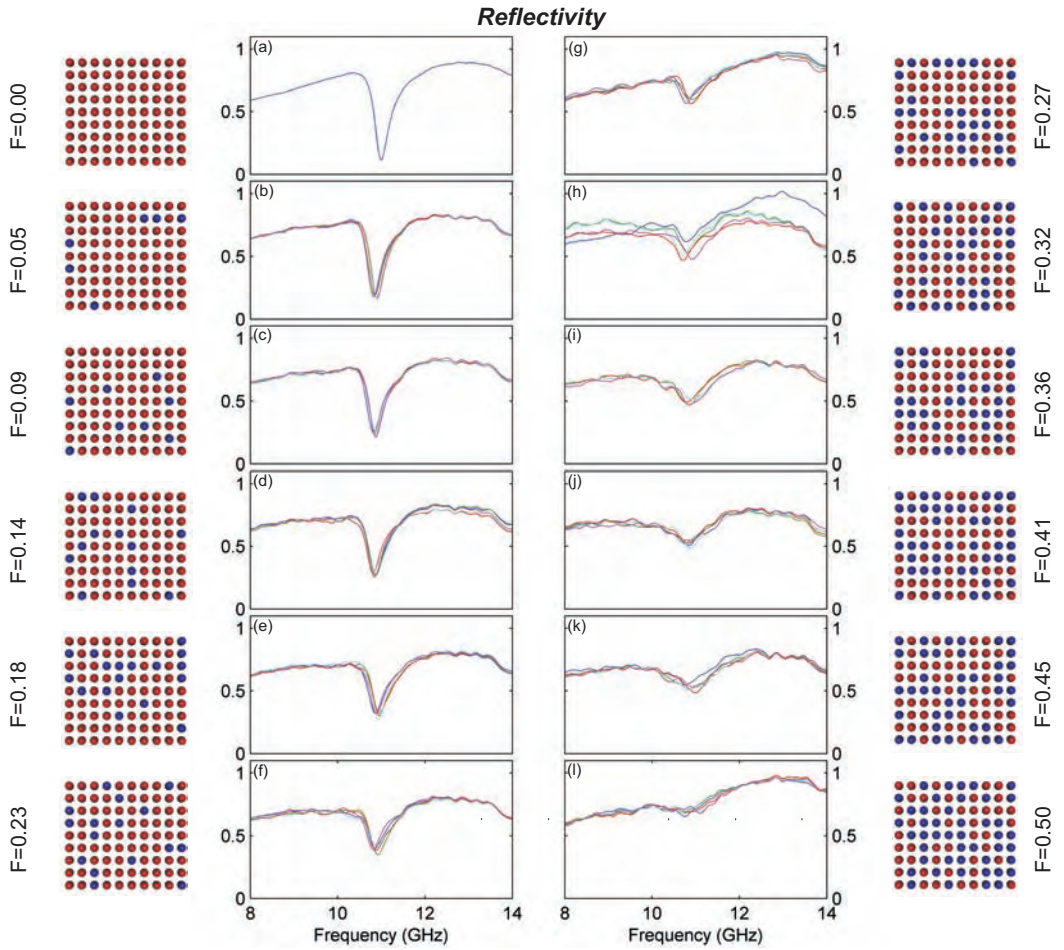

Fig. 6.8: Reflection of disordered asymmetrically-split ring (a-g) and concentric ring (h-n) metamaterial arrays for different values $(0.63-1)$ of the disorder parameter, F. In the case of asymmetrically-split rings, five different realizations corresponded to to each value of F. The left column illustrates the degree of disorder for each value of F.

The response of the disordered arrays under plane wave illumination was studied and the corresponding results are shown in Fig. 6.8. Panels (a)-(l) demonstrate the strong dependence of the ASR metamaterial to orientational disorder, with the trapped-mode resonance degrading gradually with increasing number of flipped elements. However, in contrast to the quick disappearance of the resonance in the case of positional disorder, the ASR metamaterial appears to be less influenced by orientational disorder, and the trapped-mode resonance can be distinguished even when 45% of the ASRs are flipped. Furthermore, while at most degrees of disorder all five different realizations present very similar reflection spectra, these become distinctively different

[2] The parameters of the asymmetrically-split ring arrays and the experimental conditions are the same with section 63.

close to $F = 0.32$. This becomes more evident in Fig. 6.9, where the inverse linewidth, τ, is presented as a function of the disorder parameter F. A quick decrease in the resonance lifetime is observed at the region of $F = 0.32$ coinciding with an increase in the spread of the estimated values from the five different realizations.

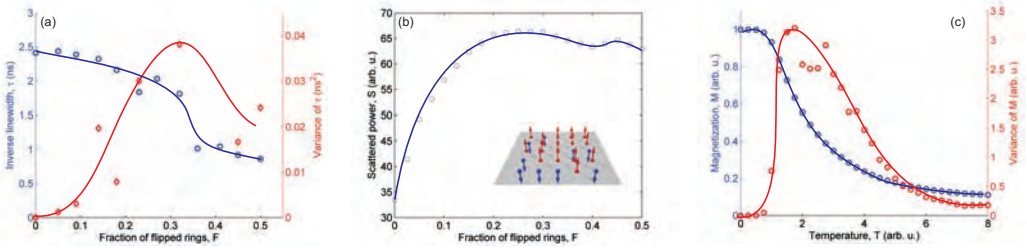

Fig. 6.9: (a) Average values (blue open circles) and variance (red empty rhombes) of the inverse linewidth, τ, as a function of the orientational disorder parameter, F, for the case of asymmetrically-split rings. (b) Average values (blue open circles) of the scattering power, §, as a function of the orientational disorder parameter, F, for the case of magnetic dipole arrays. (c) Average values and variance of the magnetization of a $10x10$ Ising lattice estimated by Monte-Carlo simulations. Blue and red solid lines serve as eye-guides.

One can attempt to attribute the decay of the resonance lifetime upon the introduction of orientational disorder in the metamaterial arrays, to scattering from the magnetic dipoles induced at the trapped-mode resonance. The results of such simulations are shown in Fig. 6.9b, where the scattered wave intensity away from the plane of the array is presented as a function of the fraction, F of flipped dipoles, for $21x21$ arrays of non-interacting magnetic dipoles oriented perpendicular to the array plane. The energy radiated away from the plane of the array increases rapidly for $F < 0.2$ and remains roughly constant for higher values of F. In contrast to the behaviour of the ASR metamaterial, no sudden increase of scattered intensity occurs at $F \simeq 0.3$, implying that a different mechanism is responsible for the degrading of the trapped-mode resonance. In fact, the rapid decrease of the inverse linewidth at $F = 0.32$ with the simultaneous increase of variance is reminiscent of phase transitions in other magnetic systems, such as the Ising model [21]. The average magnetization over 100 realizations of a $10x10$ spin lattice with nearest-neighbour interactions is presented as a function of temperature in Fig. 6.9c. A rapid decay, similar to the one observed for the ASR metamaterial inverse linewidth, is observed near the critical temperature, $T \simeq 2.3$, accompanied with a maximum in the fluctuations of the magnetization over different realizations. This phenomenological similarity implies that the behaviour of the ASR metamaterial could be explained in terms of inter-metamolecule magnetic dipole interactions.

6.5 Lasing Spaser

The two planar metamaterial structures studied in this chapter are examples of artificial media with strong and weak inter-meta-molecular interactions representing two characteristic and antipode classes of what it is called here "coherent" and "incoherent" metamaterials. The fundamental difference in the nature of their narrow resonances, collective in the first case and individual in the latter, determines the potential applications of these structures, most notably

the lasing spaser [22].

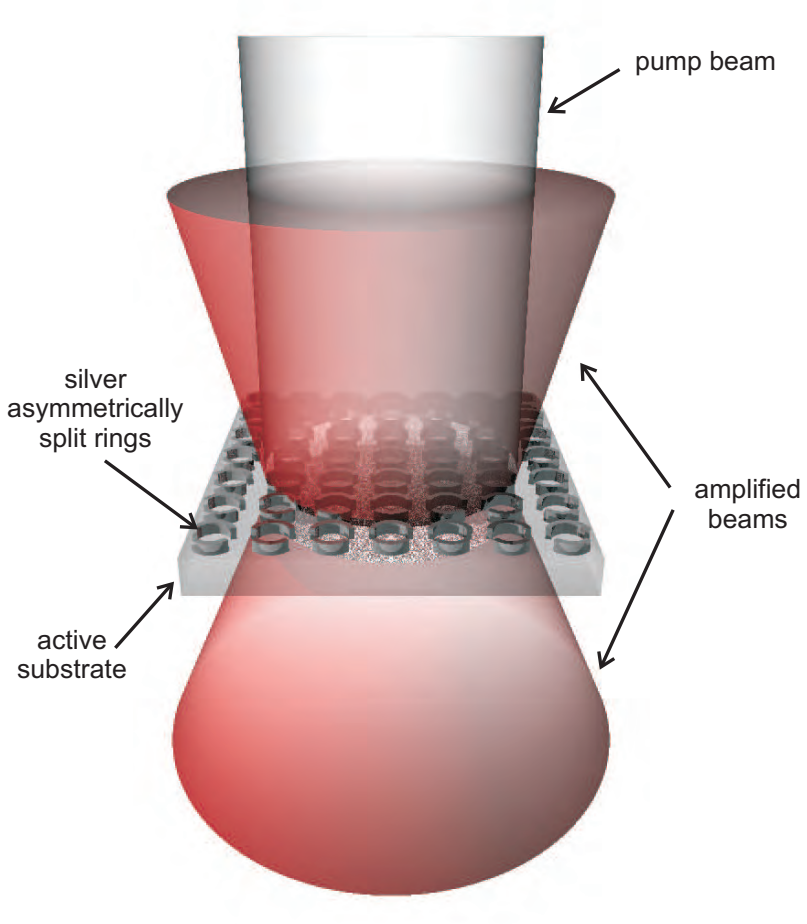

Fig. 6.10: Illustration of lasing spaser concept. An array of asymmetrically-split rings supported by an active substrate is pumped by a laser beam. As a result, an amplified narrow-divergent beam emerges.

The lasing spaser is an extension of the spaser (surface plasmon amplification by stimulated emission of radiation) [25], which is a quantum amplifier of surface plasmons. A spaser works in a way analogous to the laser, with a resonant plasmonic material replacing the laser cavity and emitting surface plasmons instead of electromagnetic radiation. Such a system is uncoupled to free-space radiative modes in order to increase the efficiency of the surface plasmon amplification. The lasing spaser is based on the same effect. However, instead of being completely uncoupled, the plasmonic resonators in this case are weakly coupled to free-space propagating modes. This results in a planar narrow-diversion coherent source of electromagnetic radiation that is fuelled by plasmonic oscillations of a two-dimensional resonator array, where the coherency of the optical source is ensured by the synchronous oscillations of the plasmonic currents in the array.

In a "coherent" metamaterial formed by asymmetrically-split rings, the regular array gives the highest value of quality factor compared to disordered arrays. It is argued here that, similarly, when both phased (coherent) and uncorrelated (incoherent) current oscillations are present in an array of meta-molecules of this type, the uncorrelated component will decay more rapidly.

Therefore in the presence of gain the phased, coherent component of amplified spontaneous current fluctuations will win over incoherent fluctuations providing for a self-starting regime of the lasing spaser.

Here a first step towards this direction is undertaken and the amplifying properties of an ASR metamaterial in the presence of gain are studied numerically. The diameter of the simulated ASR-resonators is 140 nm, with a unit cell of 210×210 nm. The angular lengths of the metallic wire segments correspond to angles $\beta_1 = 160^o$, $\beta_2 = 125^o$, while the size of their cross-section is 20×50 nm. The metal of the nano-wires is assumed to be silver with a dielectric constant described by the Drude model. The substrate is 100 nm thick with $\epsilon' = 9.5$, and gain is introduced through the imaginary part ϵ'' of the substrate's dielectric constant, which is related to the gain/attenuation coefficient α by $\frac{2\pi}{\lambda} Im(\sqrt{\epsilon' + i\epsilon''})$.

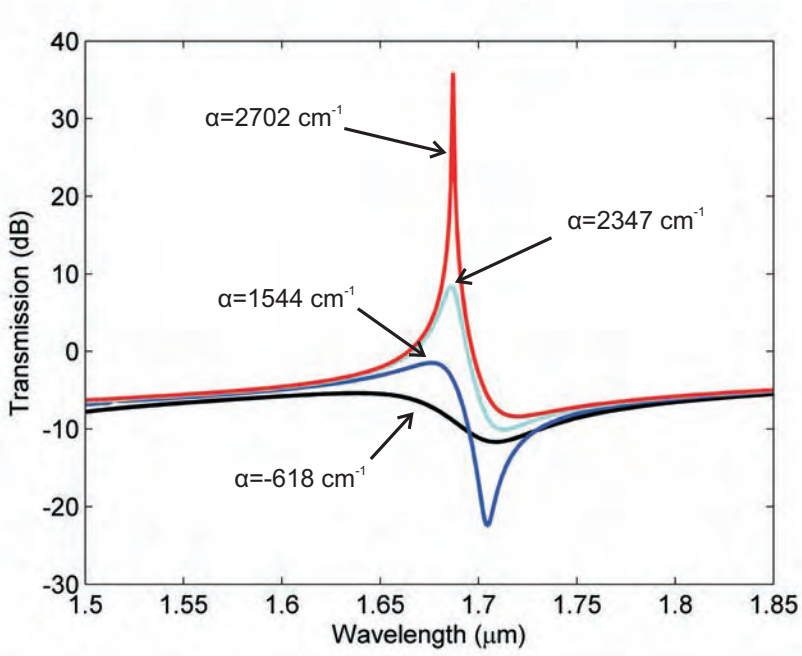

Fig. 6.11: Characteristic transmission spectra of the ASR metamaterial on an active substrate for different values of the substrate gain coefficient α.

Figure 6.11 shows the transmission characteristics of the optical ASR array for different levels of bare substrate gain presented in terms of the gain coefficient α. For negative values of α (lossy substrate) the metamaterial attenuates electromagnetic radiation, principally due to dissipation losses in the dielectric substrate. With increasing the levels of gain, material losses in the metamaterial are compensated, and attenuation gives place to strong amplification which peaks at the frequency of the trapped-mode ($\lambda \simeq 1.68$).

The conditions under which amplification occurs are better seen in Fig. 6.12, where transmission and reflection are presented in the wavelength-gain plane. The dashed contours mark the regions of unity transmission and reflection, respectively. The corresponding threshold for the gain coefficient is $\alpha_{th} \simeq 1850$ cm^{-1} in transmission and $\alpha_{th} \simeq 900$ cm^{-1} in reflection. Strong amplification takes place in a small elliptical area within the unity contours and both transmission and reflection peak simultaneously for $\alpha \simeq 2700$ cm^{-1} and $\lambda = 1.68$ μm, exceeding 35 dB

and 25 dB, respectively. At the same time the amplified transmission and reflection peak become increasingly narrower and collapse at maximum amplification. Further increase in the substrate gain leads to a rapid decrease in small-signal amplification and broadening of the amplification peak. This is because gain broadens the resonance in the same way that losses broaden absorbtion resonances, and achieving anti-phase oscillations of currents in the split-ring arcs of the plasmonic resonator becomes more difficult as radiation losses increase.

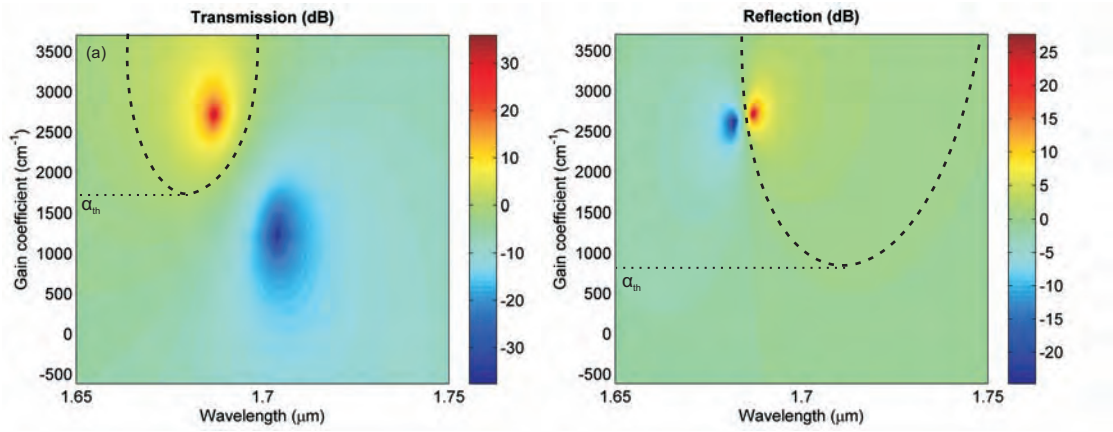

Fig. 6.12: Transmission (a) and reflection (b) of an ASR metamaterial as a function of wavelength and substrate gain coefficient α. The dashed contours mark the positions of unity transmission and reflection, respectively, and surround the areas where amplification occurs. The threshold values, α_{th}, of the gain coefficient are also marked.

The increase of amplification and the collapse of the linewidth can be clearly seen in Fig. 6.13, where the transmission levels at the trapped-mode resonance peak and the line width (full width at half maximum) are plotted as a function of the gain coefficient, α, for the optical ASR metamaterial as well as for a similar structure resonating at 8.4 μm [3]. The curves for both cases are qualitatively similar demonstrating the scalability of the concept: significant amplification occurs for moderate levels of gain with simultaneous collapse of the linewidth and is followed by a sharp decrease of maximum transmitted intensity. However, there is a significant difference in the required levels of gain, principally due to the dissipative losses in the metal that affect the performance of the optical ASR metamaterial.

The small scattering losses of the current-modes in the metamaterial array make the levels of threshold gain and gain needed to achieve peak amplification of $35-40$ dB practically attainable. For instance, quantum well structures can provide gain of the order of 10^3 cm^{-1} [26], which is similar to the threshold value required for an ASR array operating at 1.65 μm. Furthermore, quantum cascade amplifiers can readily provide the gain values needed in the mid-infrared case, since attainable gain coefficients in this wavelength range exceed 100 cm^{-1} [27]. This easy-to-achieve threshold gain condition gives a crucial advantage over the recent suggestions to combine amplifying media with nano-shell [28] and horseshoe resonant elements [29] to create a compact plasmonic nanolaser. There the high dipole radiation losses of plasmonic resonator make the threshold gain level extremely difficult to achieve. Furthermore, the lasing spaser allows high

[3] Transmission spectra estimated by method of moments simulations on a mid infrared ASR array were provided by Prof. S. L. Prosvirnin. The inner and outer radius of the infinitely-thin split-ring was 575 nm and 625 nm, respectively. The 1.5 μm-pitch metamaterial array was placed on a 2 μm active substrate with dielectric permittivity $\epsilon = 10.9$.

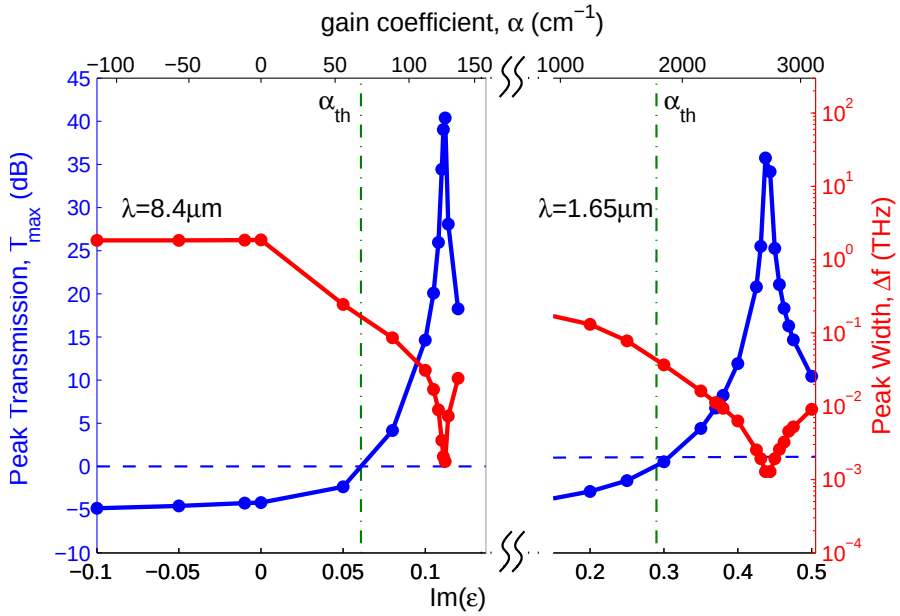

Fig. 6.13: Transmission properties of near- and mid-IR resonator arrays. Small-signal amplification (blue) and spectral width (red) of the resonant transmission peak as a function of gain level in the substrate. Corresponding values for the imaginary part of the substrate permittivity are also given. The horizontal dashed blue lines represent the levels of single-pass amplification through the bare substrate. The vertical dash-dot lines mark the threshold values of the gain coefficient.

amplification and lasing in a very thin layer of material with a modest gain level, making it a very practical proposition. The thin-layer geometry is a desirable feature for some highly-integrated devices and from the point of view of heat management and integration. Here the amplification/lasing frequency is determined by size of the ring and may be tuned to match luminescence resonances in a large variety of gain media. All together this makes the lasing spaser a generic concept for many applications.

6.6 Conclusions

Two antipode classes of metamaterials have been identified, with strong and weak inter-element interactions. The former provides a collective resonant response which is not available in a single meta-molecule, while the response of the latter is essentially the same, irrespectively of whether a single unit cell or an infinite array is considered. This characteristics lead to very different behaviour upon disordering the regular arrays, with ASRs being strongly affected even by weak or moderate disorder, and CRs ratining their resonant response even in the presence of very strong disorder. This opens avenues for novle applications, such the lasing spaser introduced int he previous chpater, where the coherency of the ASRmetamaerial can provide for a self-starting regime in the presence of gain. On the contrary, "incoherent" metamaterials do not possess a mechanism of synchronization of current oscillation in individual meta-molecules and are not suitable for lasing spaser applications. However,the resonant properties of "incoherent" metamaterials are more tolerant to disorder making them more suitable for manufacturing using methods prone to imperfections such as self-assembly [30].

BIBLIOGRAPHY

[1] T. Weiland, R. Schuhmann, R. B. Greegor, C. G. Parazzoli, A. M. Vetter, D. R. Smith, D. C. Vier, and S. Schultz, Ab initio numerical simulation of left-handed metamaterials: Comparison of calculations and experiments, *Journal of Applied Physics* **90**, 5419 (2001).

[2] K. Aydin, K. Guven, N. Katsarakis, C. M. Soukoulis, E. Ozbay, Effect of disorder on magnetic resonance band gap of split-ring resonator structures, *Optics Express* **12**, 5896 (2004).

[3] S. A. Tretyakov and A. J. Vitanen, Line of periodically arrange passived dipole scatterers, *Electrical Engineering* **82**, 353 (2000).

[4] E. Shamonina, V. A. Kalinin, K. H. Ringhofer, L. Solymar, Magneto-inductive waveguide, *Electronics Letters* **38**, 371 (2002).

[5] M. Beruete, F. Falcone, M. J. Freire, R. Marques, and J. D. Baena, Electroinductive waves in chains of complementary metamaterial elements, *Applied Physics Letters* **88**, 083503 (2006).

[6] E. Shamonina, V. A. Kalinin, K. H. Ringhofer, and L. Solymar. Magnetoinductive waves in one, two and three dimensions. *Journal of Applied Physics* **92**, 6252 (2002).

[7] M. C. K. Wiltshire, E. Shamonina, I. R. Young, and L. Solymar. Dispersion characteristics of magneto-inductive waves: comparison between theory and experiment. *Electronics Letters* **39**, 215 (2003).

[8] I. V. Shadrivov, A. N. Reznik, and Y. S. Kivshar. Magnetoinductive waves in arrays of split-ring resonators. *Physica B: Condensed Matter* **394**, 180 (2006).

[9] E. Shamonina and L. Solymar. Magneto-inductive waves supported by metamaterial elements: components for a one-dimensional waveguide. *Journal of Physics D: Applied Physics* **37**, 362 (2004).

[10] R. R. A. Syms, I. R. Young, and L. Solymar. Low-loss magneto-inductive waveguides. *Journal of Physics D: Applied Physics* **39**, 3945 (2006).

[11] M. J. Freire, R. Marques, F. Medina, M. A. G. Laso, and F. Martin. Planar magneto-inductive wave transducers: Theory and applications. *Applied Physics Letters* **85**, 4439 (2004).

[12] R. R. A. Syms, E. Shamonina, V. Kalinin, and L. Solymar. A theory of metamaterials based on periodically loaded transmission lines: Interaction between magnetoinductive and electromagnetic waves. *Journal of Applied Physics* **97**, 064909 (2005).

[13] M. J. Freire and R. Marques. Planar magnetoinductive lens for three-dimensional subwavelength imaging. *Applied Physics Letters* **86**, 182505 (2005).

[14] L. Solymar, O. Zhuromskyy, O. Sydoruk, E. Shamonina, I. R. Young, and R. R. A. Syms. Rotational resonance of magnetoinductive waves: Basic concept and application to nuclear magnetic resonance. *Journal of Applied Physics* **99**, 123908 (2006).

[15] A. A. Zharov, I. V. Shadrivov, and Y. S. Kivshar. Suppression of left-handed properties in disordered metamaterials. *Journal of Applied Physics* **97**, 113906 (2005).

[16] M. V. Gorkunov, S. A. Gredeskul, I. V. Shadrivov, and Y. S. Kivshar. Effect of microscopic disorder on magnetic properties of metamaterials. *Physical Review E* **73**, 056605 (2006).

[17] J. Gollub, T. Hand, S. Saujuyigbe, S. Mendonca, S. Cummer, and D. R. Smith. Characterizing the effects of disorder in metamaterial structures. *Applied Physics Letters* **91**, 162907 (2007).

[18] A. Alu and N. Engheta. On role of random disorders and imperfections on performance of metamaterials. *IEEE Antennas and Propagation Society International Symposium 2007*, 2897 (2007).

[19] X. Zhou, X. P. Zhao, and Y. Liu. Disorder effects of left-handed metamaterials with unitary dendritic structure cell. *Optics Express* **16**, 7674 (2008).

[20] D. J. Griffiths. *Introduction to electrodynamics* (Prentice Hall, 1981).

[21] E. Ising, The theory of ferromagnetism. *Zeitschrift der Physik* **31**, 253 (1925).

[22] N. I. Zheludev, S. L. Prosvirnin, N. Papasimakis, & V. A. Fedotov. Lasing spaser. *Nature Photonics* **2**, 351-354 (2008).

[23] N. Liu, S. Kaiser, and H. Giessen. Magnetoinductive and electroinductive coupling in plasmonic metamaterial molecules. *Advanced Materials* **20**, 1 (2008).

[24] N. Liu, L. Fu, S. Kaiser, H. Schweitzer, and H. Giessen. Plasmonic building blocks for magnetic moleclues in three-dimensional optical metamaterials. *Advanced Materials* **20**, 3859 (2008).

[25] D. J. Bergman & M. I. Stockman, Surface Plasmon Amplification by Stimulated Emission of Radiation: Quantum Generation of Coherent Surface Plasmons in Nanosystems. *Physical Review Letters* **90,** 027402 (2003).

[26] H. Carrere, X. Marie, L. Lombez & T. Amand, Optical gain of InGaAsN/InP quantum wells for laser applications. *Applied Physics Letters* **89,** 181115 (2006).

[27] M. Troccoli, C. Gmachl, F. Capasso, D. L. Sivco & A. Y. Cho, Mid-infrared ($\lambda \approx 7.4\ \mu m$) quantum cascade laser amplifier for high power single-mode emission and improved beam quality. *Applied Physics Letters* **80** 4103 (2002).

[28] J. A. Gordon & R. W. Ziolkowski, The design and simulated performance of a coated nanoparticle laser. *Optics Express* **15,** 2622 (2007).

[29] A. K. Sarychev & G. Tartakovsky, Magnetic plasmonic metamaterials in actively pumped host medium and plasmonic nanolaser. *Phys. Rev. B* **75,** 085436 (2007).

[30] D. A. Pawlak, Metamaterials and photonics crystals - potential applications for self-organized eutectic micro- and nanostructures. *Scientia Plena* **4**, 014801 (2008).

7. SURFACE STATES OF STRUCTURED INTERFACES

7.1 Introduction

The study of the transmission of electromagnetic radiation through subwavelength holes has been initiated by the work of Bethe who showed analytically by appealing to Babinet's principle, that the transmitted intensity through a hole of radius r in a infinitely thin perfectly conducting plane, decays as $(r/\lambda)^4$ in the limit of very small holes ($r/\lambda \to 0$), where λ is the free space wavelength of the incident wave [1]. Later, Bouwkamp corrected Bethe's theory by including terms of higher order in r/λ [2, 3]. Although the transmission through an array of holes, both in infinitely thin and thick conducting planes has been extensively studied in the microwave part of the spectrum [4, 5, 6, 7], the interest in this phenomenon was recently renewed by the work of Ebbesen et al [8], who demonstrated experimentally that the transmission through nano-structured metal films exceeds the original predictions of Bethe [1] by several orders of magnitude. When the transmission was normalized by the filling factor of the pattern, i.e. the ratio of the sample area covered by holes over the full sample area, it was shown that more light was transmitted than was incident directly on the holes, which implies that the transmission is mediated by inter-hole interaction. In fact, measurements at different angles of incidence further support this hypothesis, since the obtained band structure diagram demonstrates clear band gaps, which are consistent with the dispersion relation for surface plasmons on a periodically corrugated surface. Later works confirmed the surface plasmon transmission mechanism but highlighted also the role of Wood's anomalies [9, 10, 11], which occur whenever a diffraction order becomes parallel to the surface of the film. At wavelengths where Wood's anomalies appear, reflection becomes maximum which corresponds to transmission minima. However, in the vicinity of these wavelengths surface bound states exist which can couple to external radiation though the periodicity of the lattice. In the optical domain such states are called surface plasmons, while in the case of microwaves they are common surface currents, the main difference between them being that plasmons are formed by bound charges and can penetrate the bulk metal. This was further clarified by Pendry who showed that a periodically structured perfectly conducting surface can be described by an effective permittivity resembling the behavior of plasmons and named the bound states as "spoof" plasmons [12].

A different but equivalent approach was suggested as a description of the phenomenon based also on the concept of dynamical diffraction and Wood's anomalies, but employing Babinet's principle to result in a simpler description [13, 14]. The complementary screen of the hole array is considered, which is comprised by metal disks. In the limit of very small radius over wavelength ratio, the disks can be approximated by dipoles with known polarizability and the reflection coefficient of the array can be calculated. However, in this case, the field on each site of the structure includes non-local contributions from the rest of the array. By Babinet's principle,

the transmission of the hole array can be found from the reflectivity of the complementary disk array.

Recently, the transmission of quasi-periodic hole arrays has been also investigated both experimentally [15, 16, 17, 18] and theoretically [19]. Underlining the role of the periodicity and long range order in the extraordinary transmission phenomenon, the theory of ordered arrays was extended to include the quasi-periodic case [19], predicting that the physical mechanisms are the same in both cases.

7.2 Theoretical Considerations

It is known that a single hole on a thin [1] or a thick [20] metal film can be represented by a magnetic dipole parallel to the surface and an electric dipole perpendicular to it. In the case of a hole array, the collective response admits a representation in terms of the self-consistent polarization $\vec{p}_{\vec{R}}$ of each hole at the positions $\vec{R}$ in response to an external field $\vec{E}^{\text{ext}}$ plus the field induced by other holes $\vec{R}' \neq \vec{R}$ via the hole polarizability α, that is,

$$\vec{p}_{\vec{R}} = \alpha[E^{\text{ext}}(\vec{R}) + \sum_{\vec{R}' \neq \vec{R}} G(\vec{R} - \vec{R}')\vec{p}_{\vec{R}'}], \tag{7.1}$$

where $G(\vec{R} - \vec{R}')$ describes the field produced at hole $\vec{R}$ by the polarization of the hole at $\vec{R}'$. In the small hole limit ($\lambda \gg r$, where r is the hole radius), we can retain only the dipolar component of $\vec{p}$ [20]. By considering an incident plane wave with $\vec{k}_{\parallel}$ momentum parallel to the film and assuming a $\exp(i\vec{k}_{\parallel} \cdot \vec{R})$ spatial dependence for the hole polarizability [1], Eq. (7.1) can be rewritten as

$$\vec{p}_{\vec{R}} \approx \frac{1}{\frac{1}{\alpha} - G_{\vec{k}_{\parallel}}} E^{\text{ext}}(\vec{R}), \tag{7.2}$$

where $G_{\vec{k}_{\parallel}} = \sum_{\vec{R} \neq 0} G(\vec{R}) e^{-i\vec{k}_{\parallel} \cdot \vec{R}}$ is the sum of the dipole-dipole interaction over the quasi-lattice. Finally, the transmission T is given by the coherent superposition of the far field produced by all induced dipoles, or equivalently, the transmission along a direction defined by a projected parallel momentum $\vec{k}_{\parallel}^{\text{out}}$ is the far field produced by the dipole

$$\sum_{\vec{R}} \vec{p}_{\vec{R}} e^{-i\vec{k}_{\parallel}^{\text{out}} \cdot \vec{R}}. \tag{7.3}$$

The lattice sum $G_{\vec{k}_{\parallel}}$ exhibits pronounced maxima when the main diffraction peaks become grazing, which are the equivalent of the Wood anomaly condition in quasicrystal arrays. According to Eq. (7.2), the transmission will actually exhibit a dip at the divergences of $G_{\vec{k}_{\parallel}}$ and a maximum signalled by the minimum of $|1/\alpha - G_{\vec{k}_{\parallel}}|$.

In order to examine the origin of the extraordinary transmission through perforated metal surfaces, a quasi-periodic pattern of holes on a metal film was considered. A part of the pattern comprised by 1000 sites and its Fourier transform are shown in Fig. 7.1, where the long-range

[1] Long-range interaction between holes dictates the transmission resonances, so that local variations between neighboring holes can be overlooked in this coherent-phase approximation, in which the phase imposed by the external field drives the effective phase difference in the response of distant holes.

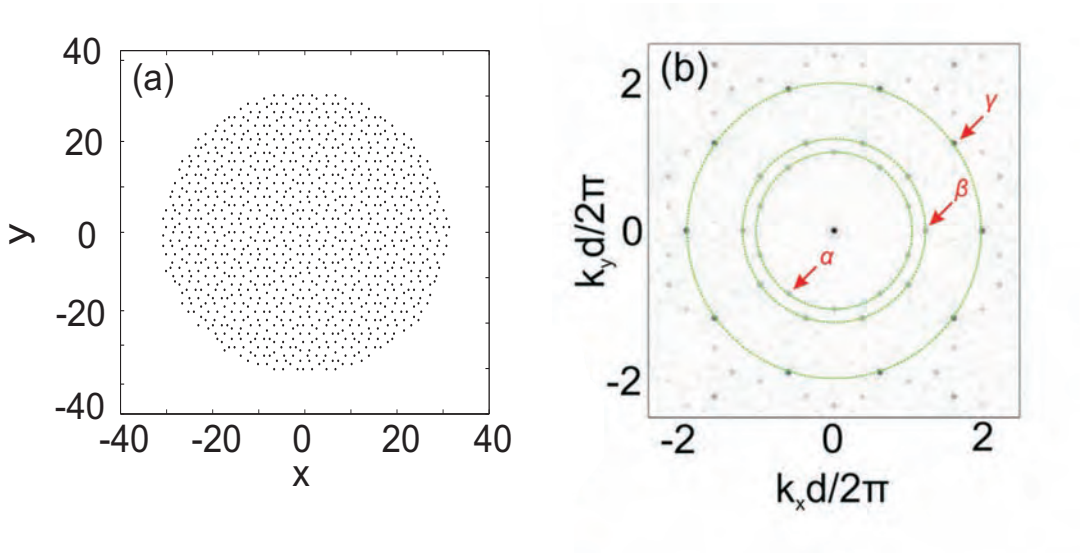

Fig. 7.1: The studied quasi-periodic pattern (a) and its Fourier transform (b).

order of the pattern and the ten-fold symmetry of the reciprocal space are evident. The pattern is characterized by the minimum hole distance d (center to center), which represents the scale of the pattern. Since the wavelength at which extraordinary transmission occurs is related to the periodicity of the array, one expects that in the case of a quasi-crystal array of holes on a self-standing metal film, maxima of transmission will appear at wavelengths near the maxima of the Fourier transform. However, these approximations are valid only in the limit of an infinite number of holes. For a small number of holes, the long-range order is not that pronounced and the analysis is more complicated. Moreover, the aspect ratio of the holes must be taken into account. By scaling the initial pattern appropriately, two different types of samples were manufactured, one in the microwave part of the spectrum and one in the optical.

7.3 Enhanced Microwave Transmission

The microwave pattern consisted of 313 circular holes with radius of 0.46 cm, resulting in a filling factor (defined as the area occupied by holes over the whole sample area) of approximately 15%. In this case the minimum hole distance d was $d = 2.31cm$, since the quasi-crystal was scaled to partially fill a rectangular area 44.2 cm x 45.7 cm (the sample size). The first microwave sample was a 0.5 mm thick self-standing Al sheet, while the second was lithographically manufactured by etching a 35 μm Cu film residing on a 1.5 mm thick dielectric substrate with $\epsilon = 3.5 - 0.03i$ (see Fig. 7.2).

The experimental results for the polarization along the y-axis (see Fig. 7.2a) are shown in Fig. 7.3 (solid curves) and are normalized only to transmission through free space. For the orthogonal polarization similar (although not identical) results were obtained. For comparison theoretical predictions derived in the coherent-phase approximation are also included. In all cases, the transmission through the hole arrays exceeds Bethe's predictions, since about ~ 10 times more intensity than what is directly incident in the area occupied by holes is transmitted.

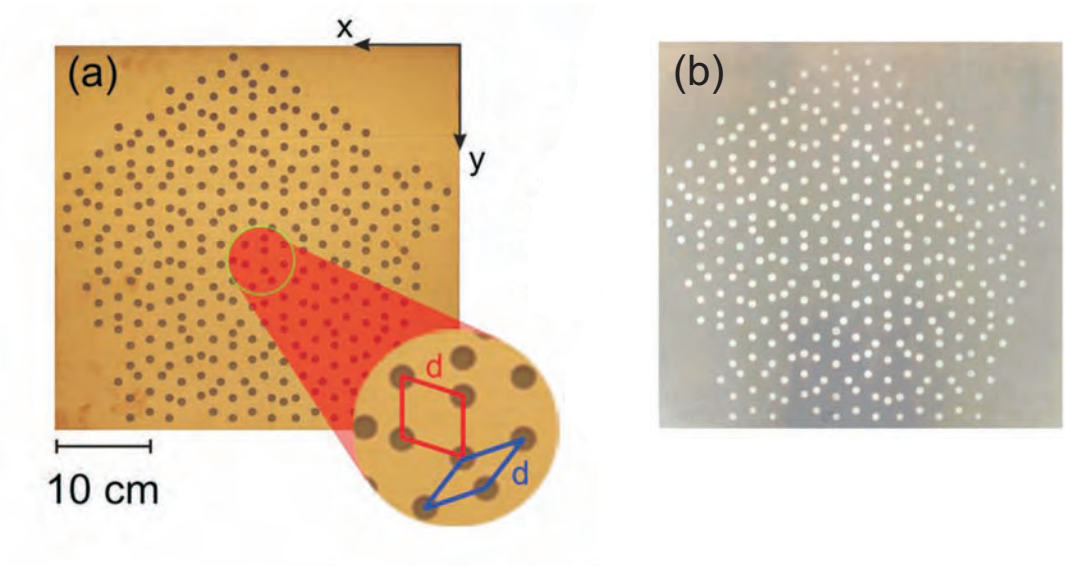

Fig. 7.2: Microwave samples: Cu on dielectric (a) and self-standing Al (b) quasicrystal.

In particular, for the self-standing array (Fig. 7.3a), two sharp transmissions peaks can be seen at 2.02 *cm* (I) and 2.34 *cm* (II) wavelengths on a slowly decaying transmission background, which as expected, lie very close to the positions predicted by theory. Peaks of shorter wavelength arising from lower spatial frequencies (e.g., γ) lie below the measured frequency range. The width of the peaks is primarily controlled by the number of holes on the sample, since, given the manufacturing accuracy, broadening effects due to fabrication imperfections are unlikely. The magnitude of the peaks is 50% and 48% respectively, while at the same time the phase change of the transmitted wave for both peaks is close to zero.

The situation changes dramatically when the metal film is supported by a dielectric substrate (Fig. 7.3b). Peaks I and II become considerably weaker (30% and 31%) and are separated by a point of zero transmission at 2.1 *cm*, where the phase is undefined. This phase singularity could be attributed to enhancement of a Wood anomaly triggered by the metal-dielectric interface. Moreover, a new transmission peak appears at 2.93 *cm* (III) (Fig. 7.3b), where 65% transmission is accompanied by a zero phase change. If, in addition to the dielectric substrate, a superstrate of the same thickness and permittivity is introduced (Fig. 7.3c), peaks I and II are no longer visible, peak III increases in magnitude reaching 90%, and the phase at the maximum is again zero rendering the structure virtually *invisible*. This is a behavior typical of Breit-Wigner resonances, which can be understood by noticing that Eq. (7.2) becomes a Lorentzian near the transmission maximum, the phase of which changes sign when the real part of the denominator vanishes (i.e., right on resonance), while the imaginary part evolves smoothly.

The more complicated spectral shape observed for the structures of Figs. 7.3b and 7.3c, results from a complex interplay between hole polarizabilities, lattice sums, and guided modes in the dielectric slabs, which is well accounted for by analytical theory (dashed curves). While the interaction between holes in the self-standing film (making up the $G_{\|}$ lattice sum) has the same distance scaling as the dipole-dipole interaction in free space, in the case of supported

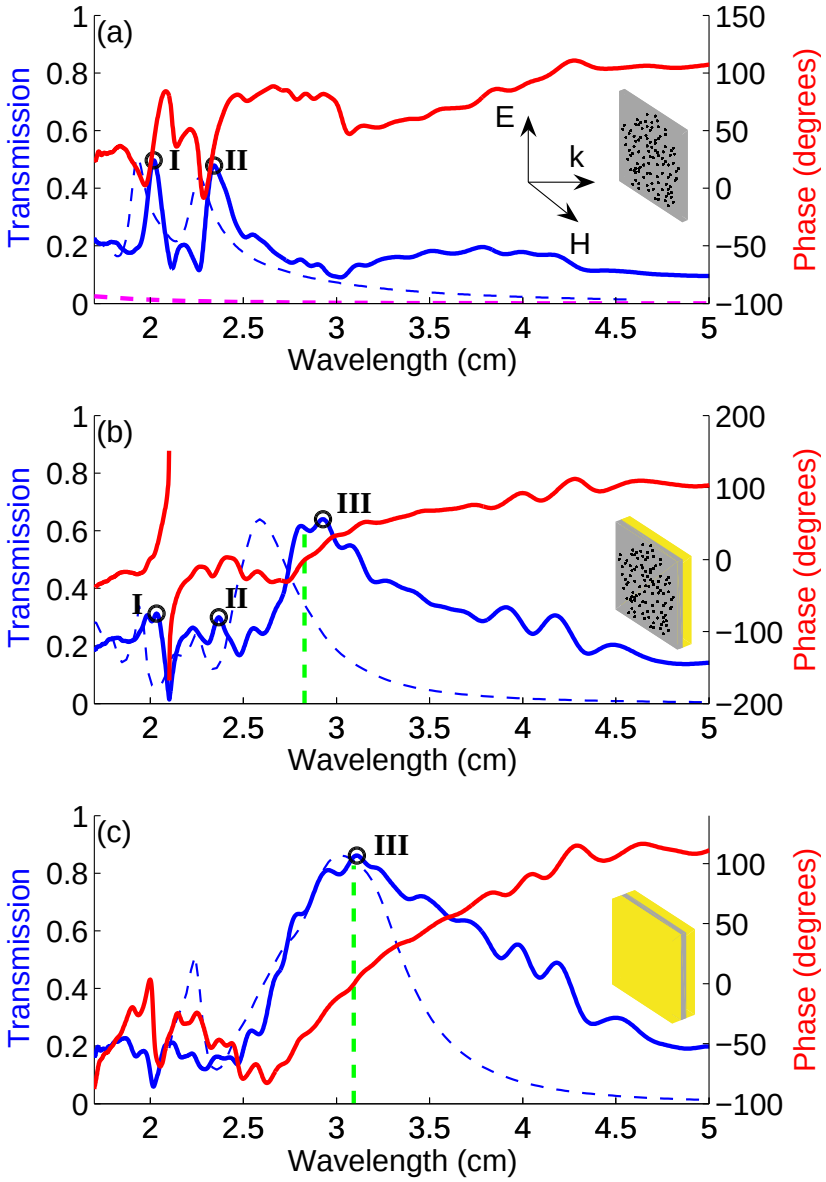

Fig. 7.3: Normal incidence transmission spectra through quasicrystal hole arrays on (a) a self-standing Al film, (b) a copper film supported by a dielectric substrate and (c) a copper film sandwiched between two identical dielectric slabs. The Bethe prediction is shown by the dashed purple line in (a), while the green lines in (b) and (c) mark the wavelength positions of *invisible metal* states, where high transmission is accompanied by zero phase change. Experimental results (solid curves) are compared with theoretical calculations obtained in the coherent-phase approximation [Eqs. (7.2) and (7.3)] (dashed curves). The latter are normalized to match the maximum of the corresponding experimental curves. (Theoretical spectra were provided by Prof. J. Garcia de Abajo.

films the situation is qualitatively different, due to the existence of cutoff-free guided TM-modes in the dielectric. These surface-like waves trigger a slower decay with distance of the inter-hole interaction. Furthermore, hole-mediated coupling of the external light to the TM modes provides a *loss* channel that results in significant broadening of peak III, with absorption in the dielectric adding an insignificant contribution. In contrast to the case of infinitely thick dielectrics, where the metal-dielectric interface would give rise to two new long wavelength peaks, in the present case, the finite thickness of the dielectric changes significantly the shape of the hole polarizability and the $G_{\parallel}$ lattice sum resulting in a single transmission peak (III) at long wavelengths and suppression of peaks (I, II) originating from the metal-air interface.

7.4 Enhanced Optical Transmission

The optical sample was manufactured by electron beam lithography on a $100nm$ thick Al film residing on a $500\mu m$ silica substrate. The skin depth of Al, defined as the distance at which the electric field is decreased by a factor $1/e$, is less than $20nm$ at the wavelengths of interest, therefore the transmission through the bulk metal can be neglected. The pattern consisted of 14194 square holes of side length $0.2\mu m$ and occupied a circular area of approximately $250\mu m$ diameter, resulting in a filling factor of 1.3%. The characteristic minimum distance between holes was $1.2\mu m$. The quality of the sample was confirmed by scanning electron microscopy (figure 7.4).

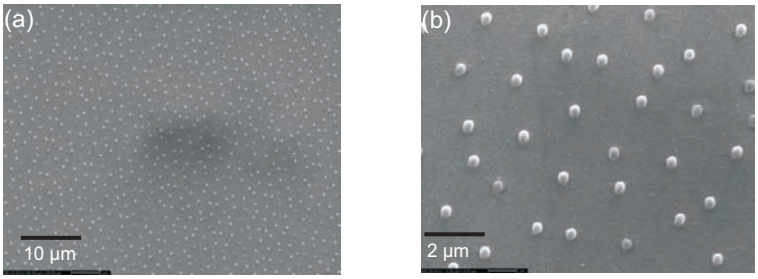

Fig. 7.4: SEM pictures of the optical quasicrystal sample.

The measurements [2] were performed in a free-space setup with a super-continuum photonic crystal fiber laser and an optical spectrum analyzer, operating in the range of 0.47 to $1.77\mu m$. Two diaphragms were used in order to reduce the intensity of the beam in order to avoid excessive heating of the sample. The sample was placed at the focal point of a converging lens, so that the area of the metal film illuminated by the beam was slightly larger than the size of the pattern, while the transmitted light was focused with a lens on an optical fiber. The experimental setup is shown in Fig. 7.5.

The results at normal incidence are presented in Fig. 7.6, where the estimates of the traditional theory are again exceeded. In contrast to the microwave sample with the dielectric substrate, the maxima are well beyond the cut-off of the waveguide modes in the holes. Due to the two different interfaces, two transmission maxima are predicted by theory for each peak of

[2] Optical measurements were performed in collaboration with A. S. Schwanecke.

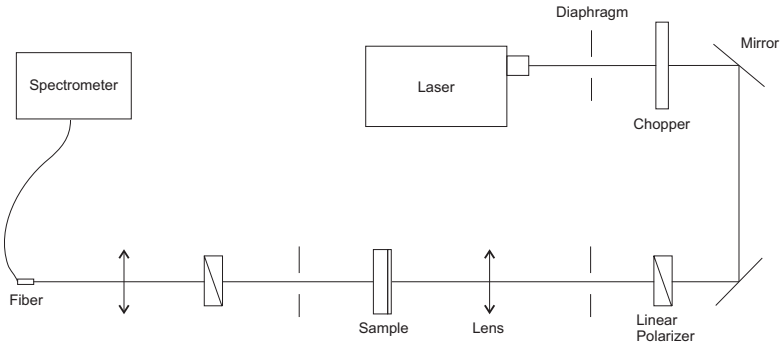

Fig. 7.5: Optical setup for transmission measurements.

the Fourier transform, but it is not clear if the two peaks which are visible in the experimental spectrum, correspond to a single interface and two reciprocal vectors or a single resonant transmission peak split due to the different permittivities on the two sides of the metal film.

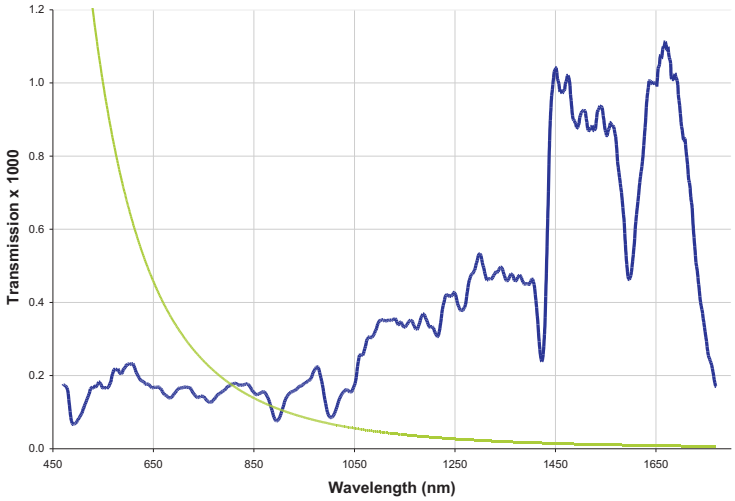

Fig. 7.6: Transmission spectrum of the optical sample at normal incidence (blue) and the corresponding Bowkamp prediction (green).

7.5 Conclusions

In conclusion, enhanced transmission of microwaves through quasi-periodic hole arrays was demonstrated theoretically and experimentally in perfect conductors which can not support surface plasmons. A direct relation between the reciprocal space maxima and the transmission peaks has been established. In particular, an *invisible metal* state characteristic of Breit-Wigner resonances has been observed, where almost total transmission with zero phase change can be achieved by placing a structured film between two dielectric slabs. The wavelength position of the total transmission can be tuned either by varying the permittivity of the dielectric slabs or by appropriately scaling the pattern. The scalability of the approach is demonstrated by scaling the quasicrystal pattern into the telecom spectral region and obtaining results analogous to those

of the microwave hole arrays. Finally, the results presented here are almost independent of the polarization of the incident wave, due to the high orientational order of the quasicrystal.

BIBLIOGRAPHY

[1] H. A. Bethe. Theory of diffraction by small holes. *Physical Review* **66**, 163 (1944).

[2] C. J. Bouwkamp. On the diffraction of electromagnetic waves by small circular disks and holes. *Philips Research Report* **5**, 321 (1950).

[3] C. J. Bouwkamp. Diffraction theory. *Reports on Progress in Physics* **17**, 35 (1954).

[4] W. H. Eggimann and R. E. Collin. Dynamic interaction fields in a two-dimensional lattice. *IEEE Transactions on Microwave Theory and Techniques* **9**, 110 (1961).

[5] W. H. Eggimann and R. E. Collin. Electromagnetic diffraction by a planar array of circular disks. *IEEE Transactions on Microwave Theory and Techniques* **10**, 528 1962.

[6] C. C. Chen. Diffraction of electromagnetic waves by a conducting screen perforated periodically with holes. *IEEE Transactions on Microwave Theory and Techniques* **19**, 475 (1971).

[7] C. C. Chen. Transmission of microwave through perforated flat plates of finite thickness. *IEEE Transactions on Microwave Theory and Techniques* **21**, 1 (1973).

[8] T. W. Ebbesen, H. J. Lezec, H. F. Ghaemi, T. Thio, and P. A. Wolff. Extraordinary optical transmission through sub-wavelength hole arrays. *Nature* **391**, 667 (1998).

[9] H. F. Ghaemi, T. Thio, D. E. Grupp, T. W. Ebbesen, and H. J. Lezec. Surface plasmons enhance optical transmission through subwavelength holes. *Physical Review B*, **58**, 6779 (1998).

[10] L. M. Moreno, F. J. G. Vidal, H. J. Lezec, K. M. Pellerin, T. Thio, J. B. Pendry, and T. W. Ebbesen. Theory of extraordinary optical transmission through subwavelength hole arrays. *Physical Review Letters* **86**, 1114 (2001).

[11] M. Sarrazin, J. P. Vigneron, and J. M. Vigoureux. Role of wood anomalies in optical properties of thin metallic films with a bidimensional array of subwavelength holes. *Physical Review B* **67**, 085415 (2003).

[12] J. B. Pendry, L. Martn-Moreno, and F. J. Garcia-Vidal. Mimicking surface plasmons with structured surfaces. *Science* **305**, 847 (2004).

[13] F. J. Garcia de Abajo, R. Gomez-Medina, and J. J. Saenz. Full transmission through perfect-conductor subwavelength hole arrays. *Physical Review E* **2**, 016608 (2005).

[14] F. J. Garcia de Abajo and J. J. Saenz. Electromagnetic surface modes in structured perfect-conductor surfaces. *Physical Review Letters* **95**, 233901 (2005).

[15] A. S. Schwanecke, N. Papasimakis, V. A. Fedotov, F. Huang, Y. Chen, F. J. Garca de Abajo, and N. I. Zheludev. Invisible quasi-periodic array of subwavelength apertures in metal screen. Nanophotonics Topical Meeting (NANO) at IPRA/NANO OSA Collocated Topical Meetings, Uncasville, CT, USA, 24 - 28 Apr 2006.

[16] F. J. Garcia de Abajo, Y. Chen, V. A. Fedotov, N. Papasimakis, A. S. Schwanecke, and N. I. Zheludev. Extraordinary light transmission through quasicrystal arrays of holes in a metal film. Photonic Metamaterials: From Random to Periodic, Grand Island, The Bahamas, 5 - 8 Jun 2006.

[17] S. Mei, T. Jie, L. Z. Yuan, C. B. Ying, Z. D. Zhong, J. Z. Zi, and Y. H. Fang. The role of periodicity in enhanced transmission through subwavelength hole arrays. *Chinese Physics Letters*, 23(2):486–488, 2006.

[18] T. Matsui, A. Agrawal, A. Nahata, and Z. V. Vardeny. Transmission resonances through aperiodic arrays of subwavelength apertures. *Nature* **446**, 517 (2007).

[19] J. Bravo-Abad, F. J. Garcia-Vidal, and L. Martin-Moreno. Transmission of light through quasiperiodic arrays of subwavelength holes. *Physical Review Leterrs* **99**, 203905 (2006).

[20] F. J. Garcia de Abajo, J. J. Saenz, I. Campillo, and J. S. Dolad. Site and lattice resonances in metallic hole arrays. *Optics Express* **14**, 7 (2006).

[21] L. D. Landau and E. M. Lifshitz, *Quantum Mechanics* (Pergamon, 1958).

8. POLARIZATION SENSITIVE TOROIDAL METAMATERIAL

8.1 Introduction

Toroidal, doughnut-shaped structures are ubiquitous in nature, appearing on scales which range from the sub-atomic [1, 2] to the astronomical [3]. On the molecular level, the torus shape is preferred by numerous biological and chemical macromolecules, such as DNA condensates [4, 5], proteins [6, 7], bacteriophages [8] and oligosaccharides [9], to name just a few (see Fig. 8.1).

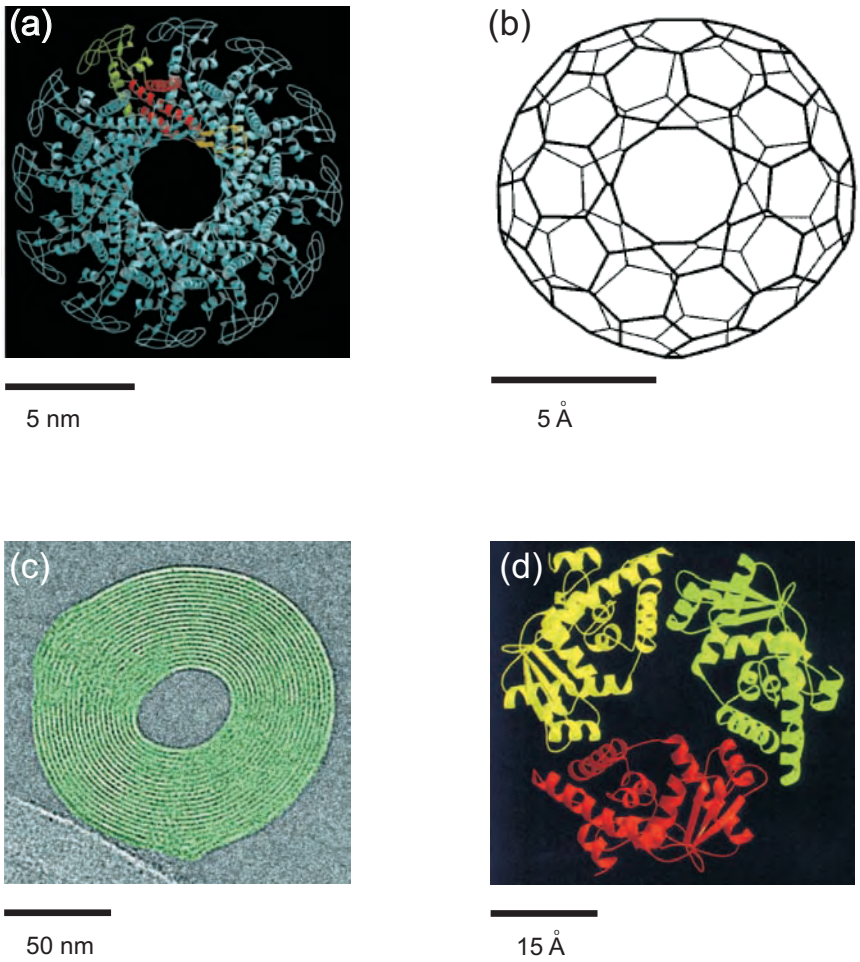

Fig. 8.1: Examples of molecular chiral toroidal structures (a-d): the head-tail connector of bacteriophage $\phi 29$ [8] (a), a torus-shaped fullerene [11] (b), a toroidal DNA condensate [4] (c), and a DNA exonuclease [7].

Toroidal symmetries are also encountered frequently in solid-state systems including fullerenes

[10, 11] and ferroelectrics [12, 13]. The electronic behavior of such systems has been studied extensively and a quantum mechanical formalism has been developed to show that toroidal frames consisting of carbon molecules support both permanent and induced toroidal moments [11]. However, the interactions of toroidal structures with electromagnetic radiation are not well understood. Indeed, within the framework of classical electrodynamics, unusual phenomena associated with violation of Lorentz reciprocity [14] and non-radiating configurations [15] have been predicted for toroidal structures. Nevertheless, experimental investigations of the electromagnetic response of such structures are rare [16]. Here, the first experimental investigation of a toroidal metamaterial [17] focusing in polarization sensitive effects is reported.

8.2 Resonant Circular Dichroism

In contrast to "helical" gyrotropic media, where handedness is usually associated with the direction of a "twist vector" following the cork-screw law along a helicity axis, the situation is more complicated when the structure possesses toroidal symmetry (see Fig. 8.2). Here, the twist vector rotates along the torus. However, although no helicity axis exists, the structure has two well-defined enantiomeric forms, corresponding to different directions of the winding.

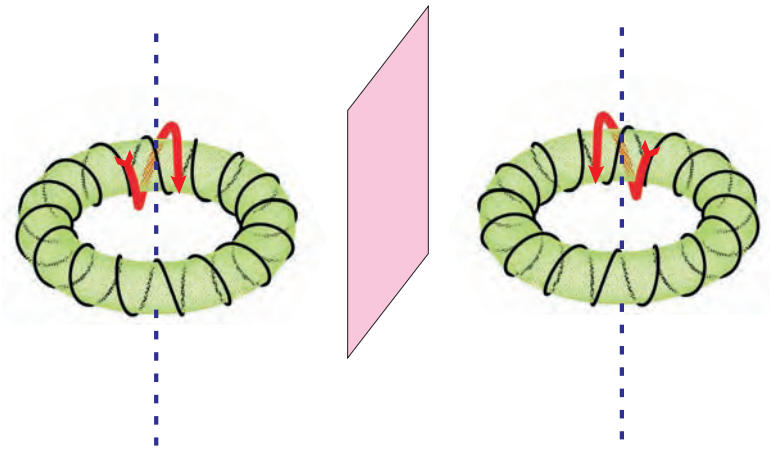

Fig. 8.2: Right and left-handed form of a chiral toroidal coil are connected by a mirror-reflection.

In order to investigate the gyrotropic properties of toroidal media a metamaterial consisting of toroidal wire windings was fabricated. The metamaterial's $15x15\ mm$ unit cell is presented on Figs. 8.3a & 8.3b, while the full $13x13$ array is shown in Fig. 8.3c. More precisely, the toroidal wire winding of the metamaterial unit cell was etched on both faces of a dielectric slab substrate with permittivity $\epsilon = 4.5 - 0.081i$. The strips are connected by metal wires linking strips on opposite sides of the slab in order to create a closed toroidal wiring consisting of four full loops. The metamaterial was formed by first manufacturing one-dimensional arrays of such wire coils supported on a single slab of dielectric and then assembling them in a two-dimensional regular array with pitch equal to the distance between individual wire coils in the slabs.The slab in the grid were oriented in such a way that the toroidal axes lie in the plane of the metamaterial array.

The polarization sensitive behavior of the metamaterial was investigated by measuring all four complex parameters of the structure's transmission matrix in a linear polarization basis and then

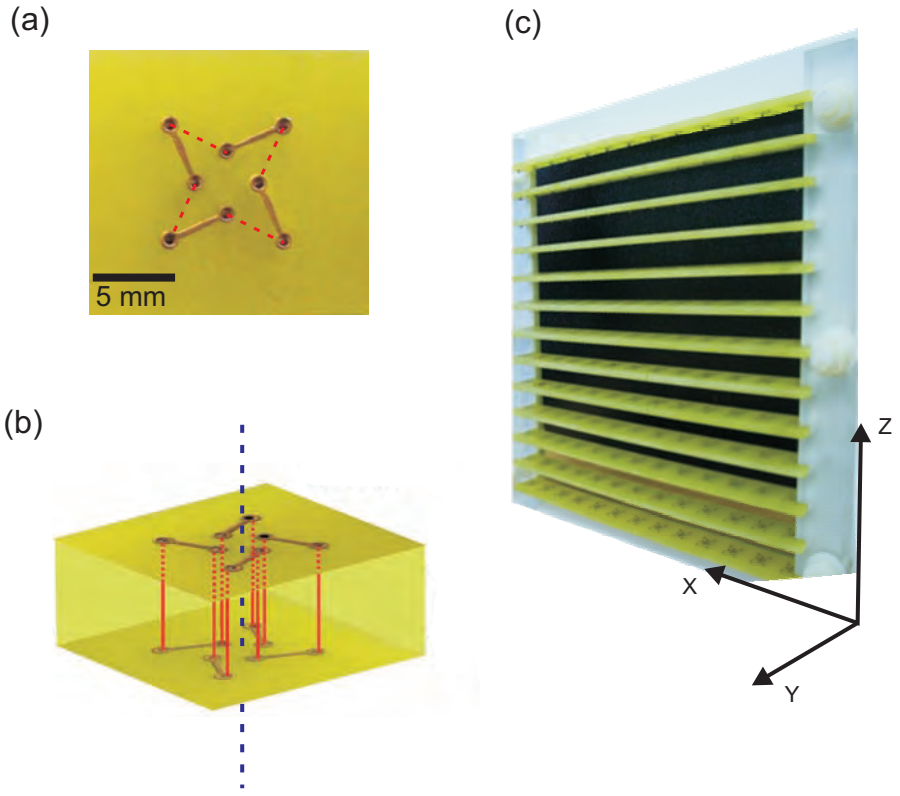

Fig. 8.3: (a-c) Artificial chiral toroidal metamaterial. Plates (a) and (b) show top and side views of the unit cell of the toroidal structure of copper wires supported by a dielectric layer. In the experimental measurements the toroids are arranged into a 13 × 13 metamaterial array so that the normally incident electromagnetic wave propagates perpendicular to the axes of the toroids.

transferring to a circular polarization basis. This enabled the calculation of the corresponding circular differential (left-right) transmission $\Delta t = t_+ - t_-$ and the differential phase delay $\Delta\varphi = \varphi_+ - \varphi_-$, respectively, which are standard measures used to characterize polarization response of chiral media. The first is a measure of the circular dichroism of the medium, while the latter is equal to the polarization plane rotation of a linearly polarized wave resulting from interactions with the structure. Experimental results are shown in Fig. 8.4. Three resonant bands of strong circular dichroism can be distinguished at around $\nu_2 = 4.5GHz$, $\nu_4 = 7.5GHz$ and $\nu_6 = 10GHz$, while corresponding resonant features are also seen in the circular differential phase dispersion. At the $\nu_4 = 7.5GHz$ both polarization states are rejected, one more strongly than the other, while at the low and high frequency resonances, the polarization selective behaviour is particularly strong with transmission of the non-rejected polarization remaining above 50%. At the same time, the phase derivative for orthogonal polarizations has opposite signs, one corresponding to a forward propagating wave, while the other to a backward wave, which is considered to be a manifestation of negative refraction in chiral media [20]. Finite element numerical calculations were also performed for the same structure and good agreement with the experimental results was observed (see black circles and green curve in Fig. 8.4)

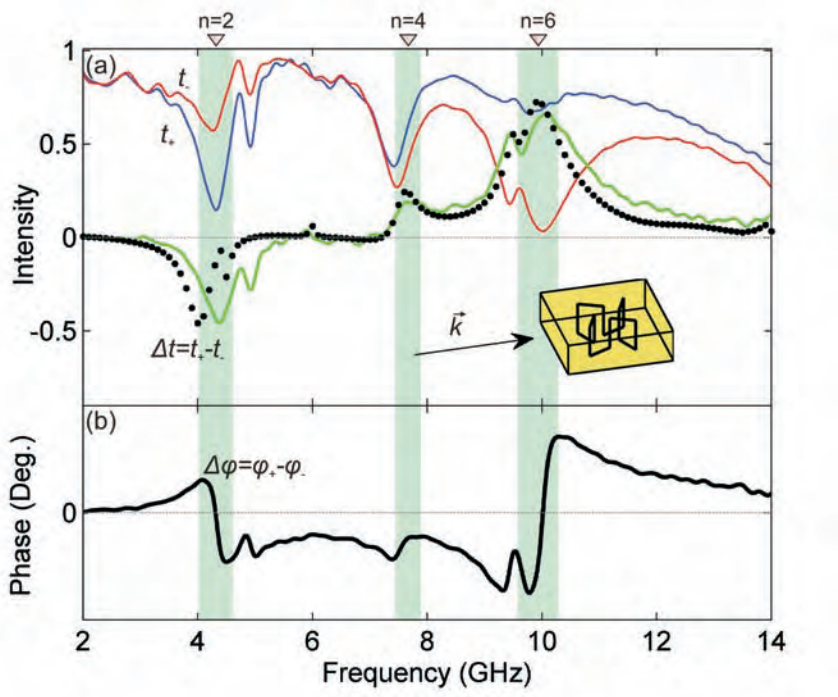

Fig. 8.4: (a) Transmission t for right (blue) and left (red) circularly polarized wave. The circular dichroism Δt is represented by the solid black curve (experimental) and the black solid circles (numerical). The positions of the main dichroism resonances at ν_2, ν_4 and ν_6 are marked by the green strips. Inset: Sketch of the toroidal metamaterial unit cell and direction of wave propagation. Panel (b) shows the left-right differential phase delay, $\Delta\varphi = \varphi_+ - \varphi_-$.

8.3 Origin of Gyrotropy in Toroidal Metamaterials

The nature of these resonances can be elucidated by numerical calculations of field and current distributions induced by the electromagnetic wave in the toroidal wire coils (see Fig. 8.5). They clearly illustrate the origin of circular dichroism of the metamaterial. Figures 8.5a & 8.5b show the energy density maps and power flow lines (tangent to the Poynting vector at each point) near the toroidal coil under resonance conditions (at the 4 GHz dichroism band). While right circular polarization interacts strongly with the left-handed coil and is strongly absorbed as indicated by the "winding" of the power flow lines in the vicinity of the wires (see Fig. 8.5a), the orthogonal polarization state propagates almost unaffected (Fig. 8.5b). Figures 8.5c & 8.5d show the amplitudes of current oscillations induced by the incident wave at two most prominent resonances, ($\nu_2 \simeq 4\ GHz$ and $\nu_6 \simeq 10 GHz$).

From here one can clearly see that the observed resonances are linked to the excitation of multi-nodal standing current waves, the form of which is disturbed by the sharp corners of the wire winding that introduce higher harmonics, as well as by the finite width of the wires and by interactions between opposite-facing loops. Under a coarse approximation, resonances occur when the total wire length in the metamaterial unit cell is equal to an integer multiple of the excitation wavelength with even number of nodes. Here the presence of the dielectric also has to be taken into account in the estimation of the effective wavelength. Correspondingly the subscript numbering resonances $\nu_2 = 4.5\ GHz$, $\nu_4 = 7.5\ GHz$ and $\nu_6 = 10\ GHz$ is simply the number

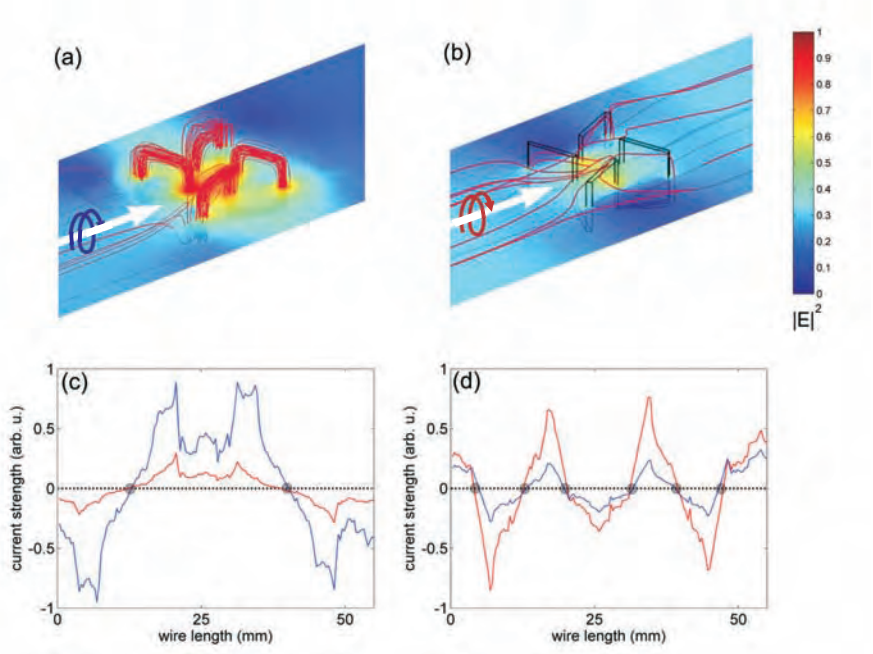

Fig. 8.5: The electric energy density (color maps) and power flow (red lines) near the chiral toroidal coil depends on whether the incident wave is right-circularly polarized (a) or left-circularly polarized. Plates (c) and (d) present the multi-nodal structure of the induced current configuration on the wire winding: two nodes are seen at $\nu_2 = 4.5\ GHz$ (c) and six modes are seen at $\nu_6 = 10\ GHz$ for both right (blue) and left (red) circularly polarized light. The amplitude of the current oscillations depends strongly on the polarization of the incident wave.

of nodes in the standing current distribution. The array of tori shows strong resonant circular dichroism and circular birefringence at frequency regions where electromagnetic excitation induces a multi-nodal standing current wave on the wire coil with the opposite sections of the torus working in unison (ν_2 & ν_6). This means that at any given time the currents in the opposite sections of the coil flow in *opposite* directions. This can only be possible in the high-frequency regime where the toroidal coil wire is much longer that the wavelength. On the contrary in the low-frequency limit the induced currents will be in phase all along the wire and thus the opposite sections of the torus would create mutually cancelling contributions to its gyrotropic response.

8.4 Multipole Expansion

The way through which gyrotropy arises in such a structure becomes even clearer within the framework of multipole theory. In general, circular dichroism arises from the coupling of parallel electric and magnetic dipole moments, but can also include a contribution from the electric quadrupole moment [22, 24, 23]. In Fig. 8.6, strength of the first few multipole moments is

presented in terms of radiated power under excitation with a linearly polarized plane wave [25]:

$$\begin{aligned} el.\ dipole\ radiation: &\quad P_p = \tfrac{\omega^4 \mu_0}{12\pi c} |\vec{p}|^2 \\ m.\ dipole\ radiation: &\quad P_m = \tfrac{\omega^4 \mu_0}{12\pi c^3} |\vec{m}|^2 \\ el.\ quadrupole\ radiation: &\quad P_Q = \tfrac{\omega^6 \mu_0}{160\pi c^3} \sum |Q_{ij}|^2, \end{aligned}$$

As expected from the relatively large size of the structure compared to the wavelength, the electric dipole moment dominates the response of the system at all frequencies, while all multipole moments resonate together at the $\nu_2 = 4.5\ GHz$ and $\nu_6 = 10\ GHz$ circular dichroism bands. More concisely, at the low frequency resonance, the magnetic dipole is much stronger than the electric quadrupole, indicating that the main contribution to chirality comes from the electric dipole-magnetic dipole coupling. A similar situation arises at the high frequency dichroism band ($\nu_6 = 10\ GHz$). However, near the weaker $\nu_4 = 7.5\ GHz$ resonance, the electric quadrupole presents a pronounced resonance, while the magnetic dipole moment is weaker. The resonant character of the weak dichroism at this resonance indicates electric dipole-electric quadrupole in addition to the electric dipole-magnetic dipole coupling. This behavior arises directly from the symmetry of the structure and the supported currents as illustrated in the inset of Fig. 8.6 for an idealized toroid which is much smaller than the wavelength. In the ideal case, the mode with $n = 2$ nodes leads to strong electric and magnetic dipole moments, which have the same direction, while $n = 4$ corresponds to a dominant quadrupole excitation of the structure, where electric and magnetic dipole moments vanish. In a small ideal toroidal current this mode is uncoupled to free-space and does not interact with external radiation. In practice however, it is excited due to the finite size of the structure, which also leads to a strong dipole component. On the other hand, the mode with $n = 6$ results in both strong dipole and quadrupole moments and thus in a more complex response.

8.5 Toroidal Response and Gyrotropy

The toroidal moments were first introduced by Zeldovich in 1958 [1] and are intensively discussed in the literature with only a few experiments claiming to having detected them [16]. It has been suggested that the complete multipole expansion requires the inclusion of toroidal moments along with the electric and magnetic ones [26]. While usually these moments can be neglected, this is not true for structures comparable to the wavelength or structures of toroidal symmetry [26], as the one considered here. Moreover, the toroidal moment is known to result in magneto-electric coupling [27], since it enters the multipole expansion in exactly the same way as the electric moments [26]. Therefore one might expect that coupling between toroidal and magnetic moments would lead to optical activity and the question of a toroidal contribution to the observed chirality arises. Indeed, the studied structure is topologically suitable for supporting magnetic toroidal moments arising from a ring-like configuration of magnetic dipole moments as shown in Fig. 8.7a, which in turn can be created by a poloidal current. Such a current distribution is supported by a chiral toroidal solenoid in a quasistatic regime: it corresponds to the fundamental current mode with $n = 0$, for which all electric multipole moments vanish, while strong magnetic

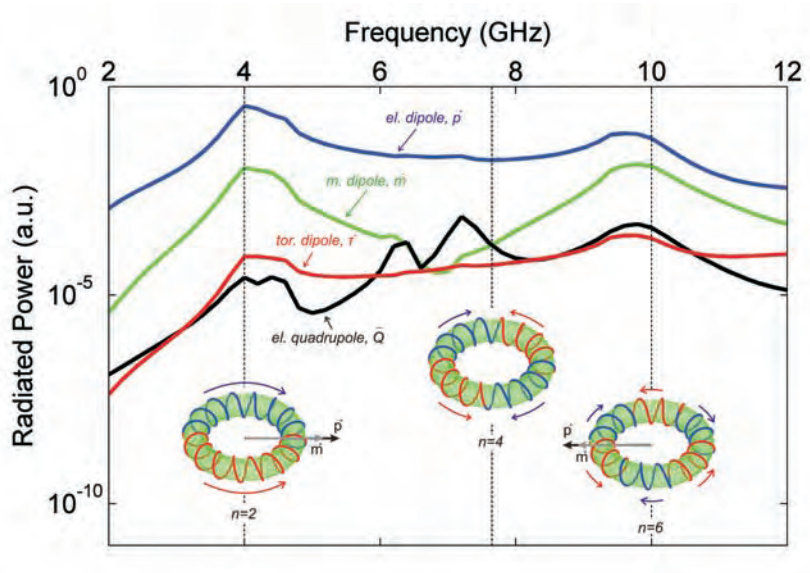

Fig. 8.6: Gyrotropy and multipole response of the structure. Radiated power from the different multipole moments of the (numerically simulated) current configuration on the wire windings, normalized to the incident power. Insets: Idealized resonant currents modes on the toroidal solenoid and leading terms of the multipole expansion for current configurations with two, four and six nodes (from left to right). For $n = 2$ the leading terms are the electric, p and magnetic, m, dipole moments, while for $n = 4$, the latter moments vanish and the electric quadrupole moment, Q, dominates the response of the structure. In the case $n = 6$, both dipole and quadrupole moments are present. Dashed vertical lines show positions of gyrotropy resonances.

dipole m and magnetic toroidal τ moments are supported (Fig. 8.7b). Here the sign of the magnetic dipole depends on the chirality of the toroid and results from the component of the current directed perpendicular to the plane of the winding's loops.

In order to quantify the toroidal response of the metamaterial, we calculate its toroidal moment by the formula, $\vec{\tau} = \frac{1}{10}\int[(\vec{r}\cdot\vec{j})\vec{r} - \vec{r}^2\vec{j}]d^3r$ and present in Fig. 8.6 the corresponding radiated power $P_T = \frac{\omega^6\mu_0}{12\pi c^5}|\vec{T}|^2$ [25]. At most frequencies the toroidal moment is comparable with the electric quadrupole moment, which suggests that the toroidal contribution to the metamaterial response is in general non-negligible. However, as it can be seen from the radiated powers, its contribution in the gyrotropy is at best secondary, since the electric and magnetic dipole/electric quadrupole moments are much stronger at the dichroism resonances. Nevertheless, a much more pronounced toroidal response can be achieved by approaching a quasistatic regime, where a constant current flows along the toroidal wire winding. Due to the symmetry of the structure, such a current configuration has a much weaker electric dipole moment which could lead to a clear manifestation of polarization effects depending on the (magnetic) toroidal moment.

8.6 Conclusions

Molecules and biological structures shaped as tori are widely spread in nature, however specifics of their interactions with electromagnetic radiation are still not comprehensively understood. The first experimental investigation of polarization-sensitive electromagnetic interactions in artificial

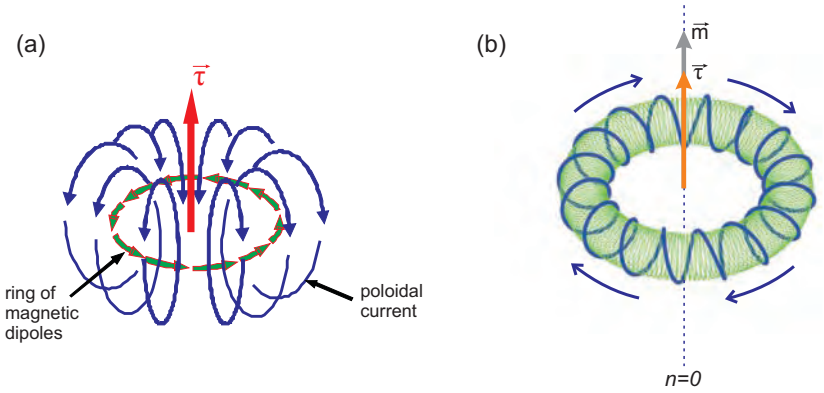

Fig. 8.7: Magnetic toroidal moment. A static poloidal current on a torus creates a ring-like configuration of magnetic dipoles, which in turn leads to a magnetic toroidal dipole moment τ (a). A constant current flowing along the chiral toroidal coil results in a (magnetic) toroidal τ and magnetic dipole m moments. The latter depends on the chirality of the coil (b).

toroidal media is presented. The reported experiments revealed strong resonant optical activity in a chiral toroidal metamaterial, while comparison with detailed numerical modelling of the induced currents provided insights into the non-trivial nature of gyrotropy that is linked to the excitation of multi-nodal standing waves on the wire coil. A multipole expansion of the supported current configuration revealed a non-vanishing induced magnetic toroidal moment.

BIBLIOGRAPHY

[1] Y. B. Zel'dovich. Electromagnetic interaction in the loss of parity. Soviet Physics - Journal of Experimental and Theoretical Physics **6**, 1184 (1958).

[2] V. M. Dubovik, A. A. Cheshkov. Multipole expansion in classical and quantum field theory and radiation. Soviet Journal of Nuclear Physics **5**, 318 (1975).

[3] J. S. Mainstone. Plasma Resonances of the Magnetosphere. *Nature* **215**, 1048 (1967).

[4] N. V. Hud and K. H. Downing. Cryoelectron microscopy of λ phage DNA condensates in vitreous ice. *Proceedings of the National Academy of Sciences* **92**, 3581 (2001).

[5] N. V. Hud and I. D. Vilfan. Toroidal DNA condensates. *Annual Review of Biophysics and Biomolecular Structure* **34**, 295 (2005).

[6] M. M. Hingorani and M. O'Donnell. A tale of toroids in DNA metabolism. *Nature Reviews Molecular Cell Biology* **1**, 22 (2000).

[7] R. Kovall and B. W. Matthews. Toroidal structure of λ-exonuclease, *Science* **277**, 1824 (1997).

[8] Simpson et al. Structure of the bacteriophage ϕ29 DNA packaging motor. *Nature* **408**, 745 (2000).

[9] W. Saenger, J. Jacob, K. Gessler, T. Steiner, D. Hoffmann, H. Sanbe, K. Koizumi, S. M. Smith, and T. Takaha. Cyclodextrin Drug Carrier Systems. *Chemical Reviews* **98**, 1787 (1998).

[10] J. Lium H. Dai, J. H. Hafner, D. T. Colbert, R. E. Smalley, S. J. Tans, and C. Dekker. Individual single-wall carbon nanotubes as quantum wires. *Nature* **385**, 780 (1997).

[11] A. Ceulemans, L. F. Chibotaru, and P. W. Fowler. Molecular anapole moments. *Physical Review Letters* **80**, 1861 (1998).

[12] A. A. Gorbatsevich and Y. V. Kopaev. Toroidal order in crystals. *Ferroelectrics* **161**, 321 (1994).

[13] I. I. Naumov, L. Bellaiche and H. X. Fu. Unusual phase transitions in ferroelectric nanodisks and nanorods. *Nature* **432**, 737 (2004).

[14] G. N. Afanasiev. Simplest sources of electromagnetic fields as a tool for testing the reciprocity-like theorems. *Journal of Physics D* **34**, 539 (2001).

[15] G. N. Afanasiev and V. M. Dubovik. Some remarkable chargecurrent configurations. *Physics of Particles and Nuclei* **29**, 366 (1998).

[16] K. Sawada and N. Nagaosa. Optical Magnetoelectric Effect in Multiferroic Materials: Evidence for a Lorentz Force Acting on a Ray of Light. *Physical Review Letters* **95**, 237402 (2005).

[17] K. Marinov, A. D. Boardman, V. A. Fedotov, and N. I. Zheludev, Toroidal metamaterial *New Journal of Physics* **9**, 324 (2007).

[18] V. M. Agranovich, Y. N. Gartstein, and A. A. Zakhidov. Negative refraction in gyrotropic media. *Physical Review B* **73**, 045114 (2006).

[19] E. Plum, J. Zhou, J. Dong, V. A. Fedotov, T. Koschny, C. M. Soukoulis, and N. I. Zheludev. Metamaterial with negative index due to chirality. *Physical Review B* **79**, 035407 (2009).

[20] J. B. Pendry. A chiral route to negative refraction. *Science* **306**, 1353 (2004)

[21] S. Tretyakov, A. Sihvola, and L. Jylha, Photon. and Nanostr. **3**, 107 (2005).

[22] A. D. Buckingham and M. B. Dunn. Optical activity of oriented molecules. *Journal of the Chemical Society A*, **1971**, 1988 (1971).

[23] Y. P. Svirko and N. I. Zheludev, *Polarization of Light in Nonlinear Optics* (Wiley, 2000).

[24] I. P. Theron and J. H. Cloete. The electric quadrupole contribution to the circular birefringenceof nonmagnetic anisotropic chiral media: a circular waveguide experiment. *IEEE Transactions on Microwave Theory and Techniques* **44**, 1451 (1996).

[25] C. Vrejoiu. Electromagnetic multipoles in Cartesian coordinates. *Journal of Physics A* **35**, 9911 (2002).

[26] V. M. Dubovik and V. V. Tugushev. Toroid moments in electrodynamics and solid-state physics. *Physics Reports* **187**, 145 (1990).

[27] M. Fiebig. Revival of the magnetoelectric effect. *Journal of Physics D* **38**, R123 (2005).

9. CONCLUSION & FUTURE WORK

9.1 Summary

Two antipode classes of metamaterials were introduced. Coherent metamaterials exhibit collective, coherent response available only in sufficiently large arrays, while in incoherent metamaterials the respose reduces to a sum of the contributions from the individual elements. The behaviour of both metamaterial types upon introducing random displacements was investigated and it was shown that coherent metamaterials are extremely sensitive to disorder. On the other hand, incoherent metamaterials appeared to be almost immune to positional disorder. It was demonstrated numerically, that coherent metamaterials allow for efficient amplification in the optical and mid-infrared part of the spectrum.

Mimicking the quantum phenomenon of electromagnetically induced transparency (EIT), it was shown experimentally that the resonant response of planar metamaterials can be engineered in order to provide sharp resonances and long pulse delays. Based on destructive interference between the metamaterial unit cell constituents, this approach allows for pulse delays exceeding 1/3 of the transmitted pulse width in structures as thin as $\lambda/35$ along the propagation direction. Bandwidth enhancement of the slow light effect was demonstrated by cascading the metamaterial with little effect on the achievable pulse delay. Normal incidence and polarization restrictions were aleviated by introducing an isotropic, incoherent metamaterial with EIT-like response.

A different type of interference was investigated in chiral metamaterials of toroidal symmetry consisting of wire windings on the surface of a torus. The polarization-sensitive behaviour of such a metamaterial was studied experimentally and numerically in the microwave part of the spectrum revealing the presence of strong resonant circular dichroism. Looking into the current configuration and its multipole expansion, it was possile to relate the circular dichroism resonances to the eigenmodes of the toroidal winding and quantify the contributions arising from coupling between different multipole moments. A non-negligile toroidal response was also observed, where the associated dipole moment was found comparable to the electric quadrupole in scattering efficiency.

Finally, the study of collective effects was extended to lattices of non-resonant inclusions leading to an experimental demonstration of surface-plasmon free extraordinary transmission in a quasiperiodic hole array. Scaled versions of such a structure were characterized both in the microwave and optical domain and a close relation between the long-range order of quasicrystals and the observed lattices resonances was established.

9.2 Future Work

The new types of metamaterials studied here pave the way towards enhanced control of the metamaterial response by appropriate engineering of the unit cell resonator. Future work can focus on transferring the reported effects to the optics domain: an immediate application of coherent metamaterials would be the realization of the lasing spaser. Such a planar light-emitting device can be a valuable asset especially in the optical domain due its compactness and efficiency. Moreover, moving into the so-called THz gap is also of great interest, since the availability of efficient light sources is limited at these frequencies. In addition, the strong surface waves supported by coherent metamaterials can become especially important when the wavelength approaches the position where the so-called Wood's anomalies occur. At these wavelengths, new resonances should appear associated with these surface waves in ways very similar to extraordinary transmission. Of special interest is the case where these resonances will coincide with the meta-molecule resonance. This combination can provide an extremely powerful feedback mechanism, which in the presence of gain media will allow to increase further the efficiency of amplification. In addition, since the energy would be stored in the form of oscillating magnetic dipoles, such a metamaterial would have an extremely strong magnetic response, uncoupled to the incident magnetic field, which can prove useful in the field of artificial magnetism. Incoherent metamaterials on the other hand are expected not only to facilitate self-assembly fabrication methods due to the independence from disorder, but also to enable even more compact metamaterial-based devices. In incoherent metamaterials, functionalities can manifest in a small number of unit cells, essentially due to the vanishing scattering losses and weak interactions between the meta-molecules. This could possibly allow the realization of delay lines and sensors consisting of a few, or even a single, sub-wavelength meta-molecule.

Finally, toroidal metamaterials provide a unique opportunity to observe the elusive effects associated with the so-called toroidal family of multipole moments. In particular, it is expected that by moving to a low frequency regime, the toroidal response of toroidal metamaterials can be enhanced, while the electric multipole response will diminish. Intriguingly, the magnetic multipole of the system can be controlled by considering either non-connected or connected loops along the meridians of the torus. The first structure allows to isolate the toroidal response by suppressing electric and magnetic multipoles, while the latter will result in a strong magnetic dipole moment co-linear with the toroidal magnetic dipole moment. Noting that the toroidal magnetic dipole moment is very similar to the electric dipole moment, it can be argued that coupling of the former moment with magnetic dipole can lead to a new type of gyrotropy of toroidal origin, similar to the gyrotropy arising due to electric dipole-magnetic dipole coupling. Such effects are of great interest not only in terms of new physics but also in respect with the vast number of macro-molecules that possess toroidal symmetry.

APPENDIX

A. PUBLICATIONS

Publications

- N. Papasimakis, V. A. Fedotov, Y. H. Fu, D. P. Tsai & N. I. Zheludev. Coherent and incoherent metamaterials and the order-disorder transitions. *Physical Review B*, Rapid Communication. In print.

- N. Papasimakis & N. I. Zheludev. Metamaterial induced transparency: sharp resonances and slow light. *Optics and Photonics News*. In print.

- N. Papasimakis, Y. H. Fu, V. A. Fedotov, S. L. Prosvirnin, D. P. Tsai, & N. I. Zheludev. Metamaterial with polarization and direction insensitive resonant transmission response mimicking electromagnetically induced transparency. *Applied Physics Letters* **94**, 211902 (2009).

- S. L. Prosvirnin, N. Papasimakis, V. Fedotov, S. Zouhdi & N. Zheludev. Trapped-mode resonances in planar metamaterials with high structural symmetry. In *Metamaterials and Plasmonics: Fundamentals, Modelling, Applications*, S. Zouhdi et al.(eds.), pp 201-208 (Springer 2009).

- N. Papasimakis, V. A. Fedotov, S. L. Prosvirnin & N. I. Zheludev. Metamaterial analog of electromagnetically induced transparency. *Physical Review Letters* **101**, 253903 (2008).

- N. I. Zheludev, S. L. Prosvirnin, N. Papasimakis & V. A. Fedotov. Lasing spaser. *Nature Photonics* **2**,351-354 (2008).

- V. A. Fedotov, M. Rose, N. Papasimakis, S. L. Prosvirnin & N.I. Zheludev. Sharp trapped-mode resonances in planar metamaterials with broken structural symmetry. *Physical Review Letters* **99**, 147401 (2007).

- N. Papasimakis, V. A. Fedotov, F. J. Garcia de Abajo, A. S. Schwanecke & N. I. Zheludev. Enhanced microwave transmission through quasicrystal hole arrays. *Applied Physics Letters* **91**, 081503 (2007).

Submitted

- V. A. Fedotov, N. Papasimakis, E. Plum, A. Bitzer, M. Walther, P. Kuo, D. P. Tsai & N. I. Zheludev. Spectral collapse in ensembles of meta-molecules. Submitted to *Science*.

- N. Papasimakis, V. A. Fedotov, K. Marinov, A. D. Boardman & N. I. Zheludev. Strong gyrotopy in a chiral toroidal medium. Submitted to *Physical Review Letters*.

Conference presentations

- (keynote) N. I. Zheludev, V. A. Fedotov, N. Papasimakis, E. Plum & J. Shi: Metamaterials - from modeling and fabrication to application. 2009 MRS Fall Meeting, Boston, Massachusetts, USA, 30 Nov - 04 Dec 2009.
- N. Papasimakis, V. A. Fedotov, Y. H. Fu, D. P. Tsai & N. I. Zheludev: Coherent metamagnetics: collective resonances and disorder-induced transitions. ICO-Photonics, Delphi, Greece, 7 - 9 Oct 2009.
- (invited) N. I. Zheludev, V. A. Fedotov, E. Plum & N. Papasimakis: Coherent metamaterials. Metamaterials 2009 Congress, London, UK, 30 Aug - 04 Sep 2009.
- V. A. Fedotov, N. Papasimakis, A. Bitzer, M. Walther & N. I. Zheludev: Metamaterial analogue of the Mssbauer effect. CLEO/Europe-EQEC, Munich, Germany, 14 - 19 Jun 2009.
- (invited) N. Papasimakis, V. A. Fedotov & N. I. Zheludev: Coherent metamaterials: from optical ferromagnetism to the lasing spaser. CLEO/IQEC 09, Baltimore, Maryland, USA, 31 May - 05 Jun 2009.
- (invited) N. I. Zheludev, N. Papasimakis & V. A. Fedotov: Coherent and incoherent metamaterials. NanoMeta 2009, Seefeld, Austria, 5-8 Jan 2009.
- N. Papasimakis, K. Marinov, V. A. Fedotov, A. D. Boardman & N. I. Zheludev: Testing the controversies of toroidal electrodynamics using metamaterials. Plasmonics and Metamaterials (META), Rochester, NY, USA, 20 - 23 Oct 2008.
- N. Papasimakis, V. A. Fedotov, K. Marinov, A. D. Boardman & N. I. Zheludev: Optical activity in toroidal metamaterials. IoP Quantum Electronics and Photonics Conference (QEP-18), Edinburgh, UK, 26 - 29 Aug 2008.
- (poster) N. I. Zheludev, S. L. Prosvirnin, N. Papasimakis & V. A. Fedotov: Coherent metamaterials and the lasing spaser. IoP Quantum Electronics and Photonics Conference (QEP-18), Edinburgh, UK, 26 - 29 Aug 2008.
- (invited) N. I. Zheludev, S. L. Prosvirnin, N. Papasimakis & V. A. Fedotov: Lasing spaser. SPIE Plasmonics: Metallic Nanostructures and Their Optical Properties VI, San Diego, CA, USA, 10 - 13 Aug 2008.
- N. Papasimakis, V. A. Fedotov, S. L. Prosvirnin & N. I. Zheludev: Slow light in "zero thickness" metamaterials. Slow and Fast Light, Boston, MA, USA, 13 - 16 Jul 2008.
- (invited) N. I. Zheludev, S. L. Prosvirnin, N. Papasimakis & V. A. Fedotov: Coherent meta-materials and the lasing spaser. IEEE COMCAS 2008, Tel Aviv, Israel, 13 - 14 May 2008.
- (invited) N. I. Zheludev, V. A. Fedotov, N. Papasimakis, E. Plum & S. L. Prosvirnin: Close-mode resonances in meta-materials and lasing spaser. Photonics Europe (SPIE Europe), Strasbourg, France, 7 - 11 Apr 2008.

- (invited) N. I. Zheludev, N. Papasimakis, V. A. Fedotov & S. L. Prosvirnin: Coherent Meta-materials and the Lasing Spaser. 6th International Workshop on Nanophotonics, Taipei, Taiwan, 11 Mar 2008.
- (invited) N. Papasimakis, V. A. Fedotov, N. I. Zheludev & S. L. Prosvirnin: Long Pulse Delays; A Planar Metamaterial Analog of EIT. 6th International Workshop on Nanophotonics, Taipei, Taiwan, 11 Mar 2008.
- (invited) F. M. Huang, A. Schwanecke, N. Papasimakis, Y. Chen, F. J. Garcia de Abajo & N. I. Zheludev: Far-field subwavelength focusing and extraordinary transmission of light by a quasi-periodic array of nanoholes. Metamaterials 2007: First International Congress on Advanced Electromagnetic Materials in Microwaves and Optics, Rome, Italy, 22 - 26 Oct 2007.
- (invited) N. I. Zheludev, V. Fedotov, A. Schwanecke, E. Plum, N. Papasimakis & K. Marinov: Plasmon resonances in photonic chiral metamaterials. Frontiers in Optics 2007, San Jose, CA, USA, 16 - 20 Sep 2007.
- (invited) N. I. Zheludev, V. A. Fedotov, M. Rose, N. Papasimakis & S. L. Prosvirnin: Chirality in photonic meta-materials. Photonic Metamaterials at SPIE Optics and Photonics Congress, San Diego, USA, 26 - 30 Aug 2007.
- N. Papasimakis, V. A. Fedotov, S. L. Prosvirnin & N. I. Zheludev: Long pulse delays in thin metamaterial slabs. CLEO/Europe-IQEC2007, Munich, Germany, 17 - 22 Jun 2007.
- V. A. Fedotov, M. Rose, N. Papasimakis, S. L. Prosvirnin & N. I. Zheludev: Achieving sharp resonances in metamaterials through symmetry breaking. CLEO/Europe-IQEC2007, Munich, Germany, 17 - 22 Jun 2007.
- N. Papasimakis, V. A. Fedotov, S. L. Prosvirnin & N. I. Zheludev: Metamaterial analog of electromagnetically induced transparency. Photonic Metamaterials: From Random to Periodic, Jackson Hole, Wyoming, USA, 04 - 07 Jun 2007.
- N. Papasimakis, V. A. Fedotov, S. L. Prosvirnin & N. I. Zheludev: "Slow" light in media of "zero" dimension. QELS (CLEO/QELS 2007), Baltimore, MD, USA, 06 - 11 May 2007.
- V. A. Fedotov, M. Rose, N. Papasimakis, S. L. Prosvirnin & N. I. Zheludev: Achieving sharp resonances in metamaterials via engaging "closed-modes". QELS (CLEO/QELS 2007), Baltimore, MD, USA, 06 - 11 May 2007.
- V. A. Fedotov, M. Rose, N. Papasimakis, S. L. Prosvirnin & N. I. Zheludev: Achieving sharp spectral resonances in metamaterials via engaging 'closed modes'. NANOMETA 2007, Seefeld, Austria, 09 - 11 Jan 2007.
- N. Papasimakis, V. A. Fedotov, S. L. Prosvirnin & N. I. Zheludev: "Slow" light in planar metamaterials. NANOMETA 2007, Seefeld, Austria, 09 - 11 Jan 2007.
- F. M. Huang, A. S. Schwanecke, N. Papasimakis, Y. Chen, F. J. Garcia de Abajo & N. I. Zheludev: Quasi-periodic arrays of subwavelength holes in a metal screen: Self-imaging in

the near-field and far-field extraordinary transmission. NFO-9, Lausanne, Switzerland, 10 - 15 Sep 2006.

- F. J. Garcia de Abajo, V. A. Fedotov, N. Papasimakis, A. S. Schwanecke, Y. Chen & N. I. Zheludev: Extraordinary transmission through planar quasicrystal. QEP-17 at Photon06, Manchester, UK, 4 - 7 Sep 2006.

- F. J. Garcia de Abajo, Y. Chen, V. A. Fedotov, N. Papasimakis, A. S. Schwanecke & N. I. Zheludev: Extraordinary light transmission through quasicrystal arrays of holes in a metal film. SPIE Optics and Photonics 2006, Complex Photonic Media (NP201), San Diego, CA, USA, 13 - 17 Aug 2006.

- F. J. Garcia de Abajo, Y. Chen, V. A. Fedotov, N. Papasimakis, A. S. Schwanecke & N. I. Zheludev: Extraordinary light transmission through quasicrystal arrays of holes in a metal film. Photonic Metamaterials: From Random to Periodic, Grand Island, The Bahamas, 5 - 8 Jun 2006.

- A. S. Schwanecke, N. Papasimakis, V. A. Fedotov, F. Huang, Y. Chen, F. J. Garca de Abajo & N. I. Zheludev: Invisible quasi-periodic array of subwavelength apertures in metal screen. Nanophotonics Topical Meeting (NANO) at IPRA/NANO OSA Collocated Topical Meetings, Uncasville, CT, USA, 24 - 28 Apr 2006.